Study of the Fluid Mechanics of Aerodynamic Microparticle Sampling

Patrick Fillingham

A dissertation submitted in partial fulfillment of the requirements for the degree of

Doctor of Philosophy

University of Washington

2020

Reading Committee:

Igor V. Novosselov, Chair

James Riley

Alberto Aliseda

Program Authorized to Offer Degree:

Mechanical Engineering

University of Washington

Abstract

Study of the Fluid Dynamics of Aerodynamic Microparticle Sampling

Patrick Fillingham

Chair of Supervisory Committee

Igor Novosselov:

Research Associate Professor of Mechanical Engineering

It is no secret that there is significant room for improvement when it comes to security at airports and other secure locations. One area with considerable room for improvement is in passenger screening for the presence of illicit materials. Traditional swabbing methods used for sampling can be inconvenient and ineffective. Non-contact sampling can offer improvements over traditional sampling methods by increasing speed and effectiveness. Aerodynamic sampling uses a combination of impinging jets to remove particles from the surface of interest and suction to direct the removed particles onto a collection substrate or directly to a detector of choice. This offers improvements over swabbing, as there is less room for contamination of the sampling substrate, removes user bias, and allows for sampling of larger areas in less time. To design an effective non-contact surface sampler, one must characterize several distinct phenomena; the flow field of impinging jets, the necessary flow conditions for the removal of micro-particles resting on

a surface, and the aerodynamic forces experienced by particles under these conditions. This dissertation focuses on (i) characterization of wall shear stress from axisymmetric underexpanded impinging jets, (ii) development of equations for the wall jet velocity profile and wall shear stress of planar underexpanded impinging jets, (ii) development of a method for calculating the adhesion force of spherical microparticles, and (iv) formulations of aerodynamic forces on non-spherical particles in a boundary layer.

TABLE OF CONTENTS

LIST OF FIGURES

LIST OF TABLES

ACKNOWLEDGEMENTS

I want to first thank Igor Novosselov for being an exceptional advisor, mentor, and collaborator. I greatly appreciate the balance of independence and helpful direction you have provided to me over the past five years and I feel very lucky to have been given the opportunity to grow as a researcher under your guidance.

I also want to recognize my lab mates and peers for always lending a helping hand whenever I reached out. Working with everyone in the NRG lab has been a great experience. I especially want to thank Ravi Vadi, Kalyan Kottapalli, and Yifei Guan, whom I have been fortunate to collaborate closely with, for their insight and friendship.

I would like to thank Dr. Alberto Aliseda and Dr. James Riley for their willingness to provide advice and assistance whenever I reached out with a problem.

Finally, I want to thank my family and friends, whose support and willingness to always go grab a beer has been crucial to my grad school experience.

Chapter 1. INTRODUCTION

Aerodynamic particle resuspension is relevant in studies across scientific disciplines. From the spread of infectious disease to the cleaning of microelectronics, understanding how particles resting on a surface will behave when exposed to a flow field is essential. One field where studying aerodynamic particle suspension can have a significant impact, and is the focus of this work, is the detection of illicit material and specifically the detection of trace amounts of explosives. There is a need for improvement in the ability to sample and detect explosive residue at airports and other checkpoint and screening applications.[1]

Trace amounts of energetic particles will be abundant on the hands, clothes, and luggage of individuals who have been handling explosives, and thus can be detected via sampling of these surfaces. Current protocol for trace explosive detection is to use a contact tracing method known as the "swab test" in which the surface of interest is swabbed by hand with a material such as nylon or cotton, which is then placed in a benchtop detection device. This method is subject to contamination, inconsistency through human error, high variance depending on the surface of interest, and general poor performance. There is also a need to sample large surfaces at security checkpoints such as large pieces of luggage or entire vehicle surfaces; sampling of these large surfaces is simply infeasible via current swabbing methods. Non-contact aerodynamic sampling potentially offers upgrades over contact sampling in all of these areas as well as speed, ease of use and efficiency[1].

While aerodynamic sampling is promising, it involves complex phenomena and thus requires thorough investigation to optimize the design of an aerodynamic particle sampler. There has been substantial research into microparticle resuspension via impinging jets [2,3] demonstrating the potential for aerodynamic sampling, but these studies are limited to low-pressure jets and

spherical glass or polystyrene particles. Trace explosive residue particles are irregularly shaped, are especially adhesive [4], and require high pressure, under expanded jets for removal[5,6]. Thus it is essential to understand both (i) the flow dynamics of underexpanded impinging jets and the resulting wall jet flow and (ii) the forces on particles resting in the resulting wall jet boundary layers. This thesis focuses on the use of extensive computational studies to parametrically characterize both the flow field of underexpanded impinging jets and the flow field of a microparticle in a boundary layer.

The second chapter of this thesis explores underexpanded axisymmetric impinging jets. Through an extensive computational study, the author was able to develop a set of equations for mapping the wall shear stress along the impingement surface as a function of nozzle parameters: nozzle pressure ratio, nozzle diameter, and standoff height. *These equations can be used to predict wall shear at any location on the impingement surface stress within a mean error of 4%.*

Chapter three utilizes computational fluid dynamics to study the flow field of underexpanded planar impinging jets through the lens of wall jet self-similarity. The computational study provides a data set to confer the wall jet resulting from underexpanded impinging jets follow the same self-similar structure of traditional wall jets. Thus, it allows for the use of similarity parameters such as friction velocity and maximum wall jet velocity and location, to map out the entire wall jet velocity field. The chapter lays out a set of equations for predicting these similarity variables as a function of jet parameters and location on the impingement surface. Using source dependent power-law relationships, the similarity variables can be predicted within a mean deviation from the CFD of only 3%. *These similarity variables can then be used to calculate the entire wall jet velocity profile, including the wall shear stress, at any location downstream of impingement.* This insight is useful for designing aerodynamic sampling or cleaning devices as

one can predict the flow field resulting from these jets with only the nozzle pressure ratio, jet width, and jet standoff height.

In chapter four, the author shows the calculation of the forces acting on a particle during aerodynamic resuspension. This work combines computational and experimental study to determine the wall shear stress required to remove 50% of silica microspheres attached to the surface, then pairs that with a computational study that calculates the aerodynamic forces on a microsphere exposed to specific wall shear stress. A moment balance derived from the applied forces is used to solve for the adhesion force experienced by the particles. This work presents (i) a method for calculating adhesion force during rolling removal and (ii) presents results for how the adhesion of microspheres changes with its diameter. This is critical knowledge for determining the necessary flow conditions for particle removal. By understanding the forces acting on a particle during removal, and how they are affected by particle size, we can better understand the necessary design conditions for aerodynamic particle sampling.

Chapter five details the development of a set of equations for calculating the drag and lift coefficient for prolate spheroids resting in a turbulent boundary layer. Direct numerical simulations were conducted for prolate spheroids attached to a wall in a linear shear flow across several parameter. The parametric study provides a data set for fitting equations for drag and lift based upon the orientation angles, Reynolds numbers, and particle aspect ratios. *These equations allow for the calculation of drag coefficient within a mean deviation from DNS of 0.8% and the calculation of the lift coefficient within a mean error of 4.4%.* As particles of interest are typically non-spherical, it is important to understand the aerodynamic forces acting on prolate particles based on their orientation and aspect ratio.

The combination of these chapters present an extensive work on the fluid dynamics of aerodynamic particle resuspension. By characterizing the flow field of underexpanded impinging jets and a comprehensive study of the forces acting on particles the author has laid the groundwork for non-conact particle sampling devices.

Chapter 2. CHARACTERIZATION OF WALL SHEAR STRESS FROM UNDEREXPANDED AXISYMMETRIC IMPINGING JETS

This analysis is published in the Journal of Fluids Engineering[7] The CFD simulations we performed with the assistance of Mr. Hari Murali[8], and the CFD computation results are presented here for completeness.

In this chapter, wall shear stress is characterized for underexpanded axisymmetric impinging jets for the application of aerodynamic particle resuspension from a surface. Analysis of the flow field resulting from normally impinging axisymmetric jets is conducted using Computational Fluid Dynamics. A normally impinging jet is modeled with a constant area nozzle while varying the height to diameter ratio (H/D) and the inlet pressures. Schlieren photography is used to visualize the density gradient of the flow field for validation of the CFD. A Dimensionless Jet Parameter (*DJP*) is developed to describe flow regimes and characterize shear stress. The *DJP* is defined as being proportional to the jet pressure ratio divided by the H/D ratio squared. Maximum wall shear stress is examined as a function of *DJP* with three distinct regimes: (i) subsonic impingement (*DJP*<1), (ii) transitional (1<*DJP*<2), and (iii) supersonic impingement (*DJP*>2). It is observed that wall shear stress is limited to a finite value due to jet energy dissipation in shock structures, which become a dominant dissipation mechanism in the supersonic impingement regime. Additionally, the formation of shock structures in the wall flow were observed for *DJP*>2, resulting in difficulties with dimensionless analysis. In subsonic impingement and transitional regimes, equations as a function of the *DJP* are obtained for the maximum wall shear stress magnitude, maximum shear stress location, and shear stress decay. Using these relationships, wall shear stress can be predicted at all locations along the impingement surface.

2.1 INTRODUCTION

Impinging jets are used for a wide range of engineering applications, which include the cooling of electronic components, surface cleaning in the microelectronic industry, and annealing processes. These jets also have the potential to allow for the rapid collection of the trace amounts of illicit materials. Although not related to particle sampling, the behavior of impinging jets has been studied extensively for the application of vertical aircraft takeoff. These studies are associated with the underexpanded jets with an exit pressure of at least 1.87 times the ambient pressure. These high-pressure jets impinge on the surface and can produce high wall shear stress in the wall jet region. This shear stress is critical in dislodging particles from the surface.

The basic structure of the impinging jet is shown in Figure 1.1. It is comprised of three characteristic regions that include the free jet region (under the nozzle), the stagnation zone (the region of contact with the plate), and the wall jet region along the plate. As the jet is underexpanded, it expands further outside the nozzle through a number of expansion and compression waves. This region of the flow is contained within the potential core in its free jet region and along with it, is a set of acoustic feedback loops formed on impingement against the plate. *Henderson et al.*, *Krothapalli et al.* and *Tam & Ahuja* [9-11] are amongst the researchers who have examined the acoustics of impinging jets.

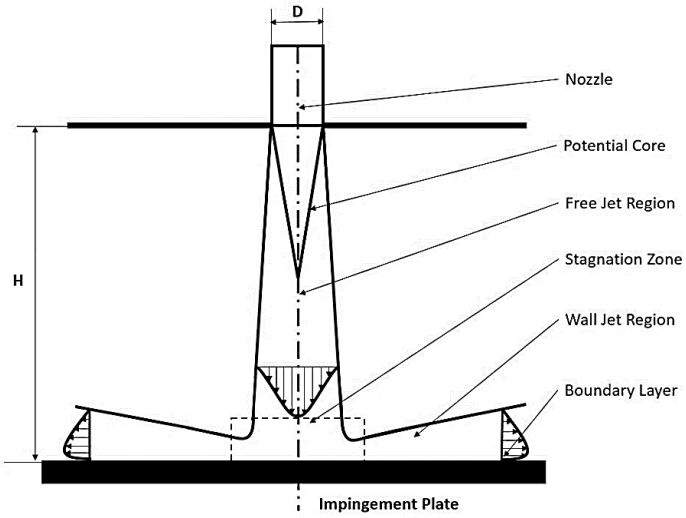

Figure 1.1. Schematic diagram of a normal impinging jet. The flow consists of the free jet region, stagnation zone, and wall jet region. The boundary layer develops as jet impinges on the surface and creates the flow parallel to the surface.

The experimental studies by *Donaldson and Snedeker* [12] using Schlieren gives a detailed insight into the complex shock structure of the supersonic jet. They examined the shock structure development and concluded that it primarily depended on the nozzle pressure ratio and the standoff distance of the jet. For a free jet without an impingement plate, the oblique shocks alone expand the flow and render the flow subsonic. This is seen in impinging jet configurations with high standoff distances. However, in some jet configurations, the airflow onto the plate may still be supersonic, and this leads to the formation of a normal shock ahead of the plate. Across this shock, the flow transitions to subsonic, and is deflected to the wall jet region near the plate. For higher standoff distances, maximum pressure occurs at the centerline of the jet on the impingement plate. For very small standoff distances, researchers have observed the formation of a stagnation bubble at the impingement region [13]. For these cases, the maximum pressure was observed to occur off the center.

A great deal of computational research is related to the supersonic impinging jet. Most of the CFD studies in this field [14-16] have employed the RANS models, which used lesser

computational memory and time to yield good predictions with respect to the experimental data. *Alvi et al.* [14], looked at solving for the flow field using different turbulence models and compared them to experimental velocity measurements. They used $k-\omega\ SST$ and Spalart Allmaras with curvature correction and observed that they produced nearly identical results. While these studies are comprehensive and important to the understanding of underexpanded impinging jets, there is a lack of investigation into the wall jet region and, specifically, the wall shear stress developed along the plate.

The problem has been investigated for subsonic and mildly sonic jets experimentally in the past. *Young et al.* [17] used oil-film interferometry to measure the shear stress from a supersonic impinging jet. The experiment was limited to a single jet pressure ratio, and therefore, one can not draw any conclusions on the effect of pressure on the flow characteristics of the impinging jet and on the wall shear stress, as well as the limits of the scope of the results to mildly sonic jets. *Tu & Wood* [18] conducted a comprehensive study of wall shear stress developed from a subsonic impinging jet, but their conclusions cannot be extrapolated to account for supersonic and compressible effects.

Smedley et al. [19] and *Phares et al.* [20] investigated a normally impinging jet on a glass plate containing microspheres and used previous results of theoretical shear stress profiles, adhesion forces, and particle removal rates to infer shear stress along the plate. They determined that the maximum shear stress was directly related to the Reynolds Number of the jet and was directly proportional to the H/D ratio. They also concluded that the axial location of the maximum shear will be at r/H = 0.09 for all cases of the jet with H/D > 8. Their results find the shear stress to be directly related to particle forces, but do not account for compressibility and turbulent effects. These conclusions were produced for subsonic and nearly sonic jets, and its applicability for highly

underexpanded jets, where the flow is compressible in the wall jet region, is uncertain. Shear stress is the correct parameter to analyze, but it must be used along with the entire boundary layer profile to understand the forces acting on the particle.

Even with full confidence in the results discussed above, it still has been shown that the shear stresses obtained for the jets examined in these experiments and models do not reach the critical shear stress needed for the successful removal of typical explosive particles. *Keedy et al.*[5] used *Birch's* [21] model for the virtual origin of underexpanded jets as their jet parameter (i.e., the origin of hyperbolic velocity decay) and demonstrated that trace explosive particles could only be removed if the impingement plate is within the distance of the virtual origin. The scenarios of interest have been extrapolated using a Mach number correction by *Smedley et al.* [19], but have not been investigated directly. Further investigation into underexpanded jets is necessary to determine the parameters of the impinging jet required to obtain the levels of shear stress needed for particle removal.

2.2 METHODOLOGY

The presented work is aimed at the characterization of wall shear stress resulting from the impingement of the normal axisymmetric jet and includes both numerical and experimental studies. Our research methodology consists of: (i) the development of the CFD model for an underexpanded air jet, (ii) the validation of the numerical results by comparison with Schlieren images, and (iii) the analysis of the CFD results to determine wall shear stresses over operational parameters of interest. Our numerical and the experimental matrix contains two jet parameters: nozzle pressure and the H/D. Only normal jets were considered in this study; a straight pipe with fully developed flow is used as a nozzle. We thus developed a Dimensionless Jet Parameter that

quantifies the wall shear stress for any location on an impingement surface for a wide range of pressure ratios and H/D combinations.

2.2.1 *Computational Study*

A computational study provides an insight into the flow field with all its necessary characteristics: shock structures and the velocity field near the wall; this is a simple, yet effective, way to calculate wall shear stresses for a range of operational parameters. The computational analysis is performed using the commercial software code ANSYS FLUENT 16.2 and a cell-centered finite volume approach. The steady-state Reynolds and Favre Averaged Navier-Stokes equations are solved to obtain the flow field.

CFD solvers can be classified as two distinct families of schemes: pressure-based and density-based methods. Previously, pressure-based methods were created for incompressible flows and flows with low Mach number flows, while the density-based methods have typically dominated transonic and supersonic simulations encountered in traditional aerodynamics applications. In the pressure-based method, a pressure equation is derived from the continuity and the momentum equations in such a way that the velocity field, corrected by the pressure, satisfies the continuity. Whereas for the density-based solver, the solver solves the governing equations of continuity, momentum, and (where appropriate) energy and species transport simultaneously. Typically, the pressure-based solver was created for incompressible flows. But it has been modified through the introduction of pressure-velocity coupling, which solves for pressure from the continuity and momentum equations, taking into consideration the effect pressure has on both the velocity and density [22]. This coupling uses either a pressure-based segregated algorithm or a coupled algorithm. The pressure-based coupled algorithm offers superior performance to the segregated algorithm and also aids with better numerical convergence. This forms an alternative

to the density-based solver. Although nearly all numerical simulation cases in this work include the supersonic region Ma > 1, where density solver may be beneficial, the majority of the flow in the wall jet region is subsonic. Thus, the use of the coupled pressure-based solver is more appropriate for this study [23]. A second-order scheme was used for the pressure, whereas a third-order MUSCL scheme was used for density, momentum and turbulence, which was necessary to avoid the effects of numerical viscosity (associated with the first-order schemes) on the jet dissipation, as well as pressure strain relationship. Since the flow is also associated with changes in temperature, the Sutherland model, which is based on the on kinetic theory of ideal gases and an idealized intermolecular-force potential, is used for viscosity.

The choice of the turbulence model takes into account the need to accurately capture the wall shear stress. Since the main focus of this analysis was on the wall jet region, we needed a model that resolves the viscous boundary layer well. The standard $k-\omega$ model suffered from errors around the near-wall region, which was resolved using the modified using the $k-\omega$ SST model [24]. According to *Catalano* [25], as $k-\omega$ SST is less stiff, it requires less computational effort. Based on the study by *Alvi et al.*, [14] the $k-\omega$ SST model showed results quite similar to the actual data obtained. Hence, the most suited option based on an accurately resolved flow field was the $k-\omega$ Shear Stress Transport model.

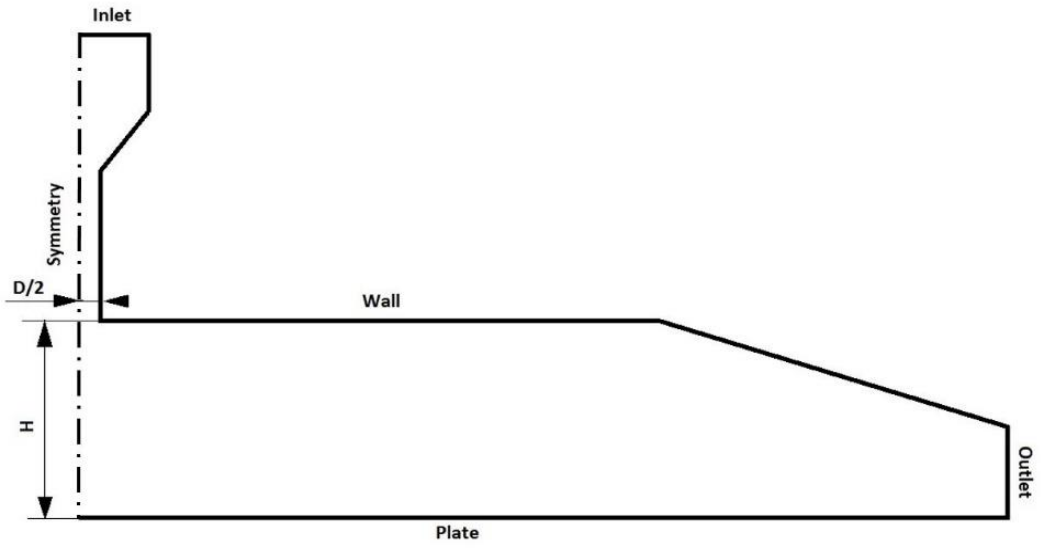

Figure 2.1. Computational Domain (not to scale). Note that only half the domain is modeled due to the presence of symmetry. The inlet is supplied with gauge pressure, plate follows the model of a no-slip wall and outlet represents the open atmosphere (0 psig).

A schematic diagram of the computational domain is shown in Figure 2.1 is used for simulations taking advantage of the jet's axial symmetry. The nozzle radius (D/2) and the standoff distance to the impingement surface (H) were varied depending on the case. The converging section of the top wall does not represent the exact experimental setup but was introduced into the CFD to aid with the solution convergence by minimizing the exit plane flow recirculation. This converging section has very low velocities, and, as a result, does not change the boundary layer properties in the vicinity of the area of study.

The mesh primarily comprises of quadrilateral elements, and for the majority of simulations, after conducting mesh independence studies, the size of the mesh is around 250,000 elements. To obtain the wall shear stress, the near wall properties have to be captured, and this is done by resolving the viscous sublayer. The viscous sublayer is of a thickness of $y^+ = 5$. To resolve this, at least three cells have to be placed within this region, so that the mesh at the impingement surface is created such that its first grid point is located at a distance of $y^+ \approx 1$. The typical size of an element within the impinging surface is of the order of 1 micron. For the boundary conditions, the

inlet of the domain is supplied with air at a specific gauge pressure measured experimentally by a pressure transducer. The impinging jet is kept open to the air and to model this, the outlet is kept far away from the inlet and is forced to be at atmospheric pressure (zero-gauge pressure). The axis of symmetry is conditioned to have no crossflow across it, and the walls are modeled as non-slip boundary.

2.2.2 *Experimental Setup*

The greatest uncertainties in the CFD simulations are the length and the structure of the supersonic jet region, and the interaction of the supersonic jet with the impingement plate. While there are several publications describing the interaction between the supersonic jet and the surface, these are limited to a few H/D ratios, and the jet pressures [15]. To perform any meaningful comparisons between the CFD and the experimental fluid dynamics, we have designed and performed a series of flow visualization experiments (Fig. 2.2).

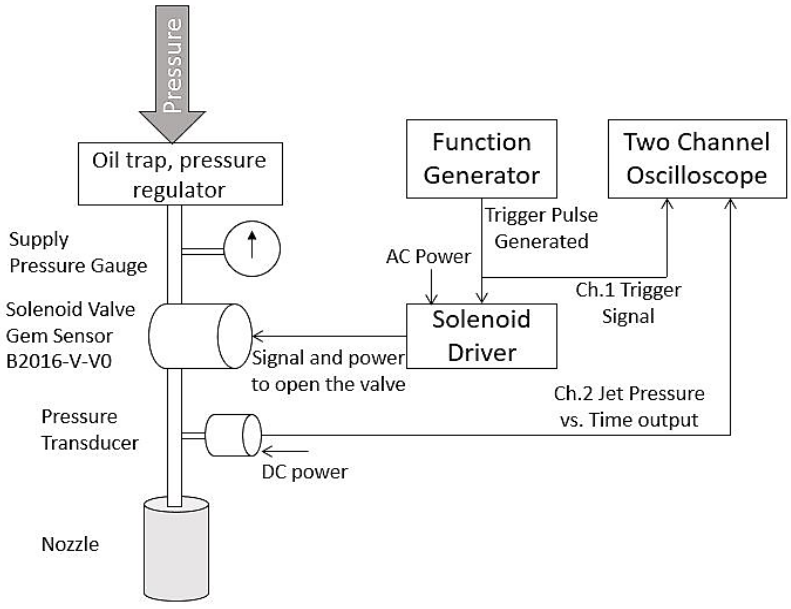

Figure 2.2. Schematic of Experimental Impinging Jet Setup. Supply pressure was regulated through the supply pressure gauge and measured precisely using an electronic pressure transducer. The flow was regulated using an AC solenoid. The flow field was then captured using Schlieren Imaging.

A normal impinging jet system was built on the optical table. Two long constant diameter nozzles are used to allow for the flow to fully develop while the standoff distance and pressure are adjusted to match the designed parameters. The pressure is then controlled by a regulator connected to conditioned shop air (RH~0%). The timing is controlled by a solenoid valve operated by an arbitrary function generator. The 1-second pulse width was used in this study. The pressure transducer downstream of the solenoid valve is used to measure the pressure in the nozzle. This nozzle pressure was then matched to the CFD boundary conditions as the inlet nozzle pressure. In the experiments, the nozzle was at a fixed location, and the location of the impingement plate was adjusted to the desired height to diameter ratio (H/D) for the impinging jet.

Schlieren imaging was used to visualize the flow patterns of the impinging jet. Schlieren imaging uses the refraction of light through media of variant density to visualize the density gradient of compressible flow. For our visualization, a z-type Schlieren setup was implemented. A halogen light bulb with a focusing lens and an optical slit was used as a point light source with spherical mirrors to collimate the light rays through the test section and to refocus the light onto a razor's edge, which blocks the refracted rays, allowing the camera to capture an image of the density gradient [26].

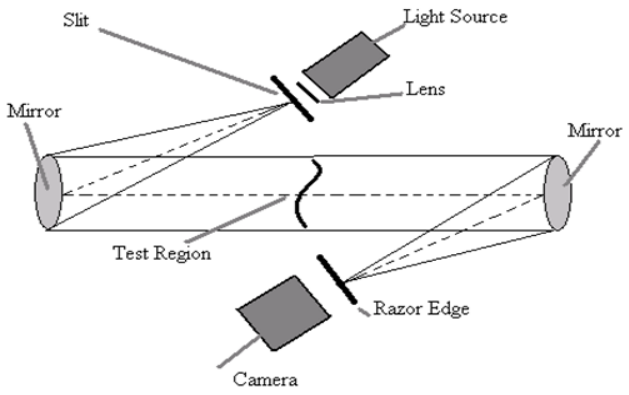

Figure 2.3. Schematic of the z-type Schlieren set up used to visualize the flow

2.3 RESULTS

2.3.1 *Computational Model Validation*

The supersonic underexpanded jet is associated with a series of expansion waves at the exit of the nozzle, and may also be accompanied by a plate shock based on the ratio of the standoff distance of the jet to its diameter (H/D ratio). These formations are characteristics of the underexpanded jet, and hence validation of the CFD model would be obtained through an accurate prediction of the behavior in the under-expanded (supersonic) region of the jet—specifically, within the interaction between the shock wave pattern in the presence of the wall. Figure 2.4 presents a schematic of an underexpanded impinging jet.

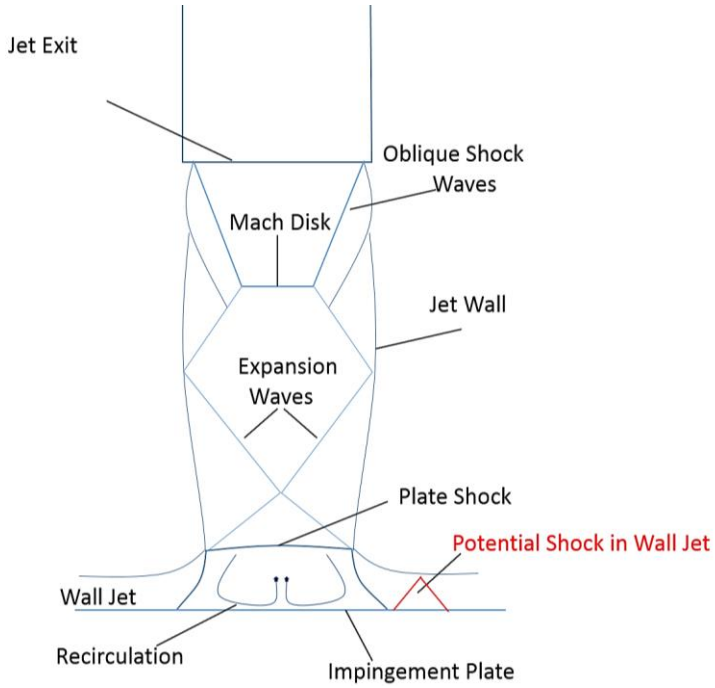

Figure 2.4 Schematic of underexpanded impinging jet. Key characteristics are outlined. The presence of supersonic flow extending to the impingement point results in a normal plate shock, which dissipates energy, resulting in less efficient removal. If the pressure in the recirculation zone is high enough, a shockwave in the wall jet region may form.

To examine the capabilities of the numerical simulation to reproduce the features of the flow, the CFD results are compared with the experimental data (in this case, Schlieren images). Thus, for the purpose of validation, the numerical simulation was run for the case of the H/D ratio of 5, with three different inlet pressures and their density contours compared against their Schlieren counterparts as shown in Figure 2.5.

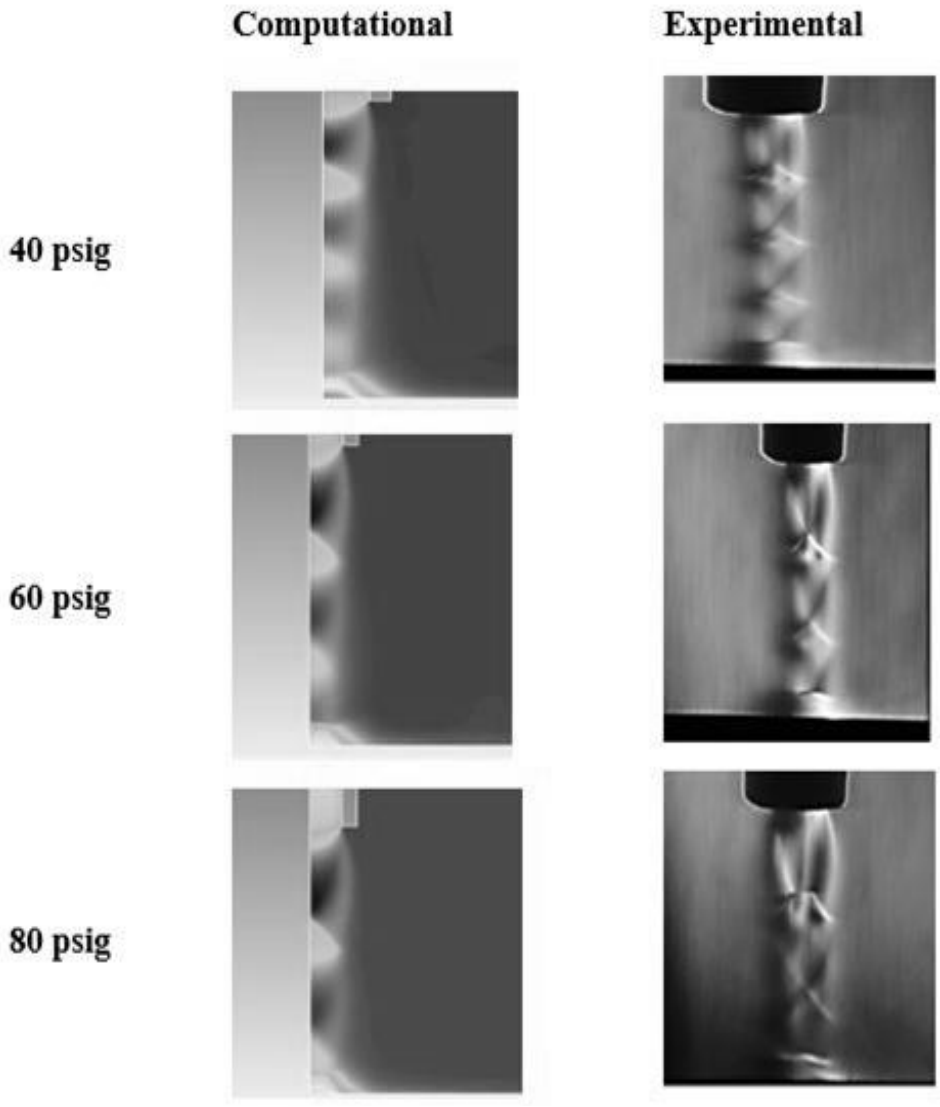

Figure 2.5 Density Contours of the CFD model and Schlieren Images at a height to diameter ratio of 5. The number of shock cells decreases with increasing pressure, but they get stronger. The oblique shock cells and the plate shocks produced by CFD are in agreement with the Schlieren images.

The Schlieren images align quite well with the CFD contours. Similar results were obtained for an H/D of 10, but are omitted in the interest of brevity. The shock cells seem to decrease in number, but increase in strength as the inlet pressure is increased. As the H/D ratio is increased, more shocks cells formed in the free jet region. This comparison confirms that the chosen simulation approach is the appropriate tool for evaluating the flow field for an underexpanded impinging jet.

2.3.2 *H/D Parameter Validation*

The z-type Schlieren setup was used to examine the flow field of impinging jets of two different diameters and across a variety of the pressure ratios to affirm the previously determined self-similarity parameter of impingement height divided by jet diameter (H/D).

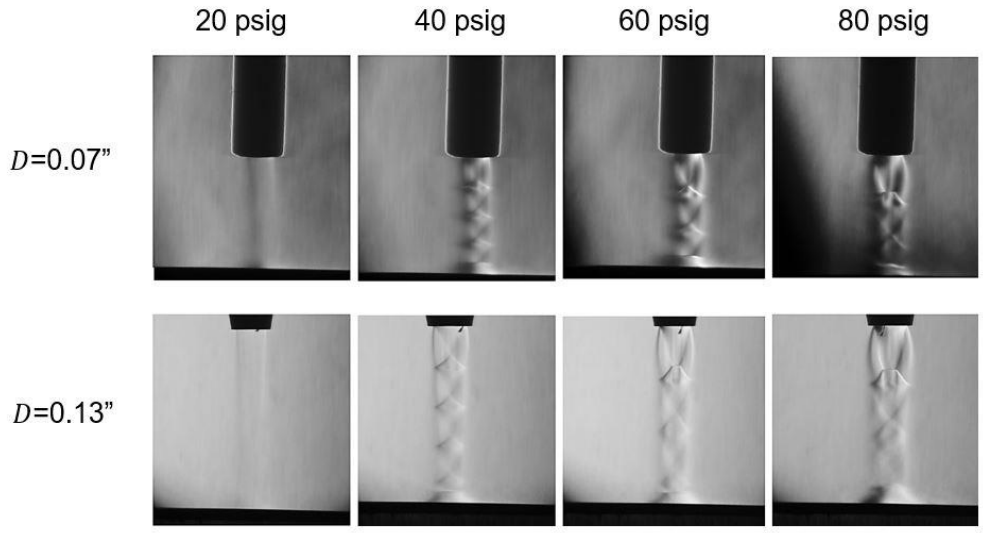

Figure 2.6 Experimental Verification of H/D as a Similarity Parameter. Normally impinging jets of similar H/D, supplied with the same inlet pressure, produce the same flow pattern.

The images from Figure 2.6 confirm the self-similarity of impinging jets using the height to diameter ratio. For each case of different pressure ratios, the relative size, location, and the number of shocks are the same.

Previous researchers and the Schlieren images in Figure 2.6 have helped identify H/D as a similarity parameter. To be confident moving forward, the CFD model is used to verify H/D similarity by looking at the wall shear profiles for different jets with the same H/D ratio. Figure 2.7 plots the profile of shear stress along the impingement plate for several different diameters with the height adjusted to maintain the same H/D.

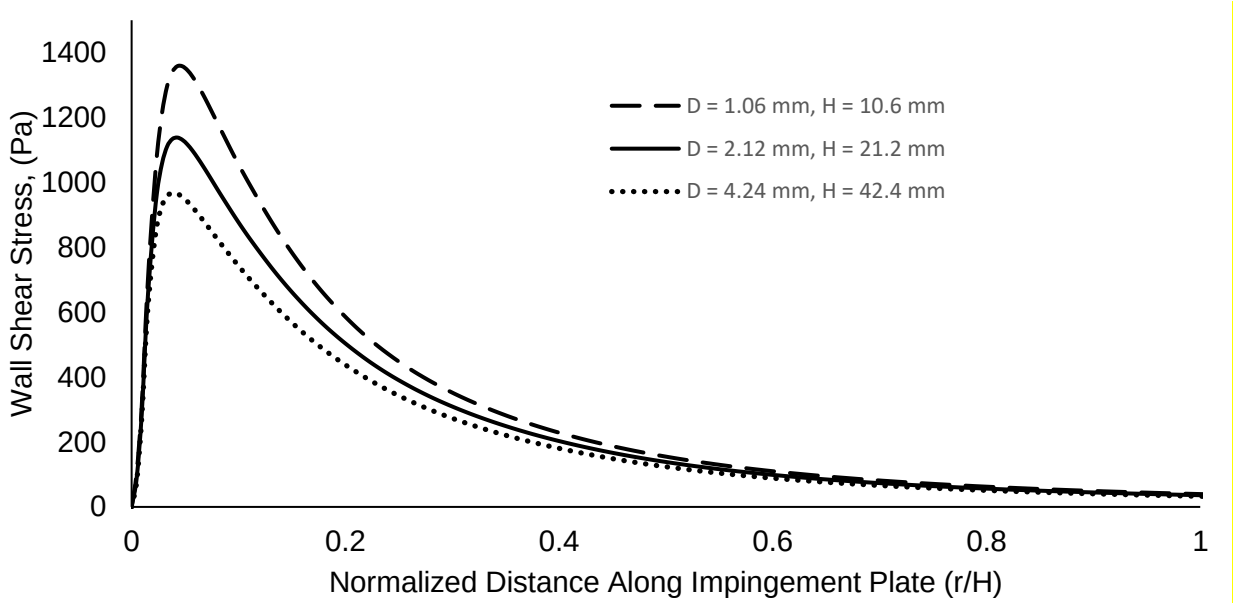

Figure 2.7 Experimental Verification of H/D as a Similarity Parameter. Normally impinging jets of similar H/D, supplied with the same inlet pressure of 40 psi, produce the same shear stress profiles but different maximum values.

Figure 2.7 shows how the shear stress profiles are not identical across the three different jet diameters (changing the impingement height to keep the H/D constant), as was expected. After further investigation changing the diameter while fixing H/D does not affect the location of the maximum shear stress or how the sheer stress decays along the impingement surface. This means that when adjusting for diameter, only the magnitude of the shear stress must be accounted for. It was found that the maximum wall shear value for constant pressure and H/D scales with the inverse of the fourth root of the diameter such that:

$$\frac{\tau_a}{\tau_b} = \left(\frac{D_b}{D_a}\right)^{\frac{1}{4}} \tag{2.1}$$

The dependency of wall shear stress on jet diameter and height independently of the H/D ratio is due to the increase in turbulent or effective viscosity with larger Reynolds number, leading to more momentum loss in the impinging jet region. Moving forward, all simulations were conducted for a diameter of 2.12 mm, and all equations may be adjusted appropriately to specific applications.

2.3.3 *Wall Shear Stress*

On establishing confidence in the CFD model, forty separate cases are run, which span eight different H/D ratios (5, 10, 15, 20, 25, 30, 40, and 60) and five separate jet pressures (20:20:100 psig). Initially, the wall shear stress profiles were examined for all cases to understand the overall trends. Figure 2.7 shows these profiles for three H/D ratios across all pressures, by plotting τ against a normalized distance along the plate of the radial distances divided by the impingement height (r/H).

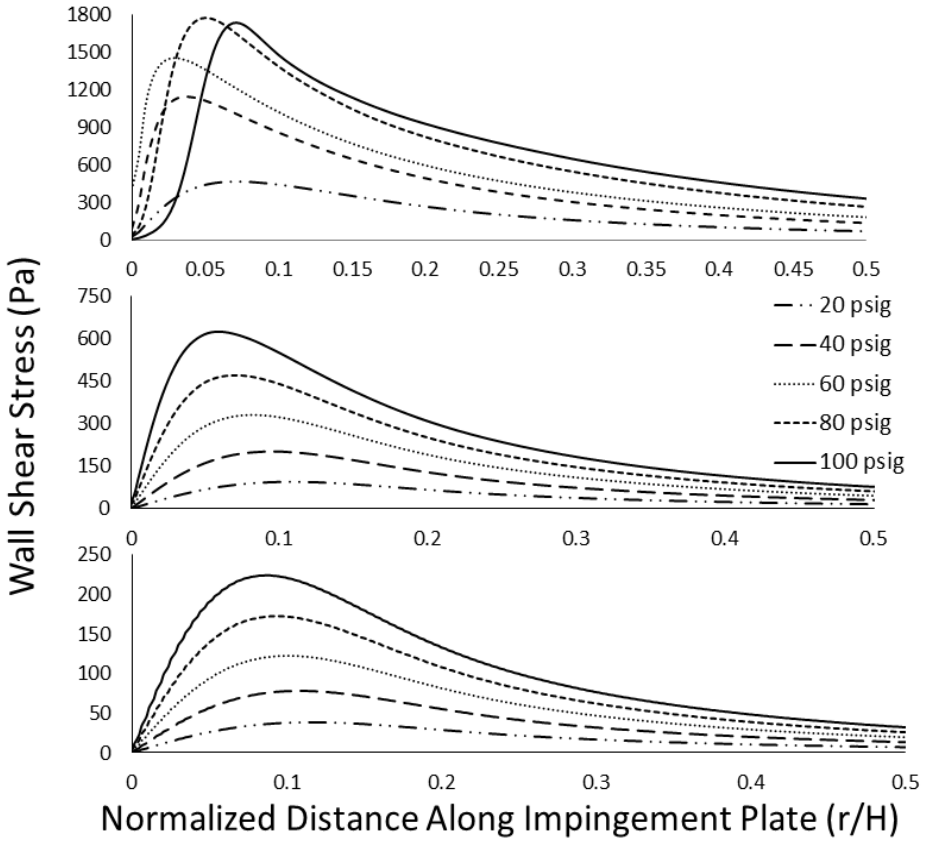

Figure 2.7 Wall Shear Stress Distribution for H/D of 10, 20, and 30 at gauge pressures of 20, 40, 60, 80, and 100 psig. The plots show the change in maximum wall shear stress magnitude and location.

The effect of the increasing pressure ratios and increasing H/D on the wall shear is visible through Figure 2.7. As the inlet pressure is increased, the wall shear stress along the plate increases. And, similarly, wall shear stress is seen to increase as the standoff distance to the plate is decreased. Amongst the two parameters, the effect produced by changing H/D on the wall shear stress is greater than that caused by the inlet pressure, i.e., the decrease in H/D produces a larger increase in the wall shear than that produced by increasing the inlet pressure. This pattern is noted for all cases until supersonic flow begins to appear at the wall jet region, which is seen in Figure 2. 8 for H/D=10 and pressures of 80psi and 100psi.

It is immediately noticeable for supersonic impingement that the location of the max shear is not consistent with regards to r/H as was found for subsonic jets [19], [20], and [17]. There is a

clear effect of pressure, as well as H/D, on the location of the maximum shear stress. This is especially true for the H/D = 10 case. In this case, supersonic flow is present in the wall jet region of the flow. The effect of the supersonic flow along the wall jet region is difficult to characterize and is thus beyond the scope of this paper.

The goal of this research is to characterize the wall shear stress based upon the impinging jet parameters. When analyzing the trends, it was found that the peak wall shear can be directly related to a single dimensionless jet parameter. We found that the maximum wall shear stress value tended to go as the inverse of $(H/D)^2$ and is directly proportional to the ratio of the jet gauge pressure over the atmospheric pressure. We then investigated how to appropriately adjust the H/D ratio to obtain a certain shear stress at a variety of pressure ratios. Consistent with our expectations, if the pressure is decreased by a factor of "X", then to achieve the same wall shear stress, the H/D must be reduced by a factor of $\sqrt{X}$. This led us to develop the dimensionless jet parameter:

$$DJP = \frac{\alpha * \left(\frac{P_{gauge}}{P_{atm}}\right)}{\left(\frac{H}{D}\right)^2} \tag{2.2}$$

Where α = 46.3 normalizes, from zero to one, the range where the *DJP* can be accurately used to characterize the impinging jet. The physical representation of DJP = 1 is that the length of the supersonic region of a free (non-impinging) jet at the given pressure ratio would be at the standoff distance of the jet.

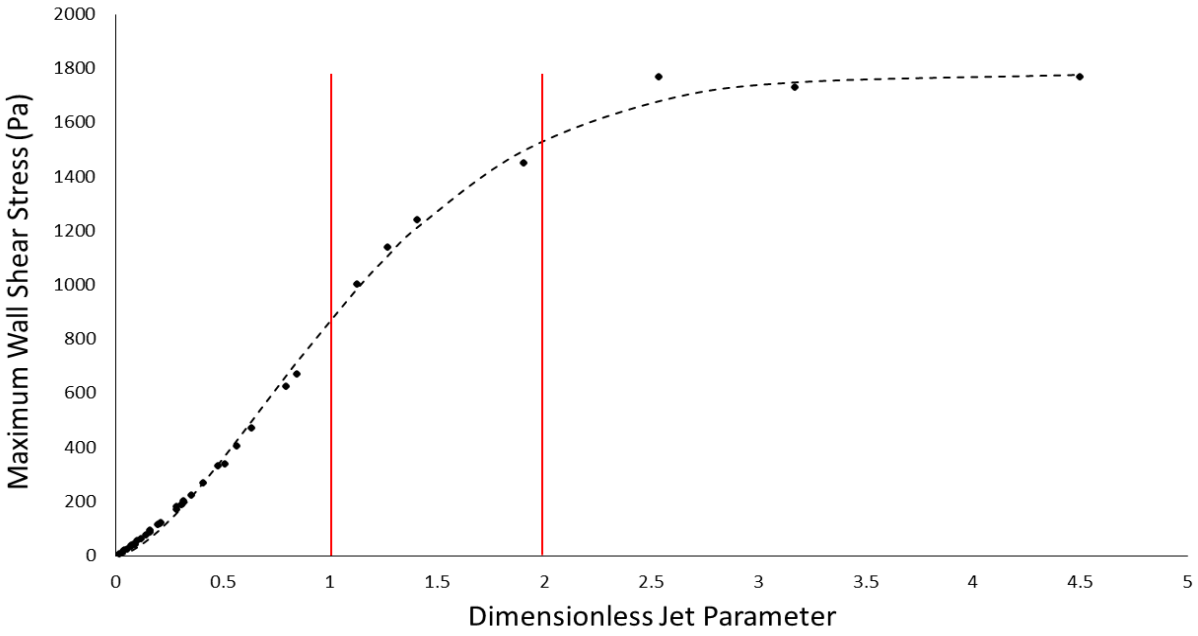

Figure 2.9 Maximum wall shear stress vs. DJP with lines separating the subsonic, transitional, and supersonic wall regions. For DJP greater than 1, the maximum shear stress asymptotically approached the maximum value limit.

Figure 2.9 displays all scenarios of the underexpanded impinging jet examined for this work. The three distinct regimes can be seen clearly in Figure 2.9. An exponential trend line is developed in Eq. (3) to capture the entire range of *DJP*'s. This trend is not accurate enough to be used for small values of *DJP*, but works in the transitional regime, capturing the maximum value in the supersonic impingement regime.

$$\tau_{max} = 1780(\,1 - e^{-(0.775*DJP)^{1.57}}) \tag{2.3}$$

When removing the data points with *DJP* greater than unity, a more accurate trend can be defined with a second-order polynomial fit. For comparison, we plotted our models with the equation for maximum shear stress using the Mach number correction developed by *Phares et al.* [20].

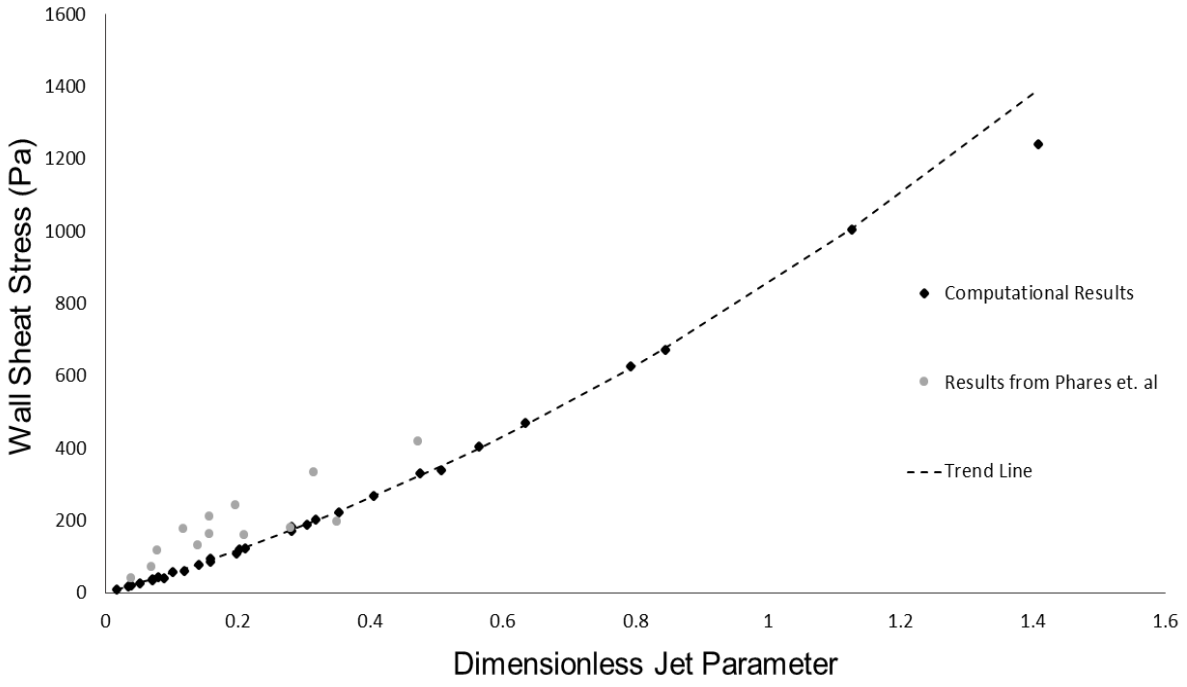

Figure 2.10 Plot of the Variation of Peak Wall Shear Stress with the Dimensionless Jet Parameter with data using the equations developed by Phares et al.

It is clear that the results from *Phares et al.* [20] cannot be consistently extended to underexpanded impinging jets. Using the Dimensionless Jet Parameter, we can accurately determine the maximum shear stress from underexpanded impinging jets using a single quadratic trend line equation, as shown in Figure 2.10 with Eq. (4). The trend was expected to be linear, but at the higher pressures and smaller H/D, the flow is compressible on the impingement plate, and these effects are most likely responsible for the second-order relationship. The trend represents all of the data for $DJP < 1$ within 5% of the computed value.

$$\tau_{max} = 327.01 * DJP^2 + 526.98 * DJP \quad (2.4)$$

For the application of particle removal, it is important not only to know what the maximum shear stress magnitude, but also the location of the maximum and the rate of decay of the shear stress on the impingement plate. In the subsonic impingement regime, the square root of the *DJP* was shown to be linearly related to the location of the maximum shear normalized by

the impingement height of the jet. In the transitional and supersonic impingement regimes, the max shear location was shown to move inside the radius of the jet and becomes unpredictable using the *DJP*.

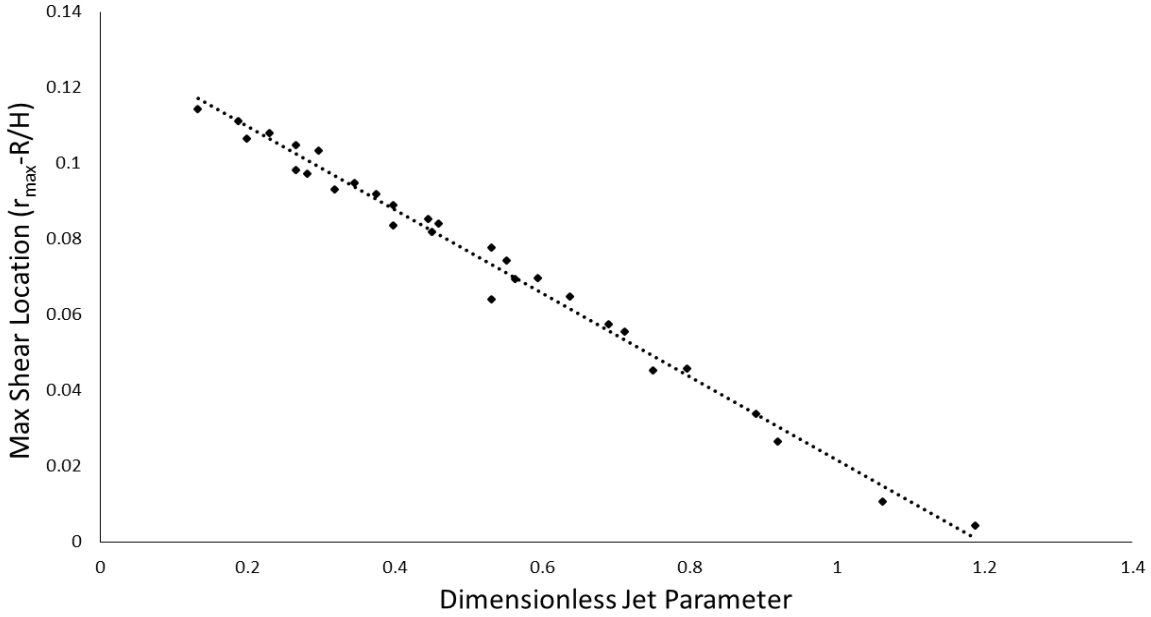

Figure 2.11 Plot showing the effect of the Dimensionless Jet Parameter on the Peak Wall Shear Location

To better represent the physics of the impinging jet, the radius of the jet is subtracted from the radial location of the max shear. The trend line for the max shear location is given by Eq. (5). As the DJP goes to zero, the peak location approaches the tangent of 7.5°, which is the spreading angle for subsonic jets, thus being the limit for the location of the maximum shear. It should also be noted that as the length of the supersonic region approaches the impingement height, the location of the max shear approaches the radius of the jet. This is because the supersonic region of the jet does not expand as the subsonic region does. The compressibility of the air at high velocity is responsible for the shifting of the maximum shear location towards the impingement point as *DJP* increases.

$$\frac{(r_{max} - R)}{H} = \tan(7.5°) - 0.11 * \sqrt{DJP} \quad (2.5)$$

Now that we can locate the maximum wall shear, we can determine how the shear decays along the plate. We define a new variable r^*, where $r^* = 1$ at the location of the maximum shear for each case, and zero at the center of the impingement point of the jet.

$$r^* = \frac{r}{r_{max}} \quad (2.6)$$

Using the r^* variable, we can then characterize the decay of the shear stress on the plate. A $\frac{1}{r^{*2}}$ relationship was initially assumed for the decay, but it was found that an exponential decay more accurately depicts the decay of the shear stress. We then use an equation to characterize the shear stress away from the peak location.

$$\tau = \tau_{max} * e^{\beta(1-r^*)} \quad (2.7)$$

Using Eq. (7), β was optimized for minimum error in the shear stress profile for each case run on our model. It was found that β is also directly related to the *DJP*. We could then come up with a trend for β and thus have the ability to determine shear stress along all of the locations of the plate based solely on the Dimensionless Jet Parameter.

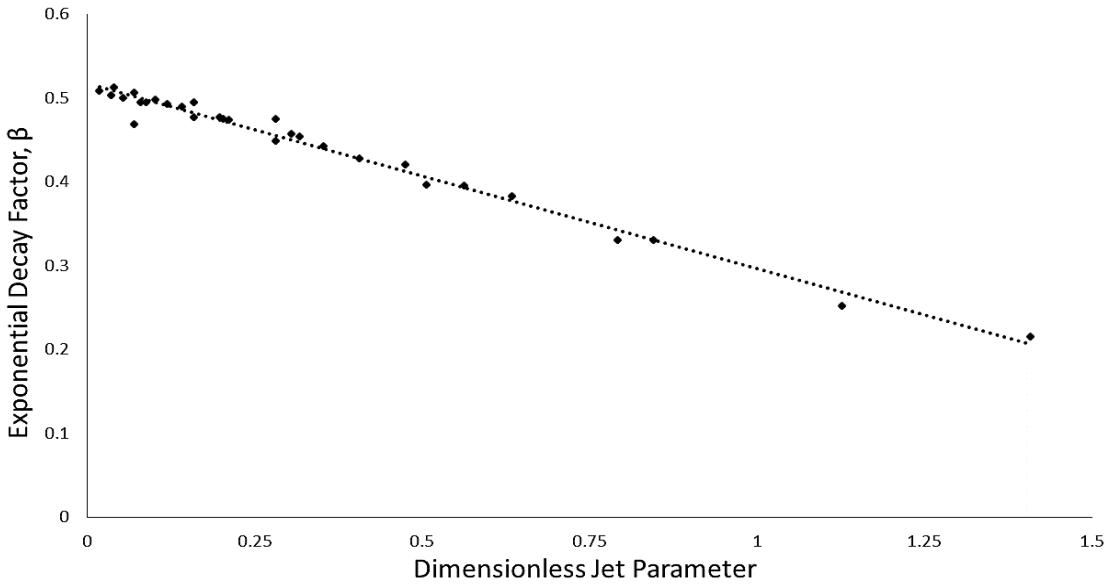

Figure 2.12 Effect of Dimensionless Jet Parameter on Exponential Jet Decay Factor

The trend line from Figure 2.12 gives us Eq. (8), which allows us to determine the decay factor as a function of the *DJP*.

$$\beta = -0.2204 * DJP + 0.5171 \tag{2.8}$$

Using the trends developed for the maximum shear stress along the wall τ_{max}, the maximum shear location r_{max}, and the exponential decay factor β, we can then use Eqs. (6) & (7)as a function of a single variable, *DJP*, to characterize the entire shear stress profile along the impingement plate for a wide range of underexpanded axisymmetric impinging jets.

2.4 Conclusions for Axisymmetric Underexpanded Impinging Jets

In this chapter, we have developed the Dimensionless Jet Parameter that can be used to characterize the wall shear stress profile on the impingement plate for the wide range of flow conditions. The *DJP* includes two principle components: nozzle pressure to ambient pressure ratio and the nozzle stand-off to nozzle diameter ratio. The relationships presented in this work are valid for normal axisymmetric jet. The best agreement for all parameters is obtained when *DJP* value is directly proportional to the pressure ratio and inversely proportional to $\left(\frac{H}{D}\right)^2$. The order of the

terms is determined by their relationship to each other. For every factor of X that the pressure is increased, the H/D ratio needs to be increased by a factor of $\sqrt{X}$ to result in similar wall shear stress profiles. It was also found that the diameter of the jet has a slight effect on wall shear stress independently of the DJP. This relationship was found to be accounted for in a simple adjustment such that for a fixed DJP, the ratios of shear stress will be proportional to the inverse of the fourth root of the ratio of diameters.

To indicate the valid operational conditions for developed relationships, *DJP* was normalized. The physical representation of *DJP* = 1 is that the length of the supersonic region of a free (non-impinging) jet at the given pressure ratio would be equal to the impingement height (or stand-off distance) of the jet. At *DJP* values greater than unity, supersonic flow in the wall jet region is observed experimentally and in the numerical simulations. The presence of the supersonic wall jet significantly complicated the analysis and hence the mapping of wall shear stress is restricted to subsonic flows of the wall jet. As a result, the *DJP* has been normalized to be in a range of 0 to 1, beyond which the use of the *DJP* is not validated for use in locating wall shear stress.

The maximum aerodynamic forces acting on the particle in the boundary layer will be at the location of the maximum shear stress assuming the viscous non-slip wall boundary layer condition. Finding the maximum values of the wall shear stress and its location is necessary for particle detachment studies and aids in the design of the non-contact sampling devices. The maximum wall shear stress in the subsonic impingement regime can now be calculated. The trend for maximum wall shear stress for lower values of *DJP* (0–0.2) is nearly linear. This corresponds to incompressible flow along the impingement surface. At higher values of DJP (> 0.2) the quadratic term is dominant. This term demonstrates that compressible flow along the

wall allows for much higher shear stress, and more efficient transfer of shear stress for design criterion trade off ($(H/D)^2$ and P_{gauge}/P_{atm}) than incompressible flow.

It was also found that when the DJP is greater than unity, there is a loss of return in the power requirement as the shear stress is limited due to the increase in energy dissipation in the normal (plate) shock wave that forms at the impingement point. In the transitional regime ($1<DJP<2$), the wall stress asymptotically approaches its maximum value limit. The maximum increase of the wall stress will be about 150% of the shear stress at $DJP = 1$. This is not well defined by the relationships developed in this work. In the supersonic wall flow region ($DJP>2$), the value of the maximum wall shear stress can be exceeded (though not significantly or predictably). To describe the supersonic wall jet region, additional CFD simulations and experimental validation experiments are needed. The non-slip assumption of the wall flow at the $DJP>1$ are not likely to be valid as the flow becomes unstable, which was observed by the high-speed Schlieren visualization. This topic is beyond the scope of this manuscript. In addition, achieving the supersonic conditions at the surface is not practical for most engineering applications due to power and nozzle standoff requirement.

For $DJP<1$, the location of the maximum shear stress was found to be consistent with the jet expansion angle. The radius of the nozzle is subtracted from the radial location of the max shear to account for the shift due to the nozzle geometry. As the DJP approaches zero (low nozzle pressure and larger stand-off distance), the peak location approaches the tangent of 7.5°, which is a typical value for a spreading angle for subsonic jets. It should also be noted that as the length of

the supersonic region approaches the impingement height, the location of the max shear approaches the radius of the jet.

Observing the decay of the wall shear profile from its point of the maximum, an equation led to the derivation of an exponential decay equation. The decay factor for the exponent is also a function of the DJP and, hence, using this similarity parameter, the shear stress along the plate can be mapped for different normally impinging jets.

The limitation of the presented relationship is related to both operational and geometrical considerations. While these results are validated for the normal axisymmetric jet in subsonic impingement scenarios, several parameters can influence the maximum values and location of wall shear stress, as well as the wall shear mapping on the surface. Among these parameters are: (i) high Mach number (> 1) at the impingement location and the presence of shocks at the surface; although these were observed both experimentally and in the CFD simulation, their effect has not been quantified in this work. (ii) Nozzle shape and the nozzle aspect ratio affect flow conditions at the nozzle exit and, thus, will have an impact on the wall shear stress. A nozzle correction factor could be developed in future work to account for over-expanded nozzles. (iii) Jet angle will also have a significant impact on the wall shear stress.

Chapter 3. WALL JET SIMILARITY OF IMPINGING PLANAR UNDEREXPANDED JETS

This work is published in the International Journal of Heat and Fluid Flow[27].

Velocity profiles and wall shear stress values in the wall jet region of planar underexpanded impinging jets are parameterized based on nozzle parameters (stand-off height, jet hydraulic diameter, and nozzle pressure ratio). Computational fluid dynamics is used to calculate the velocity fields of impinging jets with height-to-diameter ratios in the range of 15 to 30 and nozzle pressure ratio in the range of 1.2 to 3.0. The wall jet has an incomplete self-similar profile with a typical triple-layer structure as in traditional wall jets. The effects of compressibility are found to be insignificant for wall jets with Ma<0.8. Wall jet analysis yielded power-law relationships with source dependent coefficients describing maximum velocity, friction velocity, and wall distances for maximum and half-maximum velocities. Source dependency is determined using the conjugate gradient method. These power-law relationships can be used for mapping wall shear stress as a function of nozzle parameters.

3.1 INTRODUCTION

Planar impinging jets have been studied extensively; their characterization is useful in biological, chemical, and engineering applications. These studies tend to focus on heat and mass transfer [28-31]. The goal of this work is to analyze the properties of the wall jet originated from the impingement of underexpanded planar jets, with application to aerodynamic micro-particle sampling. Previous studies of underexpanded jets have generally been motivated by the flow dynamics and acoustics of short takeoff and vertical landing aircraft [9,10,32]; thus, the jets of interest were axisymmetric, and the wall jet region has not been the primary focus. The main advantages of using underexpanded planar jets for the removal of micro-particles from a surface are: (i) planar

jets provide an advantage over circular jets as the velocity in the wall jet sustains further from impingement, (ii) planar jets cover a larger area where the particle is removed, (iii) supersonic jets produce high wall shear stress in the wall jet region, (iv) isentropic nozzle relations allow for straightforward calculations of fluid properties at the jet exit, convenient for numerical and experimental studies.

For characterization of aerodynamic particle resuspension, it is useful to characterize the wall shear stress resulted from jet impingement. Measurements of wall shear stress are challenging; for example, Young *et al.* [17] used oil-film interferometry to measure the shear stress from an impinging supersonic jet. Their experiment has shown promise, but oil-film interferometry is limited in its precision. Tu & Wood [33] conducted a comprehensive study of wall shear stress developed from a subsonic impinging jet using Preston and Stanton tube measurements, but their results were affected by the measurement apparatus, and their conclusions cannot be extrapolated for compressible jets. Velocity measurements near the wall can be used to elucidate the values of the shear stress. Loureiro [34] demonstrated Laser Doppler Anemometry (LDA) could be used to measure velocity within 50 micrometers of the wall accurately; but, in boundary layers with the necessary wall shear stress to remove trace explosive materials, the viscous sublayer may be only 20 micrometers thick [35]. In general, there is a scarcity of reliable wall shear stress data in the scientific literature, especially for compressible and planar impinging jets.

3.2 WALL JET THEORY

For mapping of flow properties near the surface and wall shear stress, it is useful to examine the wall jet portion of the flow from a similarity perspective. Figure 3.1 shows the schematic diagram of the impinging jet system. Similarity variables are obtained by normalizing by x-dependent variables; y_m - wall-normal location of maximum velocity, $y_{1/2}$ - wall-normal location

of half-maximum velocity in the outer layer, u_m - maximum wall jet velocity, and u_τ - wall jet friction velocity. The planar turbulent wall jet has consistently been shown to have incomplete similarity, which is to say that a non-dimensional similarity solution cannot describe the velocity profile of the wall jet without Reynolds number or scale dependence. Thus, one must separate the wall jet into three regions: a self-similar wall layer where viscous forces are dominant, a self-similar outer layer which behaves analogously to a free jet, and an overlap layer with source dependence where the velocity is closest to the maximum. A triple-layered incomplete similarity is achieved by matching the self-similar outer and wall regions with the overlap layer. Source dependence has been studied for true wall jets but is not defined for the wall jets resulting from impinging jets.

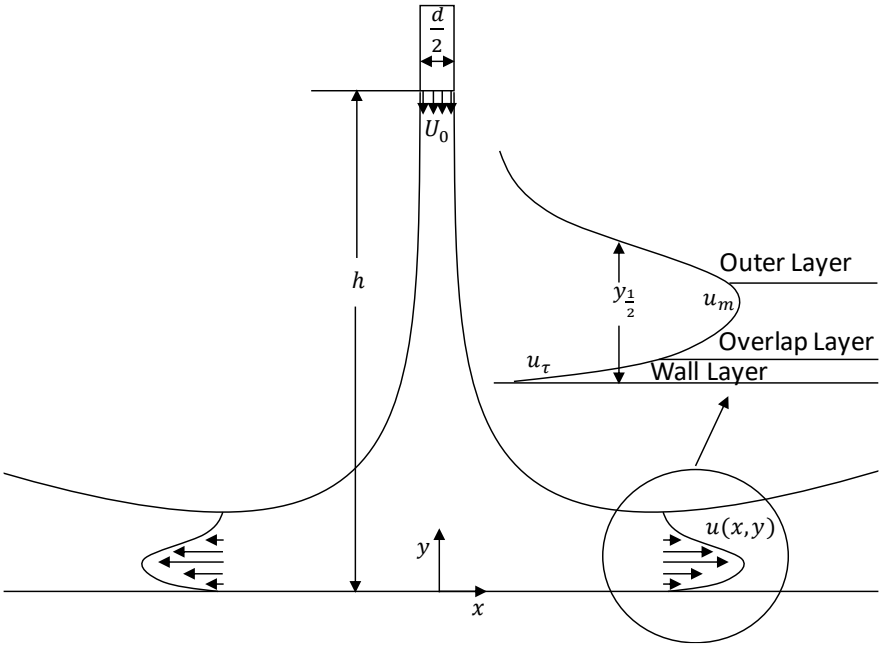

Figure 3.1 Schematic of an impinging jet and the resulting wall jet. h - standoff height, d - jet hydraulic diameter, which is equal to twice the jet width for 2D planar jets, $y_{1/2}$ - location of half maximum velocity, u_m - maximum wall jet velocity, and u_τ - wall jet friction velocity.

The equation of motion for the wall jet is defined as:

$$u\frac{\partial u}{\partial x}+v\frac{\partial u}{\partial y}=\frac{\partial}{\partial y}\left[v\frac{\partial U}{\partial y}-\frac{\tau}{\rho}\right] \tag{3.1}$$

$$u\to 0\ as\ y\to\infty;\ \ u=v=0\ at\ y=0.$$

As first proposed by Glauert [36], the equations of motion are assumed to be solved by outer and inner self-similar equations. The outer region becomes:

$$u=u_m(x)f_o'(\eta) \tag{3.2}$$

$$\eta=\frac{y}{y_{1/2}(x)}.$$

George et al. [37] demonstrated that the classical "law of the wall" coordinates for turbulent boundary layers can be used for turbulent wall jets:

$$u=u_\tau(x)f_i(y^+) \tag{3.3}$$

$$y^+=\frac{yu_\tau(x)}{\nu}.$$

The properties of inner and outer regions need to be merged in what has traditionally been called the overlap region. George et al. [37] concluded that the overlap velocity profile could be accurately described in both inner and outer similarity coordinates, but Gertsen [38] demonstrated that the velocity in this overlap region could be more accurately described in the form of a defect law:

$$u=u_m(x)-u_\tau(x)f'(\eta_m) \tag{3.4}$$

$$\eta_m=\frac{y}{y_m(x)}.$$

The solutions to these similarity equations have been determined separately by George [37] and Gertsen [38]. In this work, we examine the x-dependent variables, which can be used to describe the rest of the flow field when determined. Thus, we are interested in developing relations for

$y_{1/2}$, y_m, u_m, and u_τ. For each of these variables, we will assume a power-law relation in x [39] with source dependent coefficients:

$$y_{1/2} \sim \beta_1 x^{\alpha_1}, \quad y_m \sim \beta_2 x^{\alpha_2}, \quad u_m \sim y_{1/2}^{\alpha_3}, \quad u_\tau \sim \beta_4 x^{\alpha_4}.$$

To determine the power-law exponents, one must determine proper scaling through dimensional analysis. In the description of the planar impinging jet, we consider seven parameters: $x \sim L$, the streamwise distance from the impingement point; $y \sim L$, the distance from the impingement surface; $h \sim L$, the standoff height of the jet; $d \sim L$, the jet hydraulic diameter; $\rho \sim ML^{-3}$, the fluid density; $\nu \sim L^2T^{-1}$, the kinematic viscosity; and $U_0 \sim L^1T^{-1}$, the velocity at the jet exit. L, M, and T are the units of length, mass, and time, respectively. Using these variables for dimensional analysis yields the following non-dimensional groups:

$$\Pi_1 = \frac{h}{d}, \Pi_2 = \frac{x}{h}, \Pi_3 = \frac{y}{h}, \Pi_4 = \frac{U_0 d}{\nu}.$$

Narashima et al. [40] demonstrated that scaling x and y by the momentum flux of the source is effective when writing power-laws for the velocity in wall jets, while George et al. [37] defines the momentum flux per unit mass, $M_o = U_0^2 d/2$. In the study of underexpanded jets, one must consider the changes in density by defining the momentum flux as $J = \rho_0 U_0^2 d/2$. This normalization yields the following non-dimensional versions of x, y, u_τ, and u_m:

$$X = \frac{Jx}{\rho_\infty \mu_\infty}, \qquad Y_{1/2} = \frac{Jy_{1/2}}{\rho_\infty \mu_\infty}, \qquad Y_m = \frac{Jy_m}{\rho_\infty \mu_\infty}, \qquad U_\tau = \frac{u_\tau \mu_\infty}{J}, \qquad U_m = \frac{u_m \mu_\infty}{J}.$$

It is important to note that this procedure does not account for all of the source dependence. To account for the incomplete self-similarity of wall jets, one must consider a Reynolds number associated with the jet width. To capture the physics of underexpanded jets, the nozzle pressure ratio (NPR) and standoff height to jet hydraulic diameter ratio considered:

$$Re_n = \frac{U_0 d}{\nu_\infty}, \qquad NPR = \frac{P_0}{P_\infty}.$$

Wygnanski et al. [41] established that $Y_{1/2}$, Y_m, U_τ, and U_m can be expressed as power-laws of the form:

$$Y_{1/2} = \beta_1 X^{\alpha_1} \tag{3.5}$$

$$Y_m = \beta_2 X^{\alpha_2} \tag{3.6}$$

$$U_m = \beta_3 Y_{1/2}^{\alpha_3} \tag{3.7}$$

$$U_\tau = \beta_4 X^{\alpha_4}. \tag{3.8}$$

For the case of underexpanded impinging jets, we can assume each beta term is a function of the nozzle parameters Re_n, h/d, and NPR of the form $\beta = Re_n^a (h/d)^b NPR^c$. The alpha terms are assumed to be universal across all cases. By assuming solutions for the wall jet variables of this form, we can determine the exponents in the coefficients and the power-law exponents simply by linear least squares regression on the natural logarithm of equations 5-8, i.e.: $\ln(Y_{1/2}) = a\ln(Re_n) + b\ln(h/d) + c\ln(NPR) + \alpha_1 \ln(X)$.

While underexpanded impinging jets provide high wall shear stress, which is desirable for aerodynamic particle resuspension, flow in the wall jet region is compressible and has the potential to introduce complications in similarity formulations. The effects of density fluctuations on turbulence have been shown by Morkovin [42] to be negligible for compressible jets for $Ma < 1.5$. The range of cases in this work is limited to subsonic wall jets ($Ma < 0.8$), so the turbulent properties are not likely to be affected by compressibility. However, mean density effects may still be important. Ahlman et al. [43] found, through a direct numerical simulation (DNS) study, that mean density effects were only significant in the wall-normal direction by comparing Reynolds and

Favre averaged velocity profiles for the outer layer and comparing traditional wall coordinates with semi-local [44] and Van Driest [45] scaling. When examining velocity profiles, it was also found that mean density effects were minimal. Plotting profiles in Van Driest and semi-local scaling did not yield a noticeable improvement in similarity analysis, as shown in SI figures 1-3. For this reason, the effects of compressibility on wall jet similarity are not considered for the range of Mach numbers presented in this work. It is likely that this assumption is not valid for transonic and supersonic wall jets.

3.3 COMPUTATIONAL STUDY

3.3.1 *Computational Method*

The scientific literature does not report the experimental data or results from DNS related to the wall jet developed from compressible impinging jets in the literature. To compute the flow properties needed for estimation of shear stresses, we use steady-state CFD simulation. While Shukla and Dewan [46] found that LES and DES can be accurate in predicting flow profiles, these methods are computationally intensive for a broad parametric study. Numerical simulations for this work were performed using ANSYS FLUENT 17.2 software and a $k-\omega$ shear stress transport closure model. A pressure-based coupled solver is used with the QUICK (Quadratic Upstream Interpolation for Convective Kinematics) discretization scheme [47] to solve the steady-state Favre-Averaged Navier-Stokes equations:

$$\frac{\partial(\bar{\rho}\widetilde{u_i})}{\partial x_i} = 0 \tag{3.9}$$

$$\frac{\partial\left(\bar{\rho}\widetilde{u_i}\widetilde{u_j}\right)}{\partial x_i} = -\frac{\partial \bar{p}}{\partial x_i} + \frac{\partial \overline{\tau_{ij}}}{\partial x_j} - \frac{\partial\left(\overline{\rho u_i'' u_j''}\right)}{\partial x_j} \tag{3.10}$$

$$\frac{\partial}{\partial x_j}\left(\bar{\rho}\widetilde{u_j}\left(\tilde{h}+\frac{1}{2}\widetilde{u_i}\widetilde{u_j}\right)+\widetilde{u_j}\rho u_i''u_j''\right) = \frac{\partial}{\partial x_j}\left(\widetilde{u_i}\left(\overline{\tau_{ij}}-\overline{\rho u_i''u_j''}\right)-\bar{q}-\overline{\rho u_j''h''}+\overline{\tau_{ij}u_i''}-\frac{1}{2}\overline{\rho u_j''u_i''u_i''}\right). \quad (3.11)$$

Where, $\tilde{u}=\overline{\rho u}/\bar{\rho}$ and $u''=u-\tilde{u}$. τ_{ij} represents the viscous stress tensor.

While turbulence closure models are known to be have specific weaknesses, especially when modeling impinging jets, Jaramillo et al. [48] demonstrated that $k-\omega$ models can accurately calculate the mean flow of planar impinging jets when compared to DNS. The $k-\omega$ shear stress transport (SST) model this work uses, solves the $k-\epsilon$ closure equations away from the wall in the free stream and free jet portions of the flow, while using $k-\omega$ near the wall to resolve the boundary layer. As demonstrated by Alvi et al. [49] and discussed by Fillingham et al. [7], the $k-\omega$ SST model [50] is a good choice for modeling underexpanded impinging jets while resolving the wall jet boundary layer. Shukla and Dewan. [51] also found $k-\omega$ SST to be superior to other closure models when considering planar impinging jets.

Figure 3.2 shows the computational domain. The inlet boundary condition is defined as the exit of an isentropic nozzle where the flow is choked; thus, the boundary can be described by a total pressure and a static pressure where the total pressure is necessarily (for an ideal diatomic gas) 1.893 times the static pressure. The walls are modeled as isothermal, no-slip boundaries. The outlets are defined as atmospheric pressure outlets. The outlets are located at 50 jet hydraulic

diameters (100 jet slot widths) from the jet axis corresponding to a minimum of 1.5 times the impingement height.

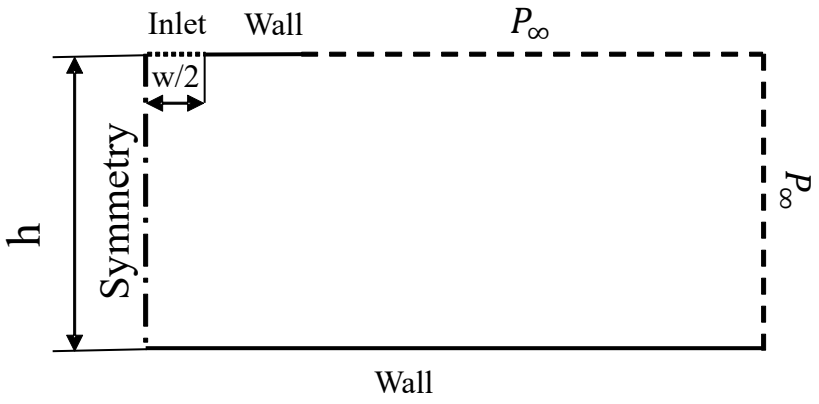

Figure 3.2. Schematic of CFD domain and boundary conditions. Note that $d = 2w$ for an infinite planar jet, where d is the hydraulic diameter.

The computational grid contains ~600,000 quadrilateral elements. At the impingement surface, the first node is at a constant distance from the wall and is placed within a y^+ value of 1 at the maximum shear stress location, ensuring that the viscous sublayer is resolved for the entirety of the domain. The x-direction spacing is set to avoid the elements with an aspect ratio greater than 50:1. Mesh independence was confirmed by doubling the number of elements; further mesh refinement did not affect the results. Table 3.1 shows the conditions used in the study. The range is chosen based on the wall shear stress required for microparticle resuspension [52,53]. All cases result in a subsonic wall jet. For a supersonic wall jet, a separate characterization would be necessary; this is beyond the scope of the paper.

Table 3.1. Summary of CFD Cases.

h/d	*d (mm)*	*NPR*
15, 17.5, 25, 30	1, 2	1.2, 1.6, 2.0, 2.4, 2.8

3.3.2 *Computational Model Validation*

To evaluate the 2D assumption, a 3D simulation of the jet with an aspect ratio of 30 to 1 was performed. As with the 2D simulation, the QUICK discretization scheme and $k-\omega$ SST turbulence closure model were used. The 3D domain includes ~12 million elements with the first node in the wall-normal direction at $y^+ = 1$. Figure 3.3 shows that the centerline profile of wall shear stress from the 3D simulation agrees well with the 2D simulations.

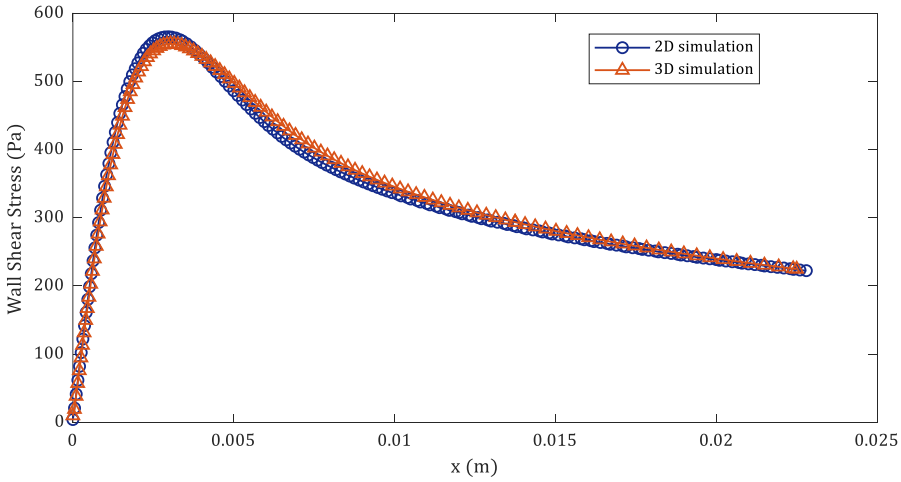

Figure 3.3. Comparison of wall shear stress as a function of distance from impingement location for 2D and 3D simulations: h = 30 mm, d = 1 mm, and NPR = 2.0 from the 2D simulation and centerline profile from the 3D simulation.

Validation of the CFD result is challenging in the absence of the experimental or DNS data for compressible planar impinging jets needed for direct comparison. To validate the model, we evaluated two flow regions: (i) impinging jet and (ii) wall jet region. Related to the impinging jet region, the implementation of the $k-\omega$ SST jet was previously validated in the study of underexpanded axisymmetric jets. The shape and the shock structures of the impinging jet predicted by the $k-\omega$ SST model were shown to be in excellent agreement with experimental observations from Schlieren photography [7]. This provides confidence in the modeling accuracy of the supersonic region of the jet. Additionally, in this study, the CFD predictions were compared

with normal pressure profiles on the impingement surface from pressure-sensitive paint (PSP) experiments. PSP utilizes the emission spectra of a luminophore by relating the emission intensity at specific wavelengths to the partial pressure of oxygen at the surface. Images were taken at wind-on and wind-off conditions, and the intensity ratio of the images relate to pressure. Binary FIB PSP and a PSP-CCD camera from Innovative Scientific Solutions Incorporated were used. The calibration curve measurements for the PSP were provided by ISSI, as well. Evaluation of the numerical model was performed using oblique planar jet impingement against the PSP measurements. Oblique impingement results in an uphill shift in the impingement point from the geometric center [54]. Figure 3.4 shows the CFD pressure profiles overlayed on the PSP measurements. The CFD simulations show agreement in shape and magnitude with PSP measurements of the pressure profile, allowing for confidence in the accuracy of the CFD in the impingement region.

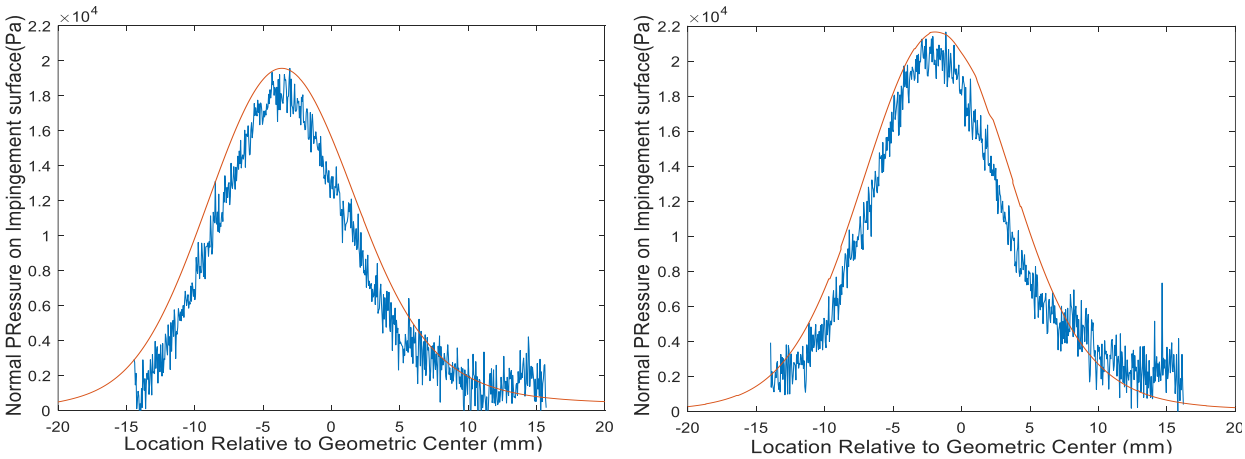

Figure 3.4. Normal pressure profiles from CFD (red) and pressure-sensitive paint (blue) experiments for h = 30 mm, d = 1 mm, NPR = 1.0 with the impingement angle of 30 degrees (left) and 15 degrees (right).

To evaluate the model accuracy in the wall jet region, the $k-\omega$ SST model results are compared to two separate DNS studies. First, the model was used to replicate DNS data from planar impinging jet conducted by Jaramillo et al. [48] The authors report a wall jet velocity profiles

at the locations downstream of the impingement point, up to 8 jet widths. Figure 3.5 (a) shows the velocity profile from DNS by Jaramillo et al. [48] and $k-\omega$ SST are in good agreement. This agreement is closer for locations away from the impingement point, which is of the most interest in our study. Second, the model was evaluated against the DNS of a classical wall jet conducted by Naqavi et al. [55] The boundary conditions were matched to ensure the wall jet development was modeled accurately. Figure 3.5 (b-d) compares the development of the wall jet thickness, $y_{1/2}$, the maximum velocity, U_m, and the wall shear stress, τ. The 2D $k-\omega$ SST model shows excellent agreement with both planar impinging jet [48] and wall jet DNS [55] studies. In summary, the $k-\omega$ SST was found to be an acceptable model for use in the parametric study of planar impinging jet due to its good agreement with the PSP measurements, Schlieren photography, as well as two DNS studies describing wall jet development.

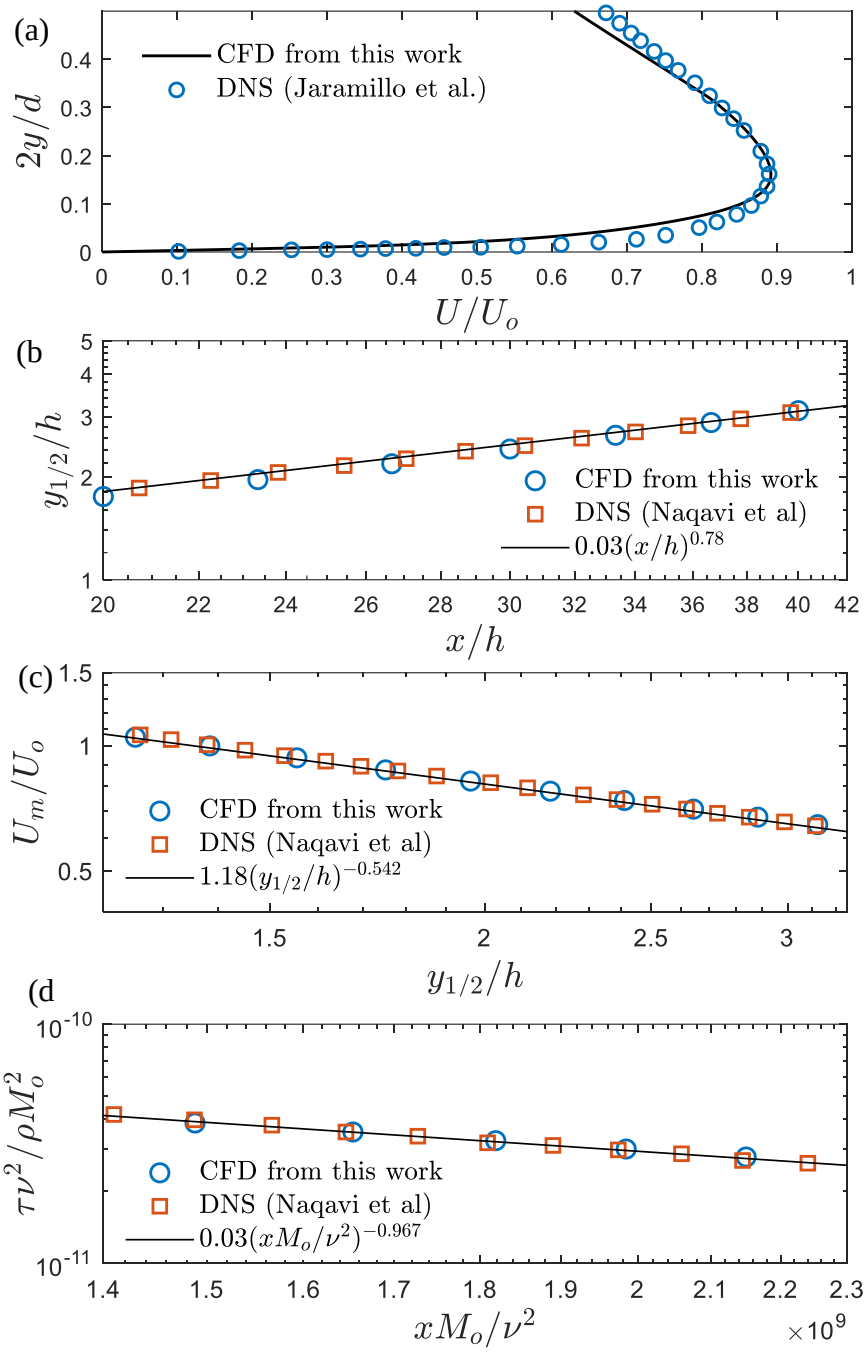

Figure 3.5. Validation of $k-\omega$ SST for impinging jet modeling (a) Comparison of the velocity profile at 8 jet widths downstream of impingement location against DNS from Jaramillo et al. [48]. Comparison with wall jet DNS simulation from Naqavi et al. [55] (b) Decay of half maximum velocity location. (c) maximum velocity (d), and wall shear stress.

3.4 RESULTS

3.4.1 *Wall Jet Velocity Profiles*

Velocity profiles from the 2D impinging jet simulations are examined to determine the self-similarity of the wall jet region. Traditionally, the planar wall jet has been considered self-similar in coordinates presented in Eq. 2. Wygnanski et al. [41] observed that normalization by $y_{1/2}$ and u_m appears to yield similarity for the entire velocity profile; however, it was later demonstrated [37] that normalization by $y_{1/2}$ and u_m only yields similarity in the outer region (y > $y_{1/2}$) of the jet. The velocity profile for the outer region is identical to that of a free jet and thus can be described by:

$$f_o' = 1 - (\tanh k\eta)^2 \tag{3.12}$$

$$k = \operatorname{atanh} \sqrt{\frac{1}{2}}.$$

Figure 3.6 illustrates the self-similarity in the outer region for three different geometries and NPRs, comparing the CFD simulations to the analytical solution in Eq. 12. The self-similarity develops downstream of the impingement point for $x/h > 0.2$.

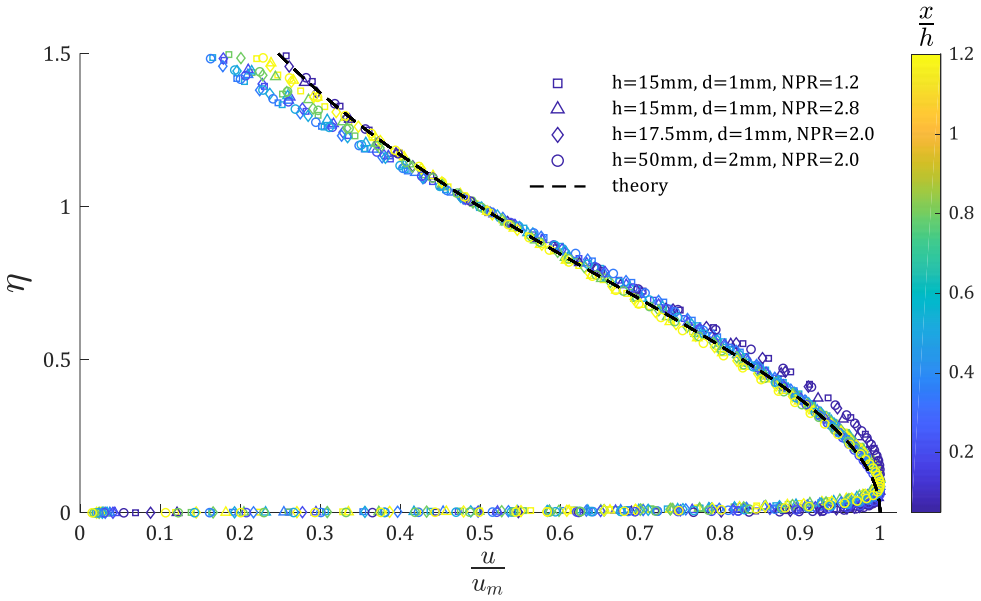

Figure 3.6. Velocity profiles plotted in outer coordinates for four different cases vs. the theoretical profile (Eq. 12). Patterns demonstrate similarity independent of the geometry and nozzle pressure ratio.

To examine similarity in the overlap layer, the coordinates described by Eq. 4 are used in a defect relation given by Eq. 13. Gertsen [38] developed an analytical expression for the velocity profile:

$$f' = \frac{1}{0.41}\left(-\ln \eta_m - \frac{5}{6} + \frac{3}{2}\eta_m^2 - \frac{2}{3}\eta_m^3\right). \tag{3.13}$$

In Figure 3.7, velocity profiles are plotted in defect coordinates for two geometries and two NPRs; the simulations are also compared with the analytical expression, Eq. 13. The overlap layer similarity takes longer to develop ($x/h > 0.4$) than the inner and outer layers.

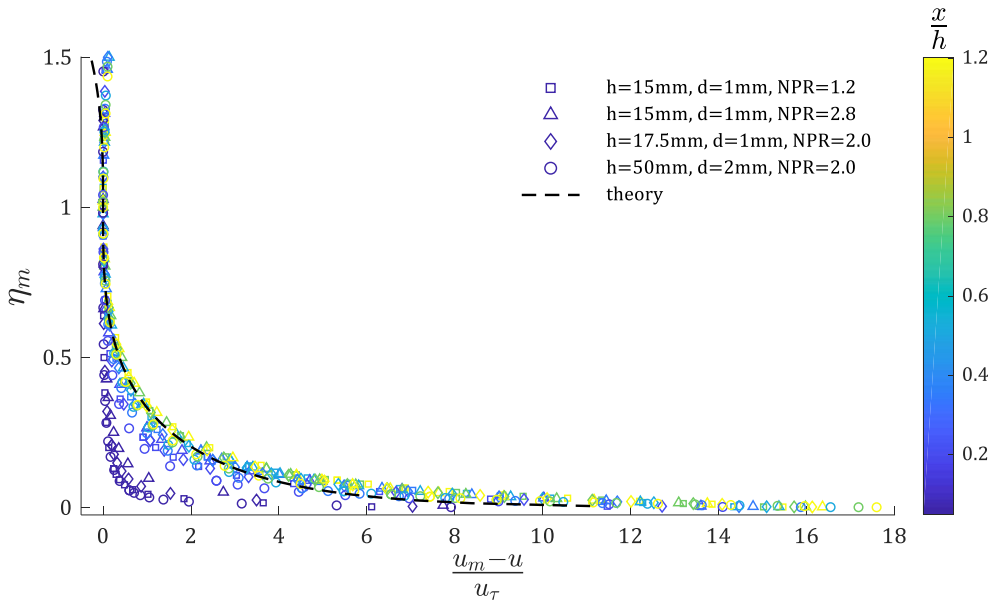

Figure 3.7. Velocity profiles plotted in defect coordinates for four different cases vs. the theoretical profile (Eq.13). Profiles demonstrate similarity independent of the geometry and nozzle pressure ratio.

When examining the velocity profile in defect coordinates, it appears that similarity extends to the wall layer; however, the analytical expression for the velocity profile derived from the equations of motion does not apply for $y^+ < 30$. To obtain similarity in the viscous wall layer, the velocity

profiles are plotted in the traditional "law of the wall" coordinates. Figure 3.8 plots the wall layer for the same cases as Figures 6 and 7.

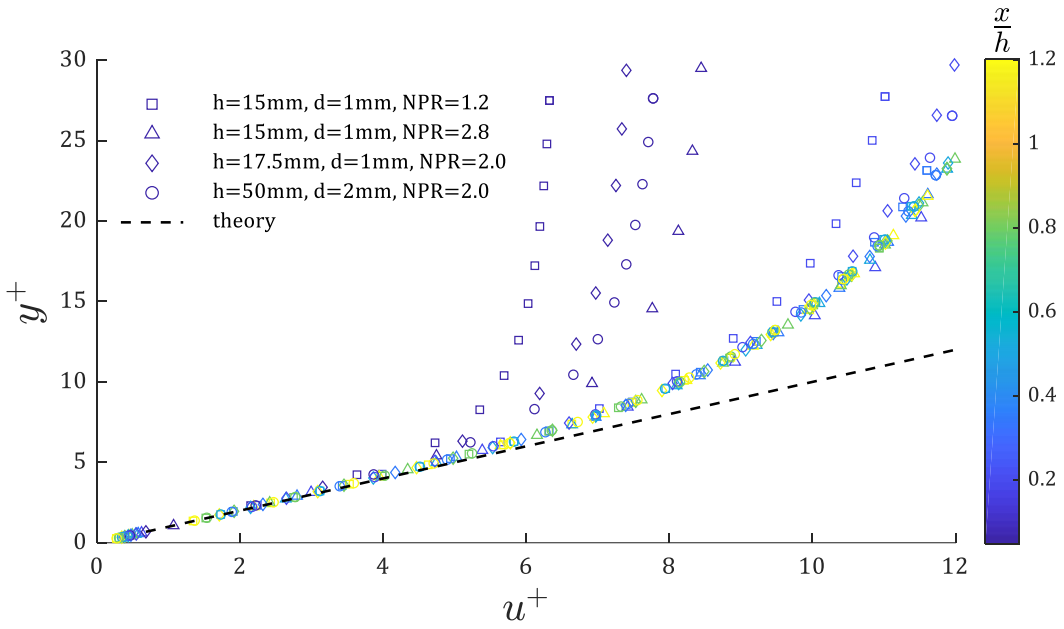

Figure 3.8. Velocity profiles plotted in wall coordinates for four different cases. The $y^+ = u^+$ shown as the dash line. Profiles demonstrate similarity independent of the geometry and nozzle pressure ratio.

Figure 3.8 demonstrates that the inner layer of the wall jet follows the traditional law of the wall, with a linear velocity profile in the viscous sublayer up to a y^+ value of 5. This is important when considering particle removal as the linear velocity profile allows for the calculation of drag forces of particles in the sublayer with only knowledge of the wall shear stress. Figures 3.7 and .8 show that an analytical expression that characterizes the "buffer" region (between the linear and log law regions of the boundary layer) of the velocity profiles of the turbulent boundary layers does not exist. Plotting data in the established similarity coordinates shows that impinging jets produce wall jets in the same triple-layer structure demonstrated experimentally [56].

3.4.2 *Power Law Relationships*

After confirming the similarity of the wall jet velocity profile, the similarity variables from each computational case were calculated and then analyzed to obtain the source-dependent power-law relationship as a function of *x*-coordinate for each similarity variables. Before calculating the power-laws, it is important to note that while the far-field conditions are not typically considered in the wall jet analysis, they are significant when determining the power-law exponents. As Gertsen [38] pointed out, his analysis is only valid in the absence of a perpendicular wall coincident with the source of the wall jet. The analysis of George et al. [37] considers the wall jet to be emerging from a perpendicular wall, and thus discrepancies between their power-law exponents are expected. An impinging jet should behave similarly to that of a wall jet emerging from a perpendicular wall. The available experimental and computational studies [57,58] that consider a wall jet emerging from a wall have all been conducted in closed water tanks, meaning they represent a confined jet scenario for both the top and side boundary conditions. In this study, unconfined jets are investigated; thus, we expect some variation in the power-law relationships developed in this work.

The characteristic length of wall jet velocity profiles has been debated in the scientific literature [36-38]. Generally, the distance from the wall in the outer region, where the velocity is half of the maximum ($y_{1/2}$), is used as the length scale. Though it was suggested that this choice is arbitrary, the use of $y_{1/2}$ has repeatedly [40,41,58] shown to be useful in characterizing the similarity of wall jet velocity profiles. It was also demonstrated that momentum normalized $y_{1/2}$ can be accurately described by a source dependent power-law in the x-direction with a virtual origin. Figure 3.9 plots $Y_{1/2}$ against X for all geometries with 1 mm jet hydraulic diameter and all NPRs. Simulations show that a virtual origin is necessary for similarity, which is consistent with the

previous reports [37,41]. While there is not an obvious physical choice for the virtual origin of a traditional wall jet, the standoff height is a logical choice for impinging jets. Here, we define the virtual origin location as $X_0 = \frac{-Jh}{\rho_\infty \mu_\infty}$.

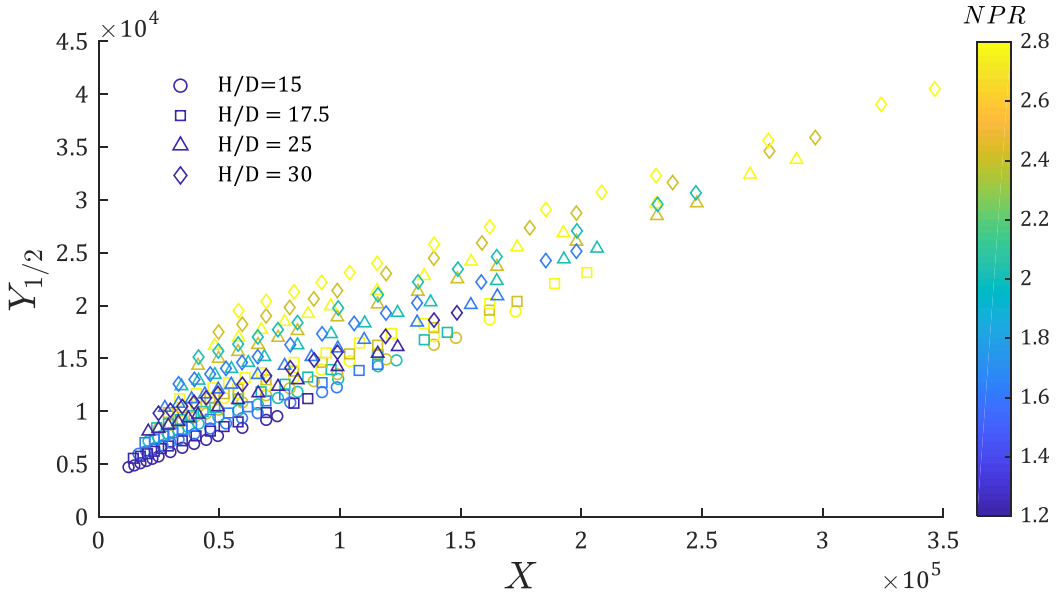

Figure 3.9. Momentum normalized half velocity wall distance plotted against momentum-normalized x-location for all height-to-diameter ratios colored by the nozzle pressure ratio.

Figure 3.10 (a) demonstrates the effectiveness of using standoff height as a virtual origin. The similarity is nearly obtained; however, an adjustment for source dependence based on nozzle pressure ratio improves the fit; $\beta_1 \sim NPR^{0.15}$ yields a linear relation, as shown in Figure 3.11 (b).

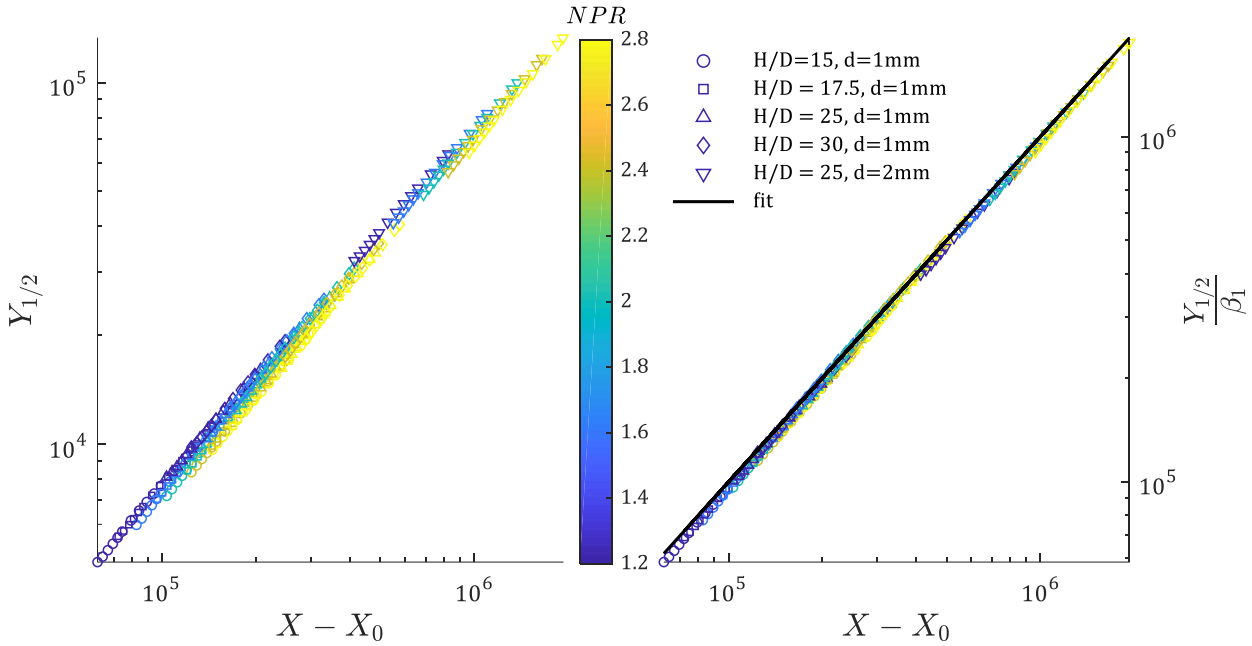

Figure 3.10. Momentum normalized $Y_{1/2}$ plotted against the momentum-normalized x-location with a virtual origin at the jet nozzle location and analytical solution to Eq. 14: (a) without nozzle pressure source dependence adjustment; (b) with nozzle pressure source dependent adjustment.

George et al. [37] proposed that the dependence of $y_{1/2}$ on x is necessarily non-linear but approaches linearity in the limit of $Re \to \infty$; for the experimental case examined $\alpha_1 = 0.97$. Gertsen [38] suggested that a linear relationship should be expected, but this determination is dependent on the absence of a wall perpendicular to the wall jet source. Naqavi [55] found that for the case of co-flow the best fit was for $\alpha_1 = 0.72$; however, the maximum x-coordinate in the analysis was limited to forty jet widths, and the wall jet was not fully developed. Since the virtual origin was not considered, and the fit is weighted to the thinner boundary layer, the exponent is significantly different from the analytical expressions for fully developed flow [37], [38]. In our analysis the wall jet is not constrained thus fully developed flow can be achieved; the least-squares analysis in this yielded $\alpha_1 = 0.98$.

$$Y_{1/2} = \beta_1 (X - X_0)^{0.98} \tag{3.14}$$

$$\beta_1 = 0.083 * NPR^{0.15}$$

In characterizing maximum velocity in the wall jet, a power-law based on a local length scale can be more accurate than one based on the global x-coordinate [37]. Intuitively, $y_m(x)$ can be used as the length scale for characterizing u_m. However, $y_{1/2}(x)$ has shown to have better a correlation; it is also easier to measure experimentally [58] and with DNS [55]. George et al. [37] proposed that the decay exponent for u_m as a function of $y_{1/2}$ is universal for wall jets. Figure 3.11 plots momentum normalized maximum velocity against $y_{1/2}$ with and without pressure source adjustment. Our calculations show that the NPR is the only source adjustment needed to obtain similarity in the wall jet, which is consistent with the findings that a power-law for maximum velocity based on the local length scale is universal [37].

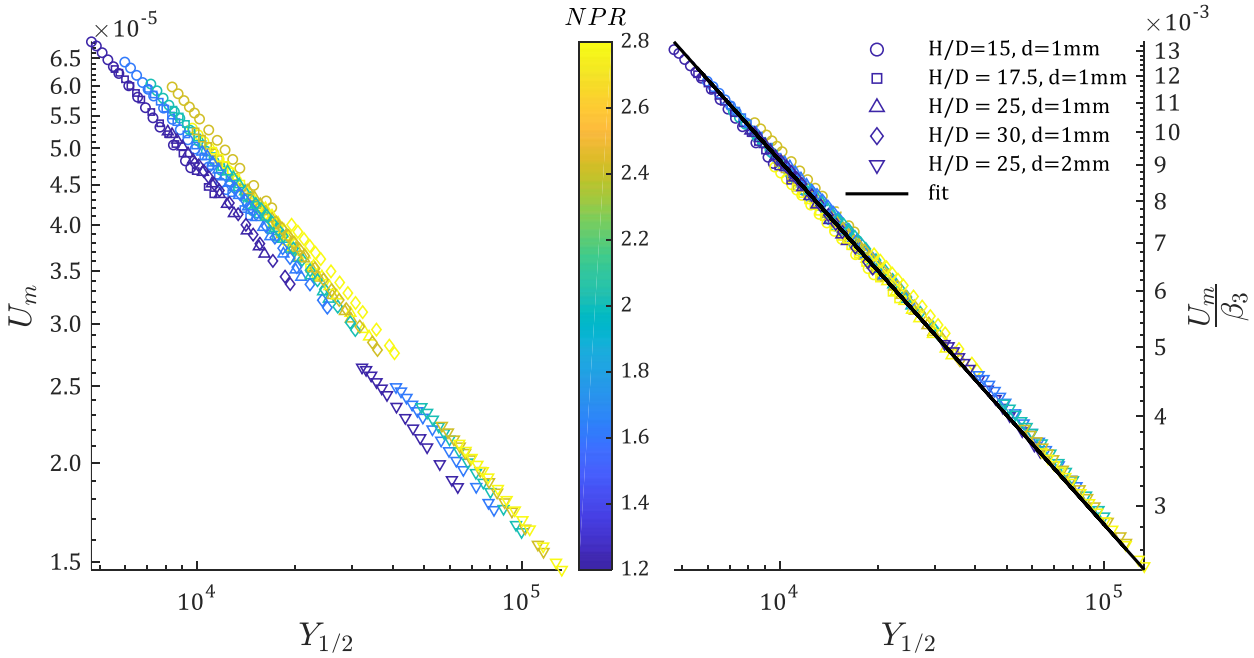

Figure 3.11. Momentum normalized maximum velocity plotted against momentum-normalized half-maximum velocity location: (a) without nozzle pressure source dependence adjustment; (b) with nozzle pressure source dependent adjustment and fit (Eq. 15).

After adjusting for nozzle pressure ratio, the power-law for maximum velocity relation is:

$$U_m = \beta_3 {Y_{1/2}}^{-0.52} \tag{3.15}$$

$$\beta_3 = 0.0051 * NPR^{0.15}.$$

The exponent for the decay of maximum velocity exponent $\alpha_3 = -0.52$, which is in good agreement with the analytical expression $\alpha_3 = 0.527$ [37]. The relationship between the local length scale and maximum velocity is one of the main characteristics of the traditional wall jets. The consistency with the literature provides evidence that wall jets developed from impinging jets exhibit the same length scale dependence as simple wall jets, regardless of far-field conditions.

To use defect law coordinates, the maximum velocity location, y_m as a function of x, must be characterized. The similarity of wall jets generally assumes the ratio, $\gamma = y_m/y_{1/2}$, to be constant, however, it is only strictly true as $x \to \infty$ [37,38]. For impinging jets near the impingement point, this approach is not valid, thus a separate power-law for y_m is required. Figure 3.12 (a) plots momentum normalized maximum velocity location against the momentum-normalized x, showing that a virtual origin is not necessary. The source dependence, as determined by a least-squares fit, is plotted in Figure 3.12 (b). The final expression for y_m is:

$$Y_m = \beta_2 X^{0.49} \tag{3.16}$$

$$\beta_2 = 0.00027 * NPR^{0.33} * \frac{h}{d}^{0.48} * Re_n^{0.85}.$$

The exponent for Y_m in this work, $\alpha_2 = 0.49$, is lower than reported in the literature. Tang et al. [59] found $\alpha_2 = 0.717$ using LDA while Naqavi et al. [55] found $\alpha_2 = 0.743$ based on the DNS calculations. Tang et al. [59] conducted their experiments in an enclosed water tank while Naqavi et al. [55] used a coflow for the DNS. These far-field conditions significantly change the entrainment pattern. The jet would primarily entrain momentum from co-flow or large-scale structures moving

in the x-direction, however, in the case of the perpendicular wall or impinging jet, the momentum must be entrained from the y-direction. This major difference in the entrainment pattern changes the wall development; the y-direction momentum entrainment hinders the wall jet spreading, thus reducing the location of the maximum velocity. To confirm this assumption, maximum velocity location data were taken from the velocity profiles provided by Shukla and Dewan [46]. These data were fitted with a power-law with the same exponent as found in this work with the excellent agreement.

Fluid compressibility did not have an appreciable effect on the decay analysis. Fitted cases for only $Ma{\sim}0.3$ and $Ma{\sim}0.8$ had exponents of $\alpha_3 = -0.50$ and $\alpha_3 = -0.48$, respectively, which is a small difference compared to the exponent found through DNS simulations of a wall jet reported in the literature [55].

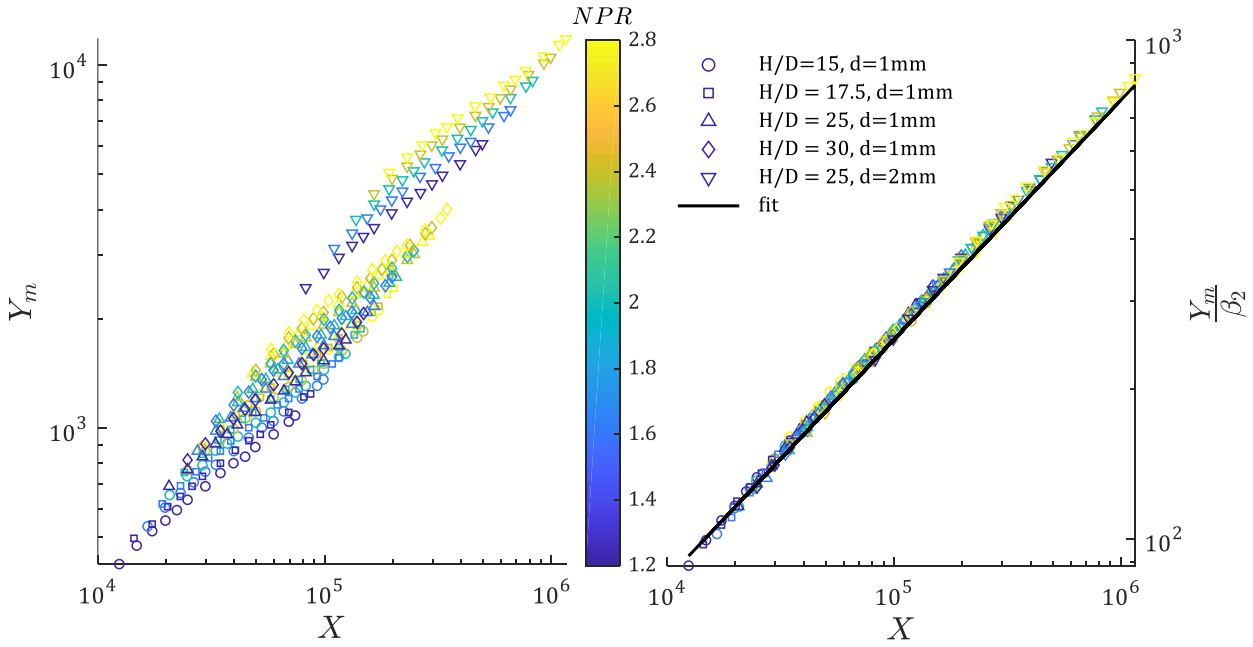

Figure 3.12. Momentum normalized maximum velocity wall-distance plotted against momentum normalized x-location: (a) without nozzle pressure source dependence adjustment; (b) with nozzle pressure source dependent adjustment and fit (Eq. 16).

Friction laws are generally expressed as a friction coefficient, which is a function of a local Reynolds number. For this work, the friction coefficient power-law works for $x/h > 1.0$. Using the downstream data, a friction law has the best fit:

$$c_f = \left(\frac{u_\tau}{u_m}\right)^2 = 0.0029 Re_l^{-0.19} \tag{3.17}$$

$$Re_l = \frac{u_m y_{1/2}}{\nu_{0.5}}.$$

This formulation agrees with the existing literature [37,58,60]. Friction laws in this form are inconsistent across experimental and DNS data, however, and are highly dependent on the momentum source; thus, for this work, friction velocity was characterized directly, similar to the maximum wall jet velocity. Figure 3.13 demonstrates the effect of the source term adjustment. Momentum normalized friction velocity can be expressed as:

$$U_\tau = \beta_4 X^{-0.3} \tag{3.18}$$

$$\beta_4 = 0.021 * \frac{h}{d}^{0.22} * NPR^{-0.07} * Re_n^{-0.5}.$$

Note that it is difficult to obtain physical interpretations from the source dependent exponents, as there are insufficient analytical or experimental data of planar impinging jets. Further investigation is needed to gain insight into the source-dependent exponents.

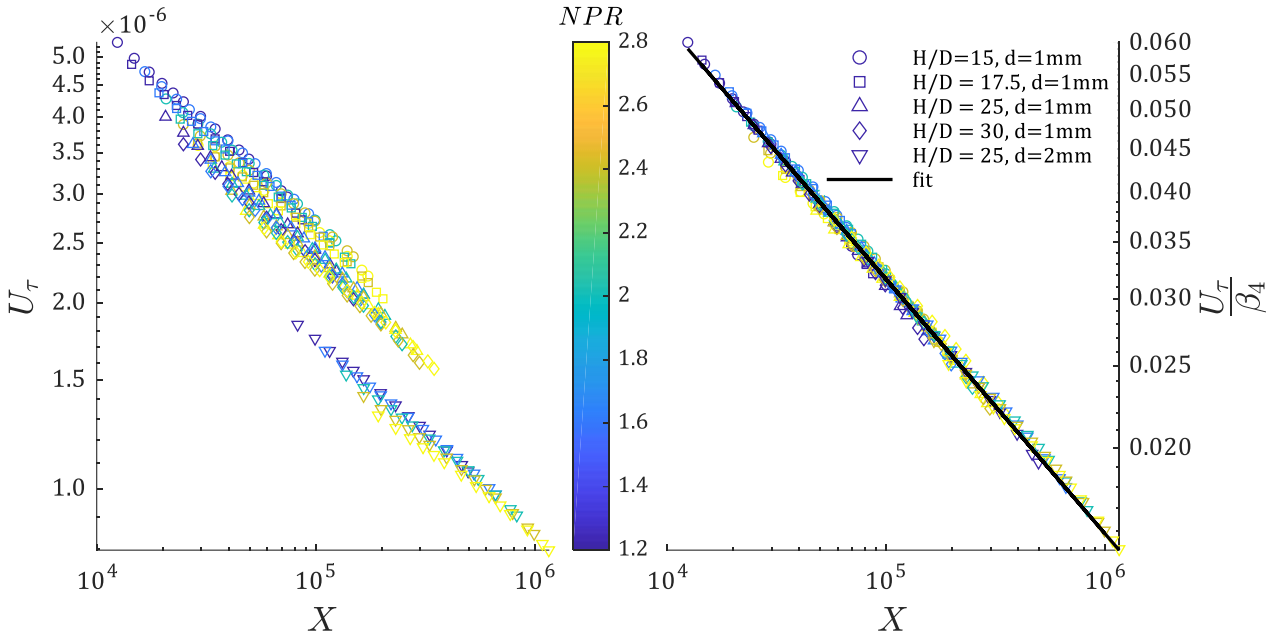

Figure 3.13. Momentum normalized friction velocity plotted against momentum-normalized x-location: (a) without nozzle pressure source dependence adjustment; (b) with nozzle pressure source dependent adjustment and fit (Eq.18).

3.4.3 *Wall Shear Stress*

Though the fluid compressibility does not have a significant effect on the power-laws or similarity, the change in mean density is not negligible. For this reason, the wall shear stress cannot be characterized directly from friction velocity. Here, we formulate a power-law for momentum normalized wall shear stress, τ^*:

$$\tau^* = \frac{\tau}{\rho_\infty}\left(\frac{\mu_\infty}{J}\right)^2.$$

Figure 3.14 plots momentum normalized wall shear stress against momentum-normalized x with and without source dependence, demonstrating that a power-law is appropriate for wall shear stress.

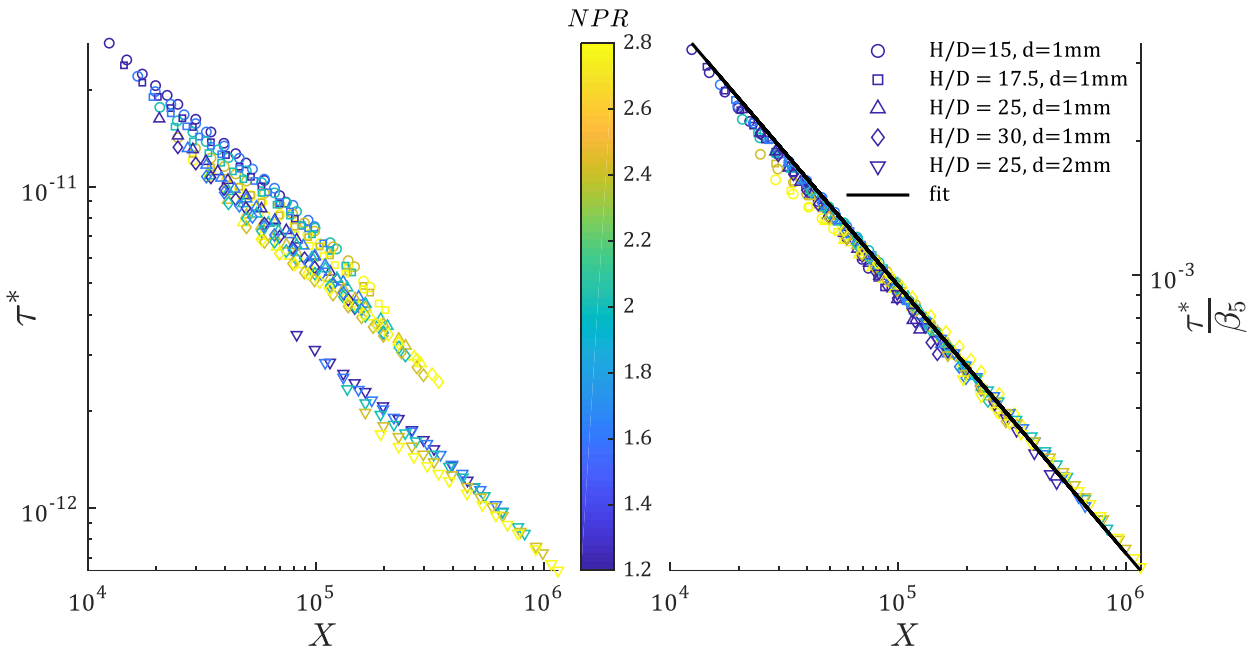

Figure 3.14. Momentum normalized wall shear stress plotted against momentum-normalized x-location: (a) without nozzle pressure source dependence adjustment; (b) with nozzle pressure source dependent adjustment and fit (Eq. 14).

The source dependent power-law developed for momentum normalized wall shear stress is:

$$\tau^* = \beta_5 X^{-0.61} \tag{3.19}$$

$$\beta_5 = 0.00059 * \frac{h}{d}^{-0.45} * NPR^{-0.18} * Re_n^{-1.0}.$$

The power-law developed in this work suggests a slower decay of wall shear stress (α = 0.61) than those in the literature for traditional wall jets. Wygnanski et al. [41] found the decay exponent to be -1.07, while Naqavi et al. [55] found an exponent of -0.967 via DNS. As stated before, both of these studies are conducted without a wall coincident and perpendicular to the wall jet source. For a direct comparison to impinging jets, the shear stress data from Tu and Wood [33] for an impinging jet with $h/d = 20.6$ and $Re_n = 6300$ is more appropriate. The experimental data was fitted with a power-law, the exponent based on the experimental data fits the data well, as shown in Figure 3.15.

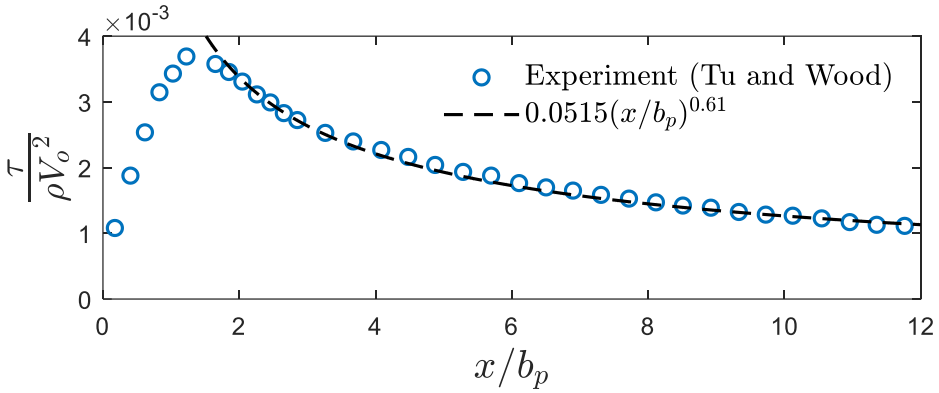

Figure 3.15. Wall shear stress profile from Tu and Wood with height to jet width ratio of 20.6 and Re=6300 with power-law fit, b_p is the half-width of the normal pressure profile.

3.4.4 *Summary of Wall Jet Relations*

The developed power-laws suggest that the power-law exponents are source independent and universal while their coefficients (pre-exponential factors) depend on the jet nozzle parameters. These relations allow for mapping of the wall jet velocity profile and wall shear stress based on knowledge of nozzle parameters and x location on the impingement surface. Table II summarizes the power laws below.

Table 3.2. Summary of Wall Jet Power-Laws from Planar Impinging Jet

Wall Jet Variable	*Power-Law*	*Coefficient, β*
$Y_{1/2}$	$\beta_1(X-X_0)^{0.98}$	$0.083 * NPR^{0.15}$
Y_m	$\beta_2 X^{0.49}$	$0.00027 * NPR^{0.33} * h/d^{0.48} * Re_n^{0.85}$
U_m	$\beta_3 {Y_{1/2}}^{-0.52}$	$0.0051 * NPR^{0.15}$
U_τ	$\beta_4 X^{-0.3}$	$0.021 * h/d^{0.22} * NPR^{-0.07} * Re_n^{-0.5}$
τ^*	$\beta_5 X^{-0.61}$	$0.00059 * h/d^{-0.45} * NPR^{-0.18} * Re_n^{-1.0}$

3.5 CONCLUSIONS FOR PLANAR UNDEREXPANDED JETS

A parametric study uses 2D numerical simulations to examine underexpanded impinging jets over a range of jet parameters, such as jet standoff distance, jet hydraulic diameter, and jet nozzle pressure ratio. The velocity fields calculated from CFD were transformed into similarity coordinates traditionally used for studying wall jets, demonstrating the self-similar nature of the wall jet resulting from underexpanded impinging jets. These similarity coordinates provide a framework to map the entire wall jet velocity field by developing power-law equations for the wall jet similarity variables based solely on the nozzle parameters and streamwise location. The analysis of the similarity profiles and power-laws led to the following conclusions:

- The wall jet developed from planar jet impingement has the same triple-layered structure as classical wall jets. Thus, the x-dependent length scales and velocities ($y_{1/2}, y_m, u_\tau$ and u_m) can be used to analyze wall jet properties.
- Compressibility does not significantly affect the similarity analysis; that is, density adjusted similarity coordinates do not yield improvement over traditional coordinates for wall jets with $Ma < 0.8$.
- The wall jet velocity profile from under expanded impinging jets can be mapped using power-laws for $y_{1/2}, y_m, u_\tau$ and u_m based only on the nozzle parameters. Jet geometry and operating conditions (h, d, NPR) have a significant effect on the power-law coefficients, while the power-law exponents are independent of these parameters. Normalization by momentum, as opposed to length scales, is found to be effective in reducing source dependence in the power-laws.
- The entrainment patterns have a significant effect on the power-law exponents but not the shape of the wall jet velocity profile.

- A power-law for normalized wall shear stress allows for estimating wall shear stress, within a maximum error of 8%, as a function of only jet hydraulic diameter, standoff height, NPR, and x-coordinate.

Chapter 4. CALCULATION OF ADHESION FORCE IN AERODYNAMIC PARTICLE RESUSPENSION

This work is published in the Journal of Aerosol Science[61].

Microparticle adhesion and resuspension are critical in studies of surface contamination, non-contact sampling, environmental and occupational health assessments, and surface cleaning. Direct adhesion measurement methods that evaluate the pull-out force are often limited to a range of operational conditions. The established analytical models need additional terms to account for roughness, morphology, and environmental conditions. The proposed aerodynamic method offers a non-contact evaluation of particle-surface adhesion force. In this work, aerodynamic detachment of silica microspheres in the 12-26 μm range from a smooth glass surface is studied experimentally. Computational fluid dynamics (CFD) calculates the drag and lift forces acting on the particles. The adhesion force is derived from the moment balance required to initiate the rolling motion of the particle. The aerodynamic forces acting on the particle, calculated by the CFD, agree with the theoretical values for a spherical particle in the shear flow in the Stokes regime (Re<1). The aerodynamic force calculations are extended to Re=1-1000. The aerodynamic method shows a monotonically increasing dependency of the adhesion force with particle diameter; the results are consistent with the theoretical models and the published experimental data. The approach can be extended to more complex systems, including the effects of roughness, particle morphology and aging, and a range of environmental conditions.

4.1 INTRODUCTION

Besides the application related to non-contact sampling of illicit trace material residues, [62-64] understanding microparticle adhesion is important in other fields. In the microelectronics industry, adherent contaminant particles on the scale of tens of nanometers in diameter can produce

fatal flaws in finished devices. Particulate matter resuspended from HVAC systems can cause adverse health effects [65] and sick building syndrome [66] in biological systems. A comprehensive understanding of aerodynamic particle resuspension from surfaces has not yet been developed due to the challenges in characterizing dependence on particle size, morphology, particle-surface interaction, humidity, turbulence level, and other parameters. To gain a better mechanistic understanding of aerodynamic particle detachment, we examine the forces acting on particles during aerodynamic resuspension.

The established methods for evaluating adhesion forces include atomic force microscopy (AFM), the centrifugal method, the electric field detachment method, the drop test procedure, and the vibration method. Most methods were developed to measure the forces acting perpendicular to the surface. However, several authors describe techniques that measure the forces required to remove particles based on the rolling and sliding mechanism. Heim [67] performed a direct measurement of the adhesion and rolling friction forces between individual silica microspheres of radius between 0.5 μm and 2 μm using AFM. There are several difficulties when the AFM is used to measure environmental samples with large particle sizes and high loading conditions. The AFM technique takes measurements one particle at a time, where, for complex adhesion scenarios, the large number set is required for reliable statistical data. These include complex particle and surface morphologies, the effect of humidity, and particle aging studies. The contact nature of the AFM measurements introduces uncertainty in the surface energy distribution of the particle-surface system in the presence of the AFM cantilever tip. Another challenge is a characterization of time-dependent particle – surface interaction as the particle ages on the surface. As the particle ages on the surface, the particle/surface interface morphology evolves due to the acting van der Waals (vdW) force, electrostatic forces, relative humidity, and possible chemical interaction. In addition

to a physical aging mechanism where the particle and surface conform to each other, increasing the contact surface area, a chemical reaction between the particle and surface may occur, resulting in interface changes. The particle or surface may also be modified by other compounds or natural processes, e.g., coating by semivolatile organics and chemical processes, such as oxidation, chemical decomposition, biological activity. The effect of these complex processes on the particle surface interaction requires the development of alternative methods.

Among the non-contact methods, centrifugal, vibrational, and hydrodynamic, and techniques have been used for particle adhesion measurements. In the centrifugal detachment method, the adhesion between particles and the surface is measured by the balance of centrifugal force generated by the rotating surface. Several researchers [68-75] demonstrated the use of the centrifugal method for measurement of adhesion strengths between particles and surfaces. The advantage of the ability of the centrifugal process to obtain data for the relatively large number of particles in a single experiment, and hence provide a relevant sample in only a few experiments. The centrifugal method measures direct lift-off force and is not used to examine for rolling removal mechanism. Deryagin and Zimon [75] developed a vibrational technique to the range of adhesion forces that could be measured over a wide range of surface accelerations. A comprehensive review and techniques for calculating the adhesion of particles are presented by Zimon [76].

The AFM, centrifugal and vibrational methods are well-developed, but the equipment can be expensive, and the measurements are time-consuming. Visser [77] studied the removal of individual particles from a solid surface through the flow between two concentric cylinders in liquid. Hydrodynamic forces were generated by the rotation of one cylinder with the other cylinder at rest. He concluded that the removal of submicron particles depends only on the wall shear stress (τ_w). The hydrodynamic force exerted on a spherical particle adhering to a flat surface was then

found to be a direct function of the shear stress [78]. In a comprehensive review, Van den Tempel [79] suggested that the hydrodynamic technique allows for the study of a greater adhesion force than is accessible by centrifuge methods. Hubbe [80] analyzed the detachment of particles from the flat surfaces in a gas flow and demonstrated that the effect of an aerodynamic force acting parallel to the wall is greater than the normal force. In other words, the lift detachment mechanism for removal may be neglected. Sharma, Chamoun, Sarma and Schester [81] investigated the hydrodynamic detachment of particles from the surface and demonstrated that the mechanism of the detachment of particles in size range of 5 μm to 40 μm is indeed controlled by rolling and not by sliding or lifting mechanisms. When rolling is assumed, torque analysis becomes critical. The torque balance model of Hubbe more accurately described the physical behavior of particles in aerodynamic removal than that of the model given by Visser; the drag force required to remove the particles was found to be about two orders of magnitude smaller than the adhesion force.

4.2 Analytical Methods

4.2.1 *Adhesion Force Modeling*

Surface adhesion forces include van der Waals forces (vdW), electric double-layer forces, solvation forces, hydrogen bonding, contact deformation, and chemical bonding. Multiple reviews of particle adhesion and removal have been conducted [71]. The effect of the environmental parameters can be significant in real-world situations. In a controlled environment, the dominant adhesion mechanism is the vdW interaction [82]. In the 1930s, Hamaker [83] and Derjaguin [84] applied the vdW theory to particle surface interactions. Initially, the models assumed a smooth, nondeformable particle and a flat plate. Derjaguin [85] considered the effect of contact deformation

on particle adhesion. The total vdW force for a smooth, deformable particle adhering to (in contact with) a smooth surface is,

$$F_{vdW} = \frac{A_H R}{6{D_0}^2} \tag{4.1}$$

where A_H is the system-dependent Hamaker constant. 0 shows the values used in this work.

Table 4.1. Parameter value used in the calculations

Material	Poisson's Ratio	Young's Modulus	Hamaker Constant	Adhesion Work
Soda Lime Glass	0.22	7.2×10^{10} Pa	$\sim 6.45 \times 10^{-20}$ J	10-35 mJ/m^2

Several theories describe the elastic deformation of a spherical particle in contact with a flat plate; the calculations of the contact radius (a) involve the particle and surface properties and the applied load (F) on the particle. The first of these theories were developed by Hertz [86] who neglected the particle adhesion force. Johnson–Kendall–Roberts (JKR) [87] and Derjaguin-Muller-Toporov (DMT) [85] considered the adhesion effects based on the surface energy and adhesion work and developed formulations for the contact radius (a) and the adhesion force (F_{ad}) for a spherical particle on a flat surface

Table 4.2. The relation between the contact radius a and the adhesion force F_{ad} for a spherical particle on a flat surface with no applied load according to JKR and DMT theories.

	DMT	JKR
a	$\sqrt[3]{\frac{2\pi W_A R^2}{E_{tot}}}$	$\sqrt[3]{\frac{6\pi W_A R^2}{E_{tot}}}$
F_{ad}	$2\pi R W_A$	$\frac{3\pi R W_A}{2}$

For both theories, the contact radius can be written as a function of the reduced Young's modulus $E_{tot,}$ the work of adhesion W_A, and the radius of the sphere. The JKR theory is used when soft systems or larger particles are being considered, while the DMT theory is generally used for

hard systems and for smaller particles. Tabor [88] proposed to identify regions where the JKR and DMT theories are applicable based on λ:

$$\lambda = \frac{2.06}{D_0} \sqrt[3]{\frac{RW_A^2}{\pi E_{tot}^2}} \tag{4.2}$$

where R is the particle radius, D_o is the typical interatom spacing, and E_{tot} is the reduced Young's modulus, defined as:

$$E_{tot} = \frac{4}{3}\left[\frac{1-\gamma_1^2}{E_1} + \frac{1-\gamma_2^2}{E_2}\right]^{-1} \tag{4.3}$$

Here, γ_i and E_i are, respectively, the Poisson ratio and Young's modulus of the material. JKR is applicable when $\lambda \gg 1$, while the DMT theory has a better fit for systems where $\lambda \ll 1$. In this work, we calculate that for silica microparticles and glass test substrates, $\lambda \approx 1$, thus the results should fit between the two theories. Maugis [89] extended on these works to characterize the transition between JKR and DMT theories.

4.2.2 *Aerodynamic Forces*

A particle in shear flow experiences aerodynamic drag and lift forces, which may result in particle detachment from the surface. Aerodynamic forces depend on the flow field in the vicinity of the particle and the flow around the particle itself. The calculation of the adhesion force is based on the threshold force for removal and the moment balance acting on the particle. Figure 4.1 shows a model for a deformable particle of diameter (d), adhering to a smooth surface in a shear flow. The forces considered in the moment balance are the adhesion force, the gravitational force (mg), the drag force (F_d), and the lift force (F_l). Particle detachment depends on the relationship of these forces, the contact radius (a), and several other factors, such as the distance between the applied

force and the surface (h), the surface roughness (δ), the particle-surface charges, and the environmental factors. In this work, h is calculated from the CFD simulation and δ is measured to be on the order of 2-6 nm and neglected in the analysis; the effect of the surface charges and relative humidity (RH) are neglected as all experiments are performed at RH<10% levels.

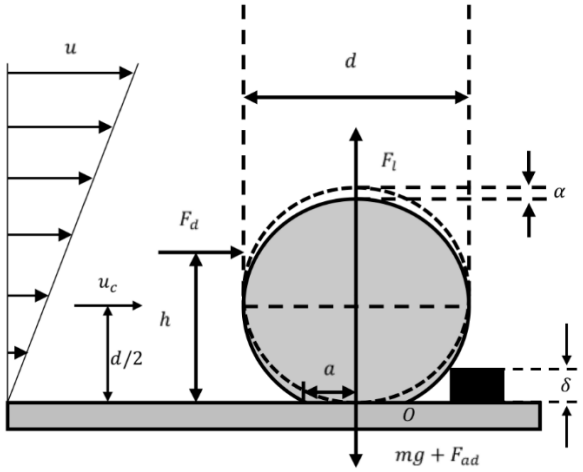

Figure 4.1. Schematic diagram of a microparticle adhesion/removal model on a surface in shear flow with linear velocity profile. The flow is fully developed at the particle location.

The effect of the Saffman lift force [90] in the shear flow has been previously considered in aerodynamic resuspension, but is not applicable when considering particles attached to a wall; an alternate formulation is necessary to account for the no-slip condition, i.e., zero velocity at the contact point. O'Neill [91] assumes the lift force is negligible when presenting an exact solution of the linearized Stokes viscous flow around a fixed sphere in contact with a fixed plane wall and derives the drag force that the fluid exerts on the sphere. Mollinger and Nieuwstadt [92] analytically derived an expression for a lift on a sphere attached to a wall. They found that it is insignificant relative to drag for low particle Reynolds numbers. The drag force in work by O'Neill [91] is determined as a combination of a pressure difference between the particle and shear force on the surface of the particle. For a microparticle in a laminar shear flow, a modified Stokes law is used to describe the drag force (F_D),

$$F_d = 1.7009 \cdot 3\pi\mu D V_c \tag{4.4}$$

where μ is the fluid viscosity, and V_c is the fluid velocity at the center of the particle. The constant 1.7009 is developed from an exact solution; it accounts for the shear flow velocity profile. Due to the symmetry, forces in the direction perpendicular to the surface (lif, gravity) do not contribute to the moment. Hence, the aerodynamic moment about the detachment location, M_d, is given by:

$$M_d = F_d \cdot h \tag{4.5}$$

The moment arm, $h = 0.7 \cdot d$, is the location of the equivalent point force from the pressure and shear force acting on the particle, and h is computed by the CFD for the entire range of the experimental conditions; the value agrees with the analytical solution [25]. The moment can be explicitely written as:

$$M_d = 1.2 \cdot 3\pi\mu D^2 V_c \tag{4.6}$$

These expressions have been shown to be limited to Stokes Flow (Re<1). In this work, we calculate the particle drag and lift force using CFD for the experimental range of the particle Reynolds numbers(~1-5). The contribution of lift force is found to be of the same order of magnitude as the gravity force and orders of magnitude lower than the drag force suggesting that particle resuspension does not occur by the lift-off mechanism.

The region outside the viscous sublayer presents difficulties with the transition to turbulence leading to a nonlinear velocity profile. For this reason, we consider only the particles that are positioned within the viscous sublayer, where non-dimensional distance is less than five ($y^+ < 5$). This limitation is expressed in Eq. (1-7)

$$d < 5\sqrt{\frac{\mu^2}{\rho\tau_w}} \tag{4.7}$$

Combining Eq. (1-7) with the definitions of Reynolds number and assuming a linear viscous sublayer we can determine a nondimensional limit for our assumptions:

$$Re = \frac{\rho V_c d}{\mu} \tag{4.8}$$

$$V_c = \frac{\tau_w d}{2\mu} \tag{4.9}$$

$$\sqrt{\frac{2\mu^2 Re}{\rho \tau_w}} = d \tag{4.10}$$

$$\sqrt{\frac{2\mu^2 Re}{\rho \tau_w}} < 5\sqrt{\frac{\mu^2}{\rho \tau_w}} \tag{4.11}$$

$$Re < 12.5 \tag{4.12}$$

The particle Reynolds number for removal must be less than 12.5 in order to use the linear shear flow assumption. In order to use this method for Reynolds numbers greater than 12.5 a more sophisticated formulation of drag force would be necessary.

4.2.3 *Models for Adhesive Resistance to Rolling*

Wang [93] originally proposed that an adhesive particle resistance to rolling can be calculated from the moment created by the adhesion force acting at the center of the contact circle. His work led to the conclusion that, for rolling removal, the ratio of the critical removal force to the adhesion force is approximately equal to the ratio of the contact radius to the radius of the microsphere. Ziskind et al. [94] extended the approach by analyzing the maximum adhesive moment acting about the contact radius with respect to the pull-off force; the authors show that the maximum adhesive moments are $\frac{2}{3}F_{ad} * a$ and $\frac{1}{2}F_{ad} * a$ for the JKR and DMT theories, respectively. Dominik and Tielens [95] theorize that the value for static rolling moment resistance is characterized by asymmetry

in the contact pressure. They developed an expression for the adhesive moment as a function of pull-off force, P, normalized contact radius, $\hat{\alpha}$, and the shifted contact area distance, ζ.

$$M_{ad} = 4P\hat{\alpha}\zeta \tag{4.13}$$

This expression is not used in this work as the shifted distance is difficult to determine. Instead, the relationships presented in Ziskind et al. [94] are used.

4.2.4 *Moment Based Methodology for Adhesion Force Calculation*

Tsai et al. [96] and Soltani and Ahmadi [97] assumed that the particle is detached when the external force moment about the point ‘‘O,’’ at the rear perimeter of the contact circle, overcomes the resisting moment. Using Ziskind’s et al. results [94] for the DMT adhesive moment, the criterion for removal becomes:

$$F_d \cdot h \geq \left(\frac{F_{ad}}{2} + mg - F_l\right) \cdot a \tag{4.14}$$

$$\frac{F_{ad}}{2} = \frac{F_d h}{a} + F_l - mg \tag{4.15}$$

Neglecting the lift force and gravity, (4.15) becomes:

$$\frac{F_{ad}}{2} = \frac{F_d h}{a} \tag{4.16}$$

Substituting the contact radius (see DMT theory in Table 1), the equation for adhesion force becomes:

$$F_{ad} = \left[2F_d * h * \left(\frac{E_{tot}}{R}\right)^{\frac{1}{3}}\right]^{\frac{3}{4}} \tag{4.17}$$

In summary, the established experimental methods and models are limited in the quantification of the lateral forces prevalent in aerodynamic particle resuspension and applications to environmentally relevant particle aging scenarios. A more direct, non-contact method is needed. The work of the previous investigators provides sufficient information to formulate and apply a robust method for calculating the microparticle adhesion force in aerodynamic resuspension scenarios. In this work, we propose that a combination of numerically calculated aerodynamic forces acting on the particle and the particle detachment experiments in the controlled wall shear stress environment allows for the estimation of threshold forces required for particle detachment, thus enabling the calculation of particle adhesion forces. Our research methodology consists of (i) calculating the aerodynamic drag and lift forces acting on a particle in the boundary layer, (ii) experimentally determining the threshold force values for particle resuspension, and (iii) based on the moment balance, calculating the particle adhesion force in aerodynamic resuspension.

4.3 NUMERICAL METHODS

Numerical modeling provides a unique capability of determining the aerodynamic forces acting on an arbitrary shape particle in the complex flow scenarios, such as laminar, turbulent and transitional boundary layers, as well as for the complex surface geometries and morphologies. Here, the CFD simulations are performed to determine the aerodynamic forces acting on the spherical particle in the laminar boundary layer. The forces are compared with the analytical solution to validate the approach and to determine the limitations of the method. The analytical solution provides the necessary information to compute the drag force, lift force, and moment for spherical particles using the modified Stokes' law in a low particle Re number region ($Re<1$). However, the forces in the low Re region may not be sufficient for particle resuspension.

Computational analysis is performed using the commercial software code ANSYS FLUENT 16. In this study, two CFD models are used: (i) a global model that simulates the flow field inside the flow cell, and (ii) a local model for flow in the vicinity of the particle. The former model is used for the design of the flow cell and to obtain the shear stresses and boundary velocity profiles for the local model as a function of the experimental inlet conditions. The boundary layer profile is used as the flow profile inlet for the simulation of the flow around the particle. The local model is used to compute the velocity field near the particle, as well as the forces acting on the particle, significantly reducing the computational demands that would arise when attempting to resolve flow around an individual particle using global flow cell simulations.

4.3.1 *Flow Cell Model*

The CFD simulations are performed to optimize the flow cell geometry and to gain insight into the boundary layer and shear stress profiles in the flow cell. Figure 4.2 shows the 3D model of the flow cell. The computational domain includes a cylindrical inlet, transition section, and 1mm high test section enclosed by microscope glass slides. The inlet section has an inner diameter of 7 mm and a length of 15 mm. The transition section converts the flow to the rectangular test section with minimum changes in the cross-sectional area to avoid the onset of flow instabilities; it has has a length of 45 mm. The test section is confined by two microscope glass slides; it is 75 mm long and 25 mm wide. Mesh optimization is performed to resolve the viscous sublayer to capture τ_w as defined by a non-dimensional wall distance of $y^+ = 5$. To resolve the flow in the viscous sublayer, we use at least three cells within this region; the first grid point is located at a distance of $y^+ \approx 1$. Further refinement of the mesh did not result in changes in the boundary layer profile. The computational domain mesh consists of about 1,000,000 quadrilateral elements.

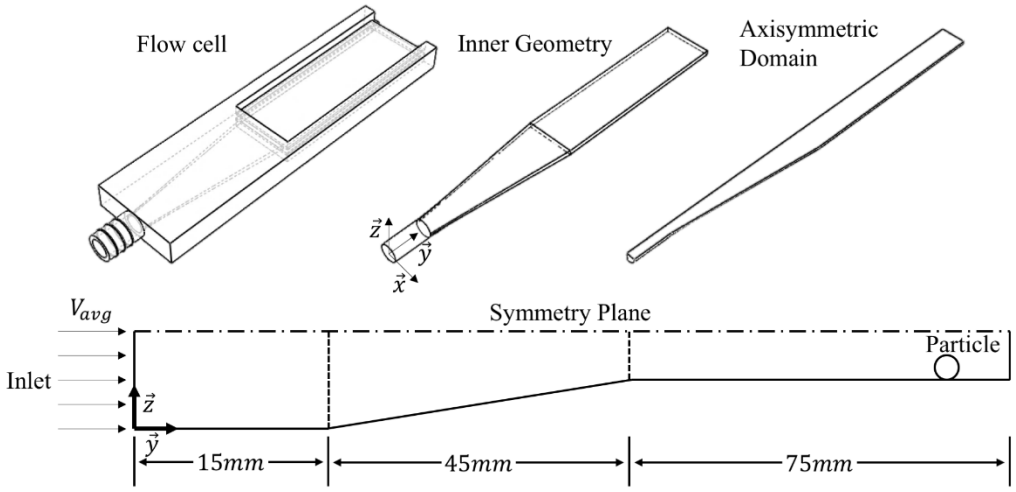

Figure 4.2. Top: flow cell geometry; Bottom: schematic of the computational domain (not to scale). A quarter of the domain is modeled due to symmetry. The inlet is set as the velocity boundary conditions; the outlet is set the atmospheric pressure boundary condition.

The choice of the turbulence model considers the requirement to resolve the near-wall boundary layer. The standard $k-\varepsilon$ model yields consistent results for free shear flows with relatively small pressure gradients but struggles in wall-bounded flows with larger pressure gradients [98]. The $k-\omega$ model has been shown to be superior to the $k-\varepsilon$ model in the flow near the wall and transitional (laminar to turbulent) region, but it suffers from numerical instability. The shear stress transport (SST) $k-\omega$ turbulence model [99] is a two-equation turbulent viscosity model that combines the best of both the $k-\varepsilon$ and $k-\omega$ models. The use of the $k-\omega$ formulation in the inner parts of the boundary layer makes the model directly applicable to resolving the viscous sub-layer. The SST formulation switches to a $k-\varepsilon$ behavior in the free-stream and, thereby, avoids the common k-ω problem of hypersensitivity to the initialization and inlet conditions. The SST $k-\omega$ model can be used as a low Reynolds number turbulence model without secondary damping functions and is a well-suited option for this work. The inlet boundary condition for the flow is a uniform velocity profile; the velocity magnitude is determined from the measured flow rate for each experimental condition. Wall boundary conditions are no-slip walls; the outlet is

modeled as an ambient pressure boundary condition. The inlet turbulence length scale is set based on a fully-developed turbulent flow in a pipe to 3.8% of the hydraulic diameter.

4.3.2 *Modeling of Flow Around a Particle*

We consider the case of a spherical particle attached to a flat surface in a wall-bounded linear shear flow. Figure 4.3 shows the computational domain and the closeup view of the mesh at the particle location. To avoid potential numerical difficulties at the contact point, in the CFD study, we modeled particle contact radius (a) to be half of the particle diameter. A contact cylinder is constructed to address this issue while maintaining the height of a spherical particle. The actual contact area may be significantly smaller than the one in the simulation domain; however, the contact cylinder is the near-zero velocity region, the flow around the particle and the calculated drag and lift forces are not influenced by this approximation. In the calculation of the moment of the forces acting on the particle, the contact length is taken from the literature.

After performing the mesh independence analysis, the computational domain uses about 1,000,000 hexahedral elements. The mesh is refined at the particle surface to capture velocity gradients and the forces acting on the particle. Because we are modeling the viscous sublayer, and low particle Reynolds numbers, a laminar model is sufficient. Table 3 describes the numerical approach and boundary conditions. The inlet velocity profile is imported from the flow cell simulation; the proportionality constant k is determined based on the flow cell simulation for a given test condition.

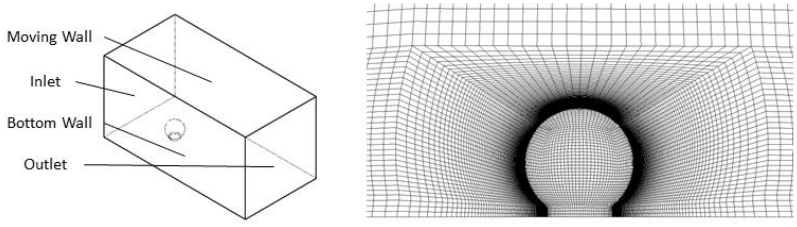

Figure 4.3. Schematic of the computational domain and mesh used for the velocity field and the particle forces computation.

Table 4.3. The boundary conditions in the CFD simulation of flow around a particle.

Boundary	Boundary Conditions
Inlet	$u = ky$
Outlet	Ambient pressure (0 psi)
Top wall	Moving wall $u_{top} = kl$
Bottom wall	Stationary Wall $u_{wall} = 0$
Sidewalls	Symmetry Planes
Particle	Stationary Wall (no slip)

4.4 EXPERIMENTAL METHODS

Experiments are conducted to determine flow parameters corresponding to the particle detachment. Figure 4.4 shows a schematic of the experimental setup. The flow cell housing is fabricated using 3D printing. The compressed shop air provides flow for the experiments; the air is filtered, and the inlet pressure and the flow rate is adjusted using a pressure regulator (ARG20, SMC, Inc., IN). The flow rate is controlled by the valve; the flow rate is monitored by a digital flow meter (TopTrak 820, Sierra Instruments, Inc., CA). The metered, conditioned air stream enters the flow cell connected to the flowmeter by flexible tubing. The flow rate measured during the experimental process is used as the input for the CFD simulation.

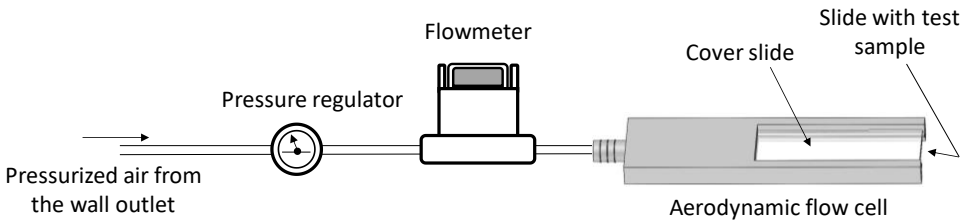

Figure 4.4. The aerodynamic flow cell setup used to study the resuspension of particles from a glass surface. The flow is controlled using a pressure inlet; the flow rate is measured by the flow meter.

4.4.1 *Testing Procedure*

Polydispersed soda-lime glass spheres in the 12-26 micron size range (SLGMS-2.5 10-22 μm, Cospheric LLC, Santa Barbra, CA) are used for all experiments. The surface roughness of the particle is not reported by the manufacturer, but has been evaluated using SEM and is assumed negligible. Standard 25 mm x 75 mm microscope glass slides are pre-cleaned in an ultrasonic bath and dried using compressed filtered dry air. The roughness of the slides is determined to be between 2 nm - 6 nm using profilometer measurements (DektakXT, Bruker Corp., MA). The slides are stored in the desiccator for 12 hours to ensure moisture removal. The microspheres are deposited gravitationally onto slides by dry nebulization. The dry nebulization is performed inside an aerosol chamber using a disposable aerosol vaporizer (HealthLine Corp., NY). The humidity in the chamber is controlled in the range of 30-40%. The method provided good repeatability and particle deposition uniformity. The glass slides with deposited particles are then placed in a desiccator for 24 hours before they interrogated in the aerodynamic flow cell. The relative humidity in the experiment is measured by the RH meter, typically below 5%. At the beginning of each experiment, creeping flow (at ~10% of the experimental flow rate) is used to dehumidify the system for 3-4 minutes. This step removes the moisture in the setup without removing the particles. To perform the time-independent experiment, each test is conducted until no more particles are

being removed. In a preliminary study, we found that a flow exposure time of 30 seconds is appropriate for reaching steady-state particle removal at all flow conditions. Before each experiment, all parts of the flow cell are cleaned with pressurized air to ensure that no outside particles are introduced in the experiments.

4.4.2 *Microscopic Analysis*

Removal efficiency is evaluated microscopically by imaging test coupons before and after exposure in the flow cell. An Olympus BX 60 microscope is fitted with a digital camera (OptixCam Summit D3K2). ToupCam software is used to acquire images. The resolution of each image is 14 megapixels. The images are taken at the center of the slide to avoid the potential side wall effect. Only the leading edge of the particle deposition is evaluated. Though the method limits the number of total particles in the experiments; the rationale for this is two-fold: (i) to avoid the ambiguity associated with particle relocation from the upstream to downstream locations, and (ii) to reduce the probability of particle removal by contact, wherein the particle removed from the upstream location travels along the surface (i.e., rolling, sliding, bouncing), comes into contact with the particle at the downstream location, and results in the detachment of the latter particle. The images are first processed using a custom MATLAB subroutine to remove any non-circular objects. The images are then imported into the microscopic image analysis software (Structure, iMicrotech Inc., NY), which stitches the selected images, sorts the particles by size, and counts the particles in the experiment.

Each experiment consists of particles being exposed to airflow at the assigned flow rate; the removal fraction in each particle size bin (1 micron) is recorded as a single data point. In a typical experiment, 1200 particles are observed with a minimum of 40 particles in each size bin. A total of 120 experiments are performed, with approximately 4200 particles in each bin size

analyzed for removal. The analysis of the 50% threshold removal condition is based on N_{total}= 5897 particles; the minimum number of particles in each size bin is N_{min}=113.

4.5 RESULTS

4.5.1 *Modeling Results*

Numerical simulations provide an insight into the forces exerted on particles in the boundary layer. Though the simulations of the flow cell do not directly result in the particle force information, they allow for establishing the operational envelope and limitations of the system. The key results of the flow cell analysis are: (i) calculated τ_w values as a function of the flow rate in the cell, (ii) velocity profile in the boundary layer that serves as an input for simulations of the flow around the particle, and (iii) determination of the flow regime (i.e., laminar, transitional, turbulent) as a function of distance from the wall, defining the range of particle sizes that can be used in the experimental study.

The velocity profile and the test particle size enables the calculation of the particle Re number and the direct comparison of the force computed by the CFD with the analytical solution. The analytical solutions of the drag coefficient and drag force are obtained from (2-1) as a function of the particle Re number. The inlet boundary condition and the particle size are varied to achieve Re = 0.001 - 1000. While this work is limited to the region of Re<12.5, we address the entire range from Stokes to Newton region, not to suggest that particle Reynolds numbers of up to 1000 are relevant, but for comparison to past work and for developing a more robust relationship for drag acting on the particle. The normal pressure and shear stress terms acting on the particle from the CFD are integrated over the entire surface of the particle to calculate the resulting F_d, F_l, and the moment arm - h. The moment arm does not vary significantly (<1%) for all conditions, the drag

and lift forces increase with the particle Re. Figure 4.5 plots the aerodynamic forces against the particle Re from the numerical simulation, calculated by the modified Stokes Law. The CFD drag force agrees well with the analytical solution in the Stokes region (Re<1). However, for the Re>1 region, F_d calculations the diverge from the analytical solution due to the onset flow separation in the wake of the particle. The numerical simulations allow for the development of an empirical relationship of drag force as a function of the particle Re number, including the transitional region between the Stokes and Newton drag laws. The equation (0-18) describes the best fit for the drag force as a function of the particle Reynolds number in the high shear stress region, specifically in the wall boundary layer for Re = 0.001-1000.

$$F_d = 1.7009 \cdot 3\pi \frac{\mu^2}{\rho} Re\left(1 + \frac{Re^{0.82}}{12.23}\right) \tag{4.18}$$

The numerical simulation also proves an empirical fit for the drag coefficient C_d for a particle in the viscous boundary layer for Re = $0.001 - 1000$. While the analytical work of O'Neill [25] shows the analytical solution for particles Re<1, we extend the range for the drag coefficient calculation to the transitional regime ($1 < Re < 1000$):

$$C_d = 1.7009 \cdot \frac{24}{Re}\left(1 + 0.071Re^{0.85}\right) \tag{4.19}$$

The CFD calculates the lift force on a sphere in a shear flow; the magnitude of the lift force is at least an order of magnitude lower than the drag force. The difference is the greatest for particles with the lower Reynolds Number. Our results are compared to the results of O'Neil and Zeng [100] in Figure 4.5.

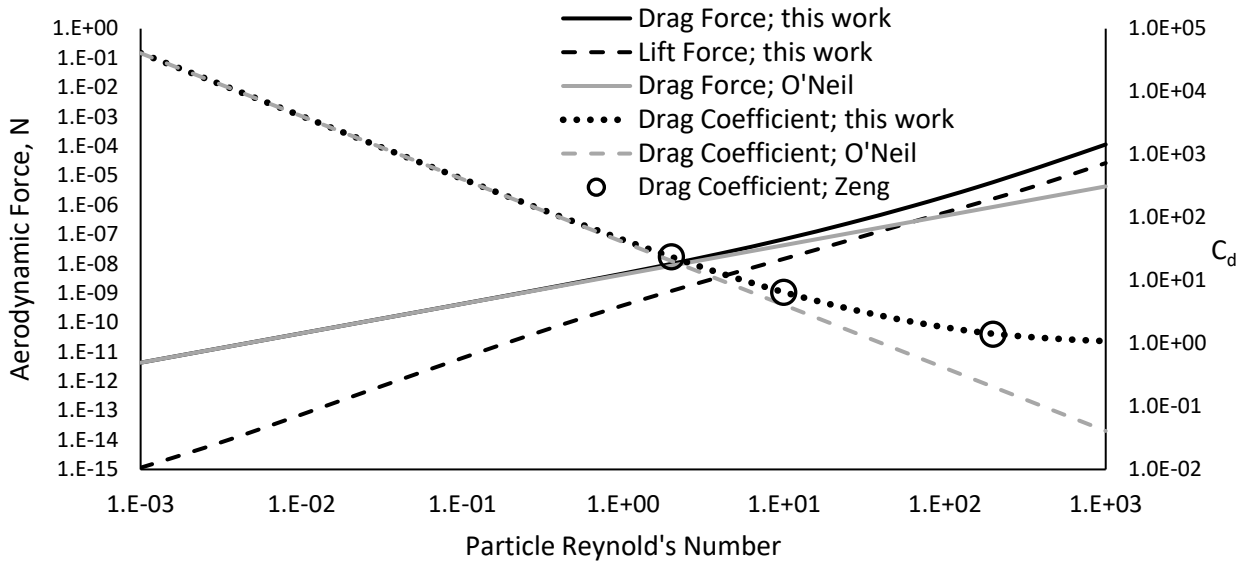

Figure 4.5. Compression of the drag and lift force from the CFD results with modified Stokes law for the sphere as a function of the particle's Reynold's number in shear flow.

4.5.2 *Experimental Results*

The relationship between the drag force and experimental particle resuspension data allows the threshold values for particle detachment to be determined. The threshold forces associated with 50% particle detachment (F_{d50}) are determined experimentally for each particle size; these are used for the calculation of particle adhesion force by a moment balance from Eq. (0-17). Although in this work, the critical force corresponds to the resuspension of 50% of the particles as it provided the most consistent results, other threshold values can be used. Figure 4.6 shows the threshold τ_w and F_d values as a function of particle size. While the drag force is directly used in the adhesion force calculation, the shear stress is a very useful independent parameter, providing flow boundary layer characterization independent of particle size and morphology.

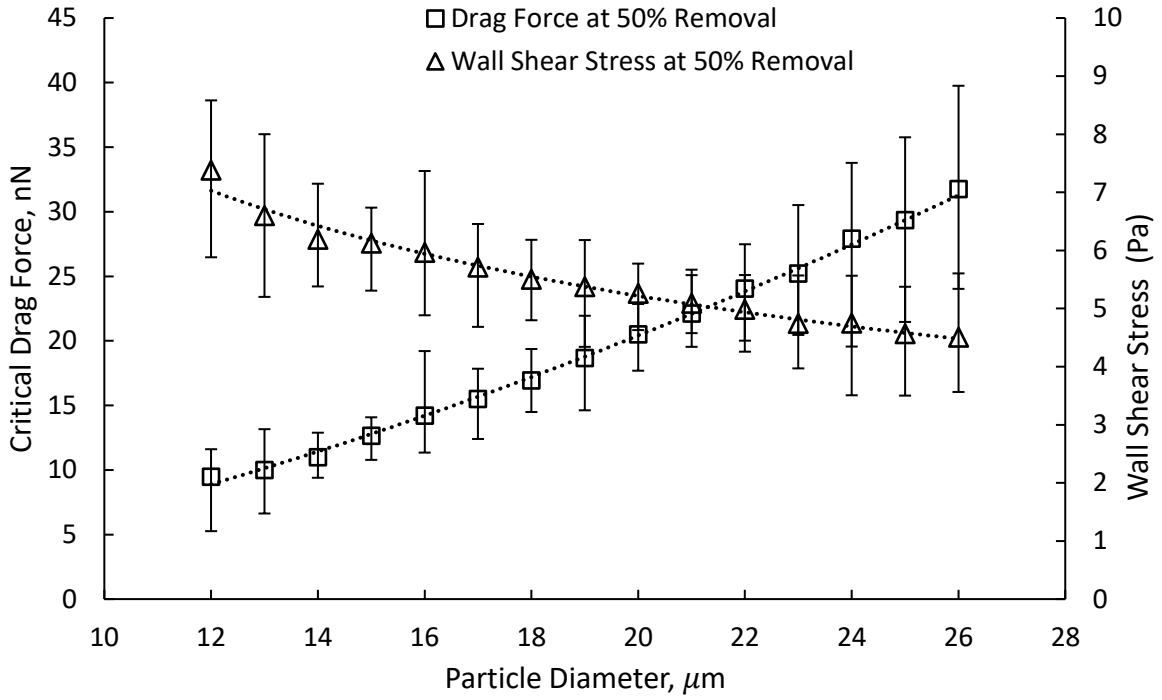

Figure 4.6. Critical drag force and τ_w for the removal of 50% of silica glass spheres. The number of observed particles in the 50% threshold removal is N_{total} = 5897, N_{min} = 113 (in the 1-micron size bin). The critical drag force is proportional to $D^{1.6}$, while the critical τ_w is shown to be proportional to $D^{-0.58}$.

The threshold force required to resuspend the particle increases as particle diameter increases; the threshold shear stress necessary for resuspension decreases as particle diameter increases. Equations (5-3) and (5-4) show the empirical relationship of the threshold drag force in nanoNewtons and critical shear stress in Pascals as a function of the particle diameter in micrometers.

$$F_{d50} = 0.1564 \cdot d^{1.63} \tag{4.20}$$

$$\tau_{50} = 29.915 \cdot d^{-0.58} \tag{4.21}$$

Using DMT and JKR theories and assumptions for contact area and adhesion force when conducting a moment balance yields an analytical relationship where the critical drag force for

particle detachment by rolling is proportional to $d^{2/3}$; our data shows a greater dependence on the particle size (see Table 4).

The experimentally determined threshold values of F_{d50} can be used in calculating the contact radius and adhesion force associated with 50% particle resuspension. The contact radius can be calculated using assumptions from DMT and JKR theories. Table 4 shows the relationships used in the calculations. Figure 4.7 shows the contact radius as a function of particle size, calculated using the experimental data for F_{d50} values, and compares the values with the DMT and JKR theories. Figure 4.7 shows that, for silica microspheres on a smooth glass surface, the DMT theory is appropriate; the JKR lines diverge while the DMT lines are closer together.

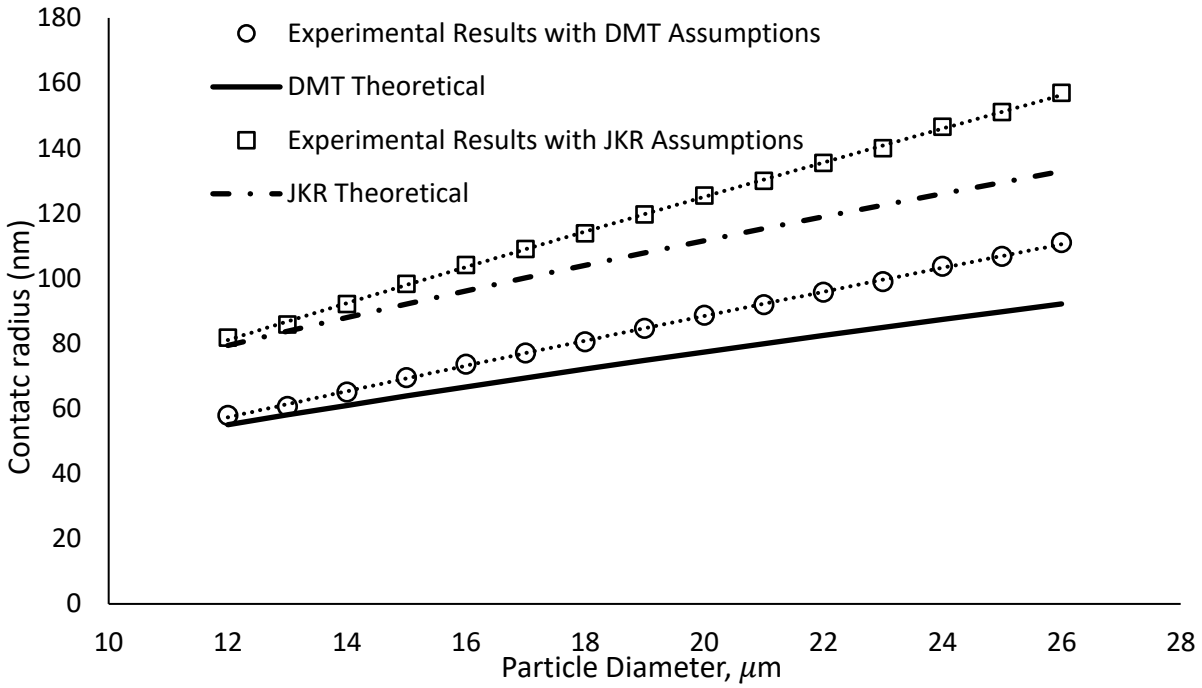

Figure 4.7. The contact radius for silica glass particles on a smooth glass surface vs. particle size. The experimental results for the 50% removal threshold and DMT and JKR assumptions are compared with the theoretical relationships.

Figure 4.7 shows a comparison of the experimental data using DMT and JKR assumptions (see Table 1) with the vdW force as well as analytical relationships using DMT and JKR adhesion theory and rolling removal assumptions. The experimental data has a better agreement with the

DMT theory. The adhesion force has a higher dependency on particle diameter than is predicted by theory. The error bars are greater for the larger particles due to their limited number in the size bin (N_{min} =113). The experimental F_{ad} is greater than the van der Waals force. Additionally, the AFM measurements of silica glass adhesion are included [101,102]. Direct comparisons of the dry adhesion force of silica microspheres on a glass surface are difficult to obtain for the particle in size range considered in this work. The AFM data are lower than the calculated adhesion force from the aerodynamic method. Several possible explanations can be considered to explain the difference. (i) Influence of particle detachment mechanisms – the perpendicular force in AFM measurements would result in rapid vertical pop-off versus rolling, where the detachment mechanism is more gradual with a possible relationship to the crack propagation theories [103]. (ii) The difference in the mechanical properties roughness of the microspheres and surface can result in a change of the contact radius and adhesion work terms in our calculations, thus in the estimation of the F_{ad}. (iii) The most likely explanation, however, is the particle deformation during the 24-hour aging period, in which the particles conform to the surface, resulting in a contact area increase, thus an increase of the adhesion force. The AFM technique examines the adhesion force based on the momentary contact of the particle and the surface. The effect of particle aging on the contact area as a function of the particle size, particle, and surface properties requires additional modeling and experimental investigation.

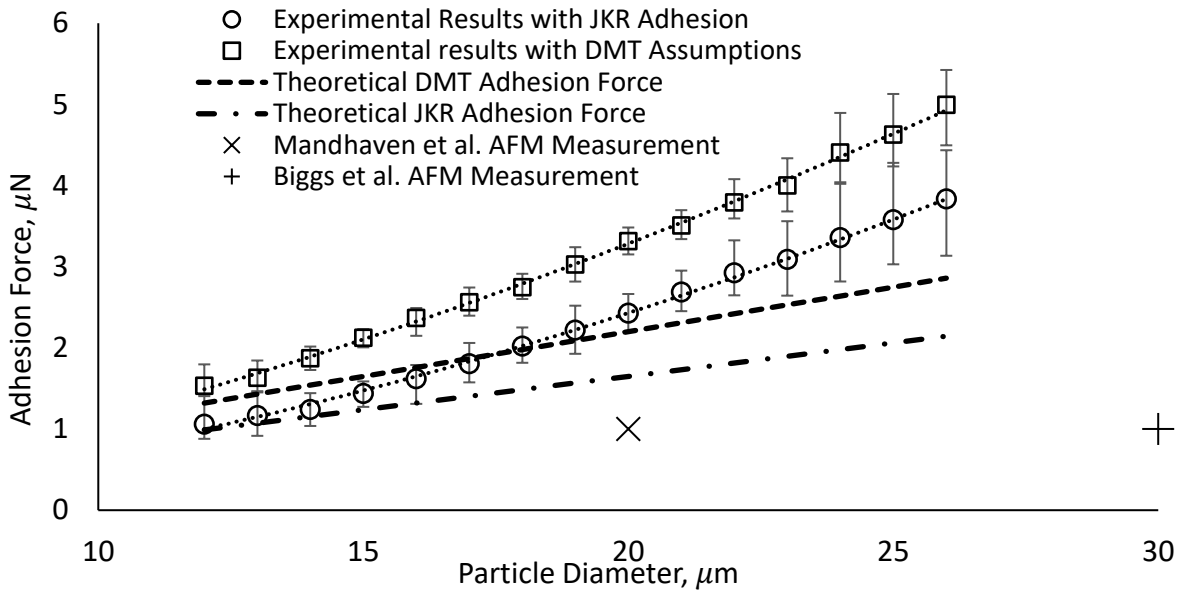

Figure 4.8. The experimental adhesion force of silica particles on a glass slide calculated with DMT and JKR assumptions vs. the JKR and DMT models and the AFM [101,102]; N_{total} = 5897, N_{min} = 113 (in each size bin).

Table 4 provides a summary of the results and a comparison with the known theoretical relationships. While the magnitude of the forces and deformations parameters are consistent, the experimental trends have a greater dependency on particle size. This is likely due to the differences in particle detachment mechanisms, changes associated with particle aging, surface and particle mechanical properties, and their surface roughness used in our calculations. These assumptions affect the contact radius and adhesion work terms, thus the estimation of F_{ad}. The relationships presented in Table 4 are representative of the adhesion force associated with the aerodynamic detachment of an aged particle by rolling on a smooth surface. The theoretical relationships are obtained by using the equations for adhesion force in Table 1 and rearranging Eq. (0-17) to solve for the parameter of interest.

Table 4.4. Comparison of relationships between the critical drag force for rolling removal, adhesion force, contact radius, and diameter. Constants c_1, c_2, & c_3 are experimentally determined and dependent on properties of the particle, contact surface, and units.

	Critical Drag Force, F_{d50}	Adhesion Force, F_{ad}	Contact Radius, a
Experimental Relationship	$c_1 d^{1.63}$ $c_1 = .1564 \frac{nN}{\mu m^{1.63}}$	$c_2 d^{1.55}$ $c_2 = 0.0319 \frac{\mu N}{\mu m^{1.72}}$	$c_3 d^{0.85}$ $c_3 = 6.952 \frac{nm}{\mu m^{0.91}}$
Theoretical relationship using DMT theory	$\frac{(\pi W_A)^{\frac{4}{3}}}{(2E_{tot})^{\frac{1}{3}}} d^{\frac{2}{3}}$	$\pi W_A d$	$\sqrt[3]{\frac{\pi W_A}{2E_{tot}}}\, d^{\frac{2}{3}}$
Theoretical relationship using JKR theory	$\frac{4(\pi W_A)^{\frac{4}{3}}}{3(2E_{tot})^{\frac{1}{3}}} d^{\frac{2}{3}}$	$\frac{3\pi W_A}{4} d$	$\sqrt[3]{\frac{3\pi W_A}{2E_{tot}}}\, d^{\frac{2}{3}}$
Van der Waals Relationship	*N/A*	$\frac{A_h}{12 D_0^2} d$	*N/A*

4.6 Summary for Adhesion Force in Aerodynamic Resuspension

In this work, we developed a method that combines a numerical calculation of aerodynamic forces acting on the particle and the controlled aerodynamic particle detachment experiments, enabling the calculation of particle adhesion forces. The aerodynamic method for determining the particle adhesion forces relies on the estimation of forces acting on the particle in the boundary layer from the CFD or the available analytical or empirical relationships. The adhesion force is derived from the moment balance needed to initiate the detachment of the particle by rolling. The geometric parameters required to construct the moment balance can be obtained from the previously published models or empirical data. A detachment of aged silica microspheres from a smooth glass surface is studied experimentally in a flow cell to determine the threshold drag force values required for particle detachment. The primary findings are related to the method development and results obtained from this approach, which, in summary, are:

- The aerodynamic method for determining the particle adhesion force provides consistent results with the DMT [104] and JKR models [87]; however, the trends, proportionality constants, and dependence on the particle diameter differed slightly from the theoretical model.
- Based on the best data fit, the critical drag force (F_{D50}) for silica particle removal from the glass slide is proportional to $d^{1.6}$, compared to the expected $d^{2/3}$ using DMT and JKR models.
- From the moment balance, the effective particle adhesion force and contact radius are found to be proportional to the particle diameter, as: $F_{ad} \sim d^{1.72}$; $a \sim d^{0.91}$ compared to the linear relationship for adhesion and $d^{\frac{2}{3}}$ relationship for contact radius from the DMT and JKR models.

In addition to the described method for the estimation of the particle adhesion by aerodynamic forces, some conclusions relevant to the particle behavior in the boundary layer flow can be made:

- The drag force computed numerically is consistent with the modified Stokes flow theory [25] for *Re*<1. For *Re*>1, it is necessary to use the CFD or empirical fit to determine the drag force.
- An empirical relationship (Eq. 4-2) between the drag coefficient and particle *Re* in a linear shear flow is developed for transitional (Stoke to Newton drag) flow regimes ($1 < Re < 10^3$).
- The lift force is consistently at least at an order of magnitude less than the drag force and several orders of magnitude less than the adhesion force.

The limitations of this study are related to the particle size and ability to interrogate relatively low adhesion forces, due to the assumption that the particles need to be contained within the viscous

sublayer and a fully developed flow. The shear stresses considered in this work are relatively low due to the low adhesion force between the silica particles and glass surface. Other fluid dynamic systems can be used to study the particle adhesion force if the relationship between the flow and shear stress can be quantified. For example, particle detachment by the impinging jet [2,20,105-109]; the shear stresses systems can be as high as 2kPa [7]. A combination of shear stress calculations and particle removal data in the impinging jet system can extend the application of the method to higher adhesion force systems.

The aerodynamic measurement method is sensitive to the surface and the particle roughness parameters: at the inception of the rolling motion, the particle may need to overcome the effect of asperities on the test surface or the particle surface. While smooth surface assumptions are used in this study, the sensitivity to the microscopic geometry at the particle surface interface allows the surface roughness effects, and particle morphology need to be studied in rolling detachment scenarios. Application of the methods over a range of parameters and comparisons to the findings previously reported in the literature: relative humidity (RH=0-100%) [110], electrostatic force, particle aging (deformation) on the surface, and surface properties [72,97,111]. Of particular interest is the extension of the method to systems with greater adhesion forces. The practical application of the presented work will include analysis resuspension rates related to the particle fate in the environment and optimization non-contact surface sampling methods.

Chapter 5. AERODYNAMIC FORCES ON PROLATE SPHEROIDS RESTING ON A SURFACE IN A LINEAR SHEAR FLOW

This work is submitted for publication in Powder Technology.

Though the aerodynamic forces acting on a spherical particle are well studied, in many real-world applications, the particles are non-spherical, and there are currently no established relations for forces on non-spherical particles resting on a surface. We developed new relations for the aerodynamic forces on prolate-spheroidal particles attached to a surface in a linear shear flow using direct numerical simulations. The presented formulations predict drag and lift coefficients as a function of the particle aspect ratio, flow incidence angle, and Reynolds number. The predictive model agrees with the DNS results for the drag and lift coefficients within 0.3% and 3%, respectively.

5.1 INTRODUCTION

Understanding aerodynamic forces acting on particles resting on a surface is crucial in the fields of study where particle resuspension is of interest. These particles are often irregularly shaped, but recent scientific research treats such particles as spheres, as there are no established relations for non-spherical particles. This presents the need for formulations for aerodynamic forces on non-spherical particles.

O'Neil [91] first derived an analytical expression for the aerodynamic forces experienced by a spherical particle at rest on a surface in shear flow in the low Reynolds number ($Re<1$) Stokes regime, but particle resuspension often necessitates higher Reynolds numbers. Zeng[100] conducted a comprehensive numerical study on stationary and moving particles on a surface in a shear flow and developed robust relations for aerodynamic forces. The work by Zeng was expanded upon

first by Lee et al. [112], then Fillingham et al. [61] investigated critical shear rates for particle resuspension. Yahiaouiet al.[113] characterized forces in a parabolic velocity profile. While existing work has led to a comprehensive understanding of aerodynamic forces on spherical particles, particles of interest, for example, in trace explosive detection, tend to be oblong and rest along their long axis[114], rendering models for forces on spherical particles inadequate.

There has been significant recent work into the characterization of aerodynamic forces for non-spherical particles. Militzer[115] first developed expressions for drag on prolate spheroids in axisymmetric flows. Holzer[116] produced a model for drag on arbitrary particle shapes. Ouchene et al.[117,118] and Zastawny et al. [119] each constructed models for lift, drag, and torque on arbitrary particle shapes in uniform flows. Harper[120] first developed an analytical model for the calculation of lift for an ellipsoidal particle in a shear flow. Still, it is limited to particles far away from a surface. Gavse et al. [121] formulated expressions for the lift on ellipsoidal particles in shear flow near the surface, but the method diverges as the distance to the surface approaches zero. Cui et al.[122] described a force-based model for tracking the movement of ellipsoidal particles in arbitrary shear flows; however, the method does not apply to a particle resting on a surface. There remains a lack of comprehensive models for the problem of non-spherical particles attached to surfaces. In this work, we present a parametric computational study of flow over prolate spheroids resting on a surface for the characterization of the lift and drag force as a function of Reynolds number, orientation and aspect ratio.

5.2 METHODOLOGY

5.2.1 *Problem Description*

Typical particles of interest for surface cleaning and aerodynamic sampling will be on the order of microns in height, and therefore under any aerodynamic removal scenario will be resting

in the linear viscous sublayer of a turbulent boundary layer [61]. When at rest, particles will lie with their long axis parallel to the surface. Thus, for this work, we consider rigid prolate spheroids resting on a surface parallel to their long axis in a linear shear flow. The coordinate axis is attached to the surface at the center of the spheroid with x-, y-, and z-coordinates representing the streamwise, wall-normal, and spanwise directions, respectively. The incidence angle θ is definied as the rotation of the spheroid about the y-axis, as shown in Figure 5.1.

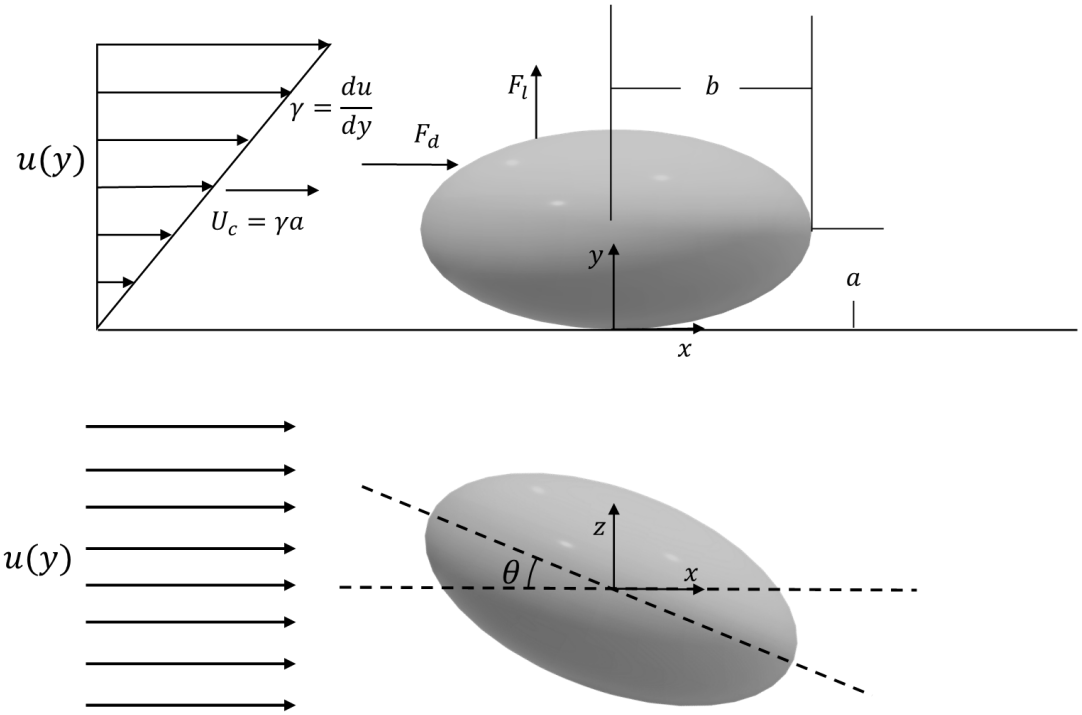

Figure 5.1. Schematic diagram of a prolate spheroid resting on the surface in a shear flow with a side-view (top) and top-veiw (bottom).

We define the aspect ratio, η, of the particles as the ratio of the major axis to the minor axis:

$$\boldsymbol{\eta = \frac{b}{a}}. \tag{5.1}$$

Such that an aspect ratio of 1 represents a sphere. In this work, we investigate aspect ratios of $1.5, 2, 3$, and 5 each at angles, θ, of $0°, 30°, 45°, 60°$, and $90°$.

The characteristic length scale, d_p, for the prolate spheroids is taken to be the volume equivalent spherical diameter. The characteristic velocity for a prolate spheroid in a linear shear flow is the flow speed at $y = a$, such that in a flow of shear rate γ, $U_c = \gamma a$. This gives us the definition of our Reynolds number for the problem:

$$Re = \frac{U_c d_p}{\nu} = \frac{2\gamma a (a^2 b)^{\frac{1}{3}}}{\nu} \tag{5.2}$$

In a realistic removal scenario for microparticles are positioned entirely in a linear shear flow, the height of a particle must be less than the width of the viscous sublayer of a turbulent boundary layer ($h^+ < 5$). In Fillingham et al. [61], the author demonstrated that this leads to a maximum Reynolds number of 12.5 for spherical particles. For a prolate spheroidal particle resting on its long axis, the limit can be defined as

$$\frac{Re}{\eta^{\frac{1}{3}}} < 12.5, \tag{5.3}$$

which provides a physical limit that conveniently aligns with the range of Reynolds numbers for which the flow will stay steady and attached [100,112]. For this reason, the Reynolds numbers considered in this work are in the range of 0.1-10.

Finally, we define the drag and lift coefficients for the problem using the spherical equivalent diameter and the flow velocity U_c at $y = a$ such that:

$$C_D = \frac{F_d}{\frac{1}{2}\rho U_c^2 \pi \frac{d_p^2}{4}}, \qquad C_L = \frac{F_L}{\frac{1}{2}\rho U_c^2 \pi \frac{d_p^2}{4}} \tag{5.4}$$

5.2.2 *Computational Approach*

The commercial finite volume solver, Ansys Fluent 18.2, was used to solve the three-dimensional, steady, incompressible Navier Stokes equations.

$$\nabla \cdot \mathbf{u} = 0 \tag{5.5}$$

$$(\mathbf{u} \cdot \nabla)\mathbf{u} = -\frac{1}{\rho}\nabla \mathrm{p} + \nu\nabla^2\mathbf{u} \tag{5.6}$$

Simulations are performed in a rectangular domain with dimensions $L_x = 50d_p$ and $L_y = L_z = 10d_p$. With boundary conditions shown in Table 1. To avoid a singularity at the contact point between the particle and the surface particles were modeled at a small gap of $0.01d_p$ away from the surface.

Table 5.1 Boundary conditions for numerical simulations on flow over particles

Inlet	Top	Sides	Particle	Bottom	Outlet
$u = \gamma y$	$u = \gamma L_y$	$u = \gamma y$	$u = 0$	$u = 0$	$\frac{\partial u}{\partial x} = 0$
$v = 0$	$v = 0$	$v = 0$	$v = 0$	$v = 0$	$\frac{\partial v}{\partial x} = 0$
$w = 0$	$w = 0$	$w = 0$	$w = 0$	$w = 0$	$\frac{\partial w}{\partial x} = 0$
$\frac{\partial p}{\partial x} = 0$	$\frac{\partial p}{\partial y} = 0$	$\frac{\partial p}{\partial z} = 0$	$\frac{\partial p}{\partial \vec{n}} = 0$	$\frac{\partial p}{\partial y} = 0$	$\frac{\partial p}{\partial x} = 0$

The computational grid is clustered near the particle surface to enhance resolution in the region of interest while reducing the overall computational cost. The grid is constructed such that the non-dimensional spacing, $\Delta^+ = \frac{\Delta * u^+}{\nu}$, is less than unity in each direction at the surface of the particle for the highest Reynolds number case. A mesh independence study was conducted, with the results summarized in Table 2.

Table 5.2 Mesh independence study for the case of $\boldsymbol{Re = 8.73, \eta = \frac{2}{3}, \theta = 30°}$. $\boldsymbol{\Delta y_p^+}$ and $\boldsymbol{\Delta x_p^+}$ represent non-dimensional grid spacing at the surface of the particle. $\boldsymbol{\Delta x_p^+ \approx \Delta z_p^+}$ for all cases.

Mesh	$[N_x, N_y, N_z]$	Δy_p^+	Δx_p^+	C_D	C_L
Course	[128,63,38]	0.29	1.45	7.754	1.713
Medium	[256,126,76]	0.145	0.725	7.749	01.706
Fine	[512,252,152]	.073	0.363	7.748	01.706

The mesh independence study shows that the coarse mesh is inadequate, but any further refinement beyond the medium mesh is unnecessary.

5.3 RESULTS

5.3.1 *Drag Coefficient*

The drag coefficient for a sphere resting on a surface has been previously studied, and a relationship based on the Reynolds number has been established[100]:

$$C_D = 1.7009 * \frac{24}{Re}(1 + .104Re^{0.75}) \tag{5.7}$$

For prolate spheroids, then it is natural to use the existing expression for spherical particles with correction factors for orientation and aspect ratios. When examing the effect of aspect ratio on drag coefficient at each angle, as shown in Figure 5.2, it appears that adjustment to the spherical relation is necessary for $\theta = 0$ (the volume equivalent diameter accounts for the variation due to the elongation of the particle) but the effect of aspect ratio increases with the angle θ.

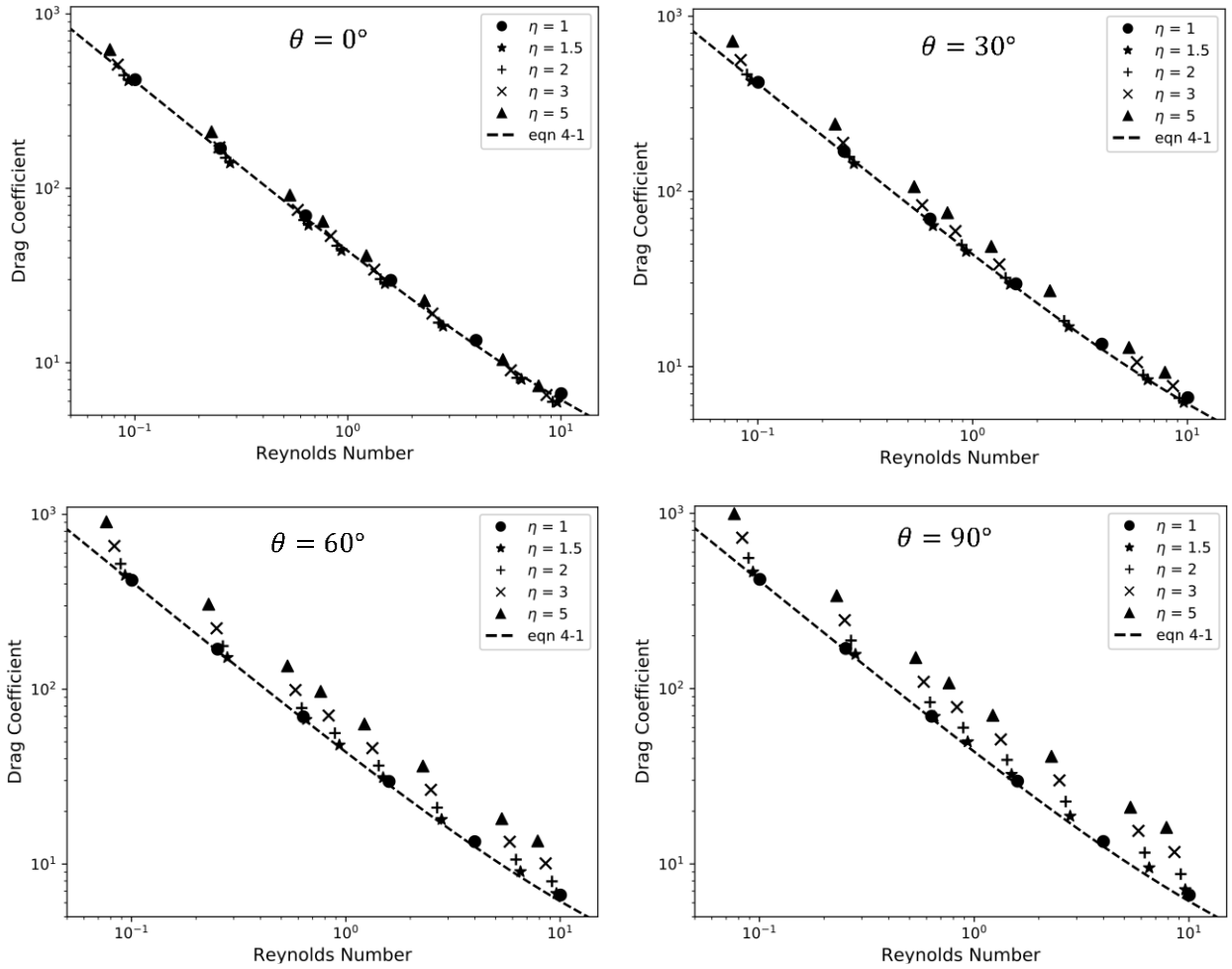

Figure 5.2. Drag coefficient from DNS against particle Reynolds number for incidence angles of $0°, 30°, 60°$ and $90°$ at all aspect ratios. The effect on aspect ratio on deviation from the spherical relation is most prominent at an angle of $90°$.

For determining the effect of incidence angle on the drag coefficient, we look to relations established for prolate spheroids in a uniform flow. Happel and Brenner[123] found that the drag coefficient varies with the square of the sine of the incidence angle as

$$C_D = C_{D,\theta=0} + \left(C_{D,\theta=90} - C_{D,\theta=0}\right) \sin^2 \theta \tag{5.7}$$

Figure 5.3 shows that the formulation agrees well for prolate spheroids in a linear shear flow.

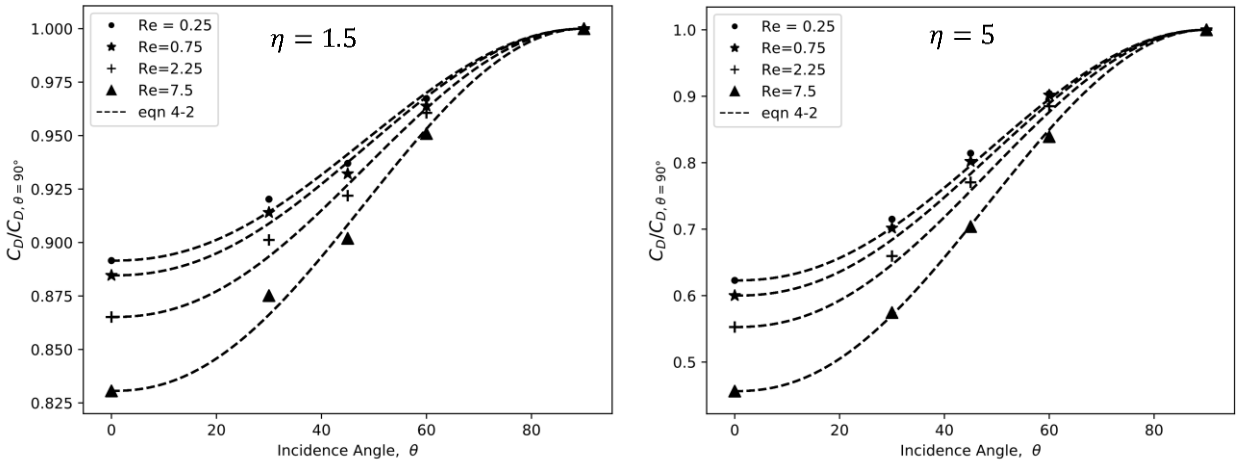

Figure 5.3. Drag coefficient from DNS normalized by drag coefficient at an incidence of 90° plotted against incidence angle for comparison of theoretical relation by Brenner. The $\sin^2\theta$ relation is appropriate for spheroids in a shear flow attached to a surface.

To fully characterize the drag coefficient, we seek expressions for incidence angles of $\theta = 0°$ and $\theta = 90°$ as a function of Reynolds number and aspect ratio in the following form:

$$C_{d,\theta=0} = 1.7009 * \frac{24}{Re}(\eta^{\alpha_1} + 0.104\eta^{\alpha_2}Re^{0.75} + \alpha_3(\eta-1)^{\alpha_4}Re^{\alpha_5})$$
$$C_{d,\theta=90} = 1.7009 * \frac{24}{Re}(\eta^{\beta_1} + 0.104\eta^{\beta_2}Re^{0.75} + \beta_3(\eta-1)^{\beta_4}Re^{\beta_5}) \quad (5.9)$$

Such that the equations converge to that of a sphere as the aspect ratio goes to unity. The coefficients as determined by least-squares fitting to the numerical simulations are summarized in Table 3.

Table 5.3 Summary of fitting parameters for drag coefficient expressions at 0° and 90°

	1	2	3	4	5
α	0.523	−0.442	−0.483	−0.003	0.625
β	0.405	0.636	−0.162	0.0856	−0.121

The expression allows predicting the drag coefficient with a mean deviation from DNS results of 0.8% and a maximum deviation of 3.1%, see Figure 5.4.

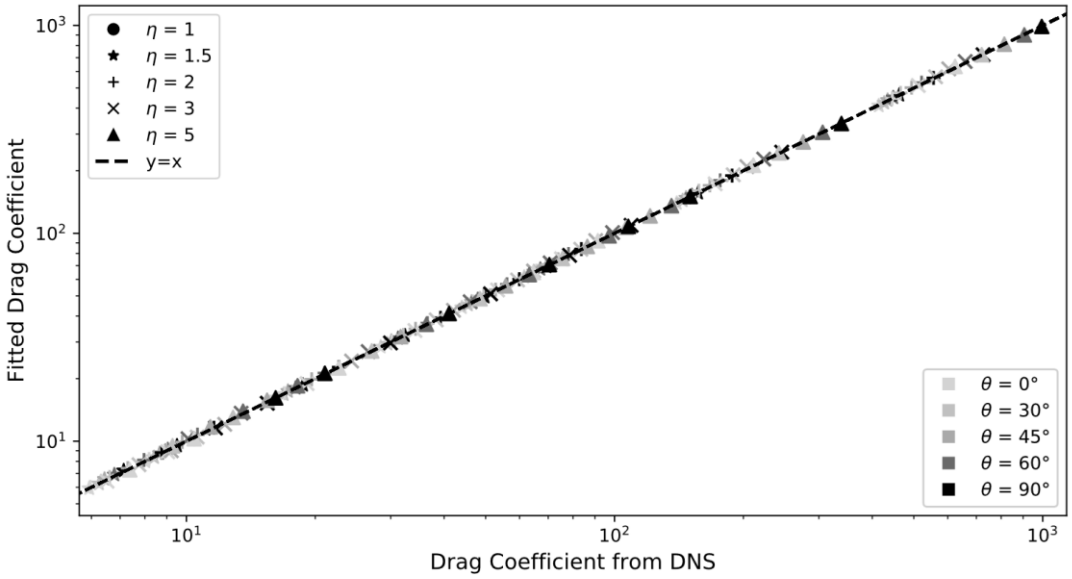

Figure 5.4. Drag coefficient predicted by the correlations developed in this work against the results from a direct numerical simulation. The fitted drag coefficient agrees with the DNS results with a maximum deviation of 3.1%.

5.3.2 *Lift Coefficient*

As with the drag coefficient, Zeng[100] established a relation for the lift coefficient of a sphere resting on a surface in linear shear flow:

$$C_L = \frac{3.663}{(Re^2 + 0.1173)^{0.22}} \tag{5.10}$$

As with the formulation for the drag coefficient, we will be basing our equation for the lift coefficient on this existing relation.

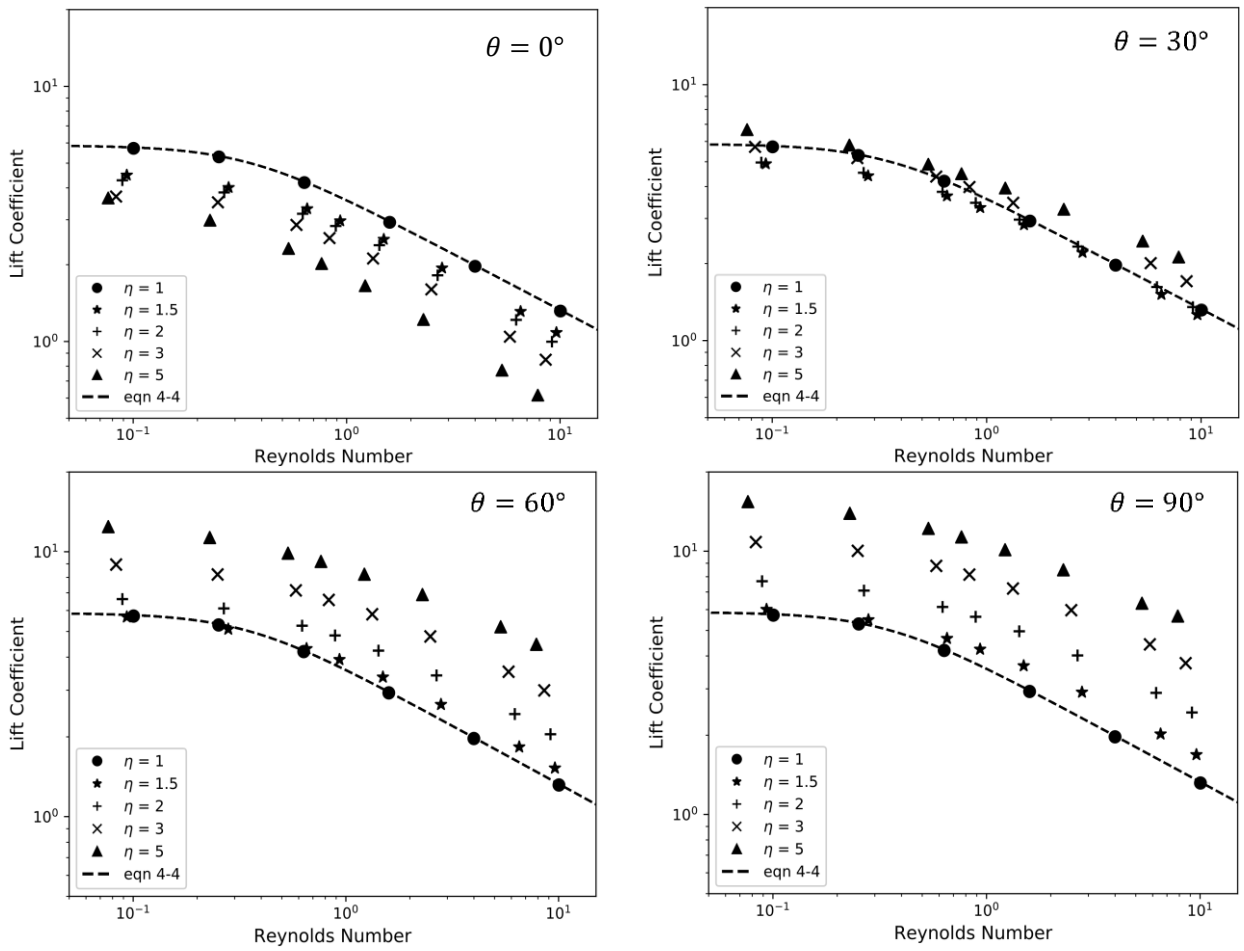

Figure 5.5. Lift coefficient against particle Reynolds number for incidence angles of $0°, 30°, 60°$ and $90°$ at all aspect ratios with comparison to the lift coefficient for a sphere. The lift coefficient decreases with aspect ratio at low angles of incidence but increases with aspect ratio at higher angles.

Figure 5.5 shows the dependence of the lift coefficient on the aspect ratio is highly dependent on the incidence angle. For a $90°$ incidence angle, the lift coefficient increases drastically with aspect ratio while it decreases drastically at an incidence of $0°$. For all aspect ratios, the maximum lift occurs at $90°$ incidence and the minimum at $0°$. Our formulation contains the terms for incidence angle, the Reynolds number, and a stand-alone aspect ratio term. The correlation also must converge to that of a sphere at an aspect ratio of 1. Thus, we propose a formulation in the form:

$$C_L = \frac{3.663(1 + Re^{\lambda_3}(\eta - 1)^{\lambda_4} \sin^2\theta)}{(\eta^{\lambda_1} Re^2 + 0.1173\eta^{\lambda_2})^{0.22}} \tag{5.11}$$

Table 4 summarizes the fitting parameters found via the least-squares fitting.

Table 5.4 Summary of fitting parameters for lift coefficient expressions.

	1	2	3	4
λ	2.021	1.559	0.165	1.218

The lift coefficient is more difficult to characterize than drag, but the correlation still agrees with the DNS for all cases. The final expression for lift has a mean deviation of 4.4% and a maximum deviation of 16.2%. Figure 5.6 plots the predicted lift coefficient against the results from DNS.

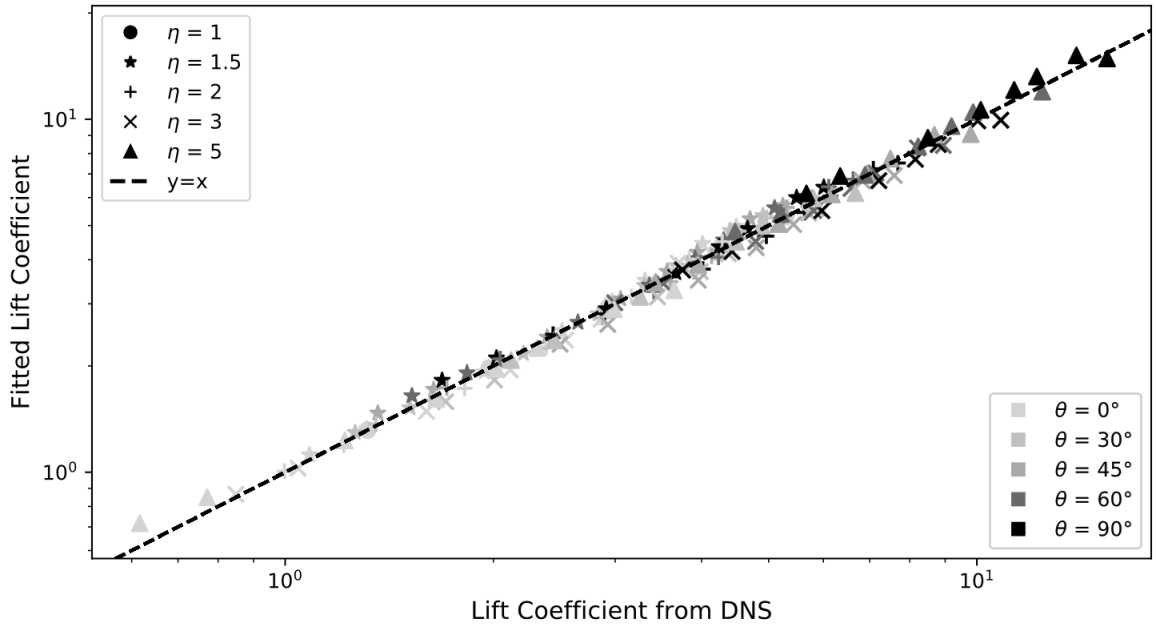

Figure 5.6. The lift coefficient predicted by the correlations developed in this work against the results from the direct numerical simulation. The fitted drag coefficient agrees with the DNS results with a maximum deviation of 16.2%.

5.4 SUMMARY FOR FORCES ON PROLATE SPHEROIDS

In this work, we formulate a set of equations for predicting the drag and lift coefficients on prolate spheroids resting on a surface in a linear shear flow as a function of incidence angle, aspect ratio, and Reynolds number. Direct numerical simulations were conducted for prolate spheroids with the aspect ratios up to 1:5, Reynolds numbers from 0.1-10, and at incidence angles of $0°, 30°, 45°, 60°$, and $90°$. The numerical results provide a large parametric data set for developing fitting parameters for drag and lift coefficients. The new correlations converge to that of Zeng[100] at an aspect ratio of unity. Table 5 presents the final expressions and their mean and max deviations.

Table 5.5 Summary of lift and drag coefficient formulations

Expression	Mean deviation	Max deviation
$C_{D,\theta=0°} = 1.7009 * \frac{24}{Re}(\eta^{0.523} + 0.104\eta^{-0.442}Re^{0.75} - 0.483(\eta-1)^{-0.003}Re^{0.625})$	0.57%	1.71%
$C_{D,\theta=90°} = 1.7009 * \frac{24}{Re}(\eta^{0.523} + 0.104\eta^{0.636}Re^{0.75} - 0.162(\eta-1)^{0.0856}Re^{-0.121})$	0.43%	1.43%
$C_D = C_{D,\theta=0} + \left(C_{D,\theta=90} - C_{D,\theta=0}\right)\sin^2\theta$	0.81%	3.11%
$C_L = \frac{3.663(1 + Re^{0.165}(\eta-1)^{1.218}\sin^2\theta)}{(\eta^{2.021}Re^2 + 0.1173\eta^{1.559})^{0.22}}$	4.41%	16.2%

For the drag coefficient, the variation as a function of angle follows the $\sin^2\theta$ trend as reported by Happel and Brenner for uniform flow, such that the drag coefficient is minimum at an incidence of $0°$ and maximum at $90°$. The predictive model for the drag coefficient for a prolate

spheroid resting on a surface agrees with the DNS results within 3.1% over a range of flow angles $\theta = 0°$-90°, Re<10, and particle aspect ratios up to 1:5.

For the lift coefficient relation, it is not useful to compare to results for uniform flow. Thus, a new formulation is developed by adding adjustment terms for aspect ratio and incidence angle to the equation developed by Zeng et al. [100]. The lift coefficient increases with aspect ratio for an incidence of 90° while it decreases with aspect ratio for an incidence of 0°. Establishing a correlation for lift is more challenging; our best fit for the lift coefficient has a maximum deviation of 16.2%.

Chapter 6. CONCLUSIONS

The work in this dissertation has furthered the design and development of aerodynamic particle sampling by developing a deeper understanding of the flow of underexpanded impinging jets and their resulting wall jet boundary layer coupled with developing formulations for the forces on microparticles resting in the developed boundary layers.

The first accomplishment is the parametric characterization of the wall shear stress generated from axisymmetric impinging jets. The work resulted in a set of equations that allow for the mapping of wall shear stress based upon jet nozzle parameters. This wall shear stress mapping allows for the prediction of particle removal, or the determination of necessary conditions for particle removal, using axisymmetric impinging jets.

The second accomplishment is another parametric study of planar underexpanded impinging jets, resulting in a full similarity analysis that allows for *the complete calculation of the wall jet velocity and wall shear stress anywhere along the impingement surface as a function of*

nozzle parameters. As with axisymmetric impinging jets, this knowledge can be used to determine the necessary nozzle parameters for the removal of microparticles from a surface.

Along with characterizing underexpanded impinging jets, I have developed a model for determining the adhesion force and aerodynamic forces on spherical particles resting in a boundary layer. By describing the forces experienced by particles, we gain an essential understanding of the necessary conditions for particle removal.

Finally, the forces on prolate spheroids resting in a boundary layer were investigated, *resulting in a set of equations to predict the aerodynamic forces within an average deviation from the DNS results within 3%.* These formulations allow for a straight-forward calculation of forces on non-spherical particles that is crucial for understanding the aerodynamic resuspension of non-spherical particles.

The presented thesis provides insight into the fluid dynamics of aerodynamic particle resuspension. The results assisted in the development of non-contact surface sampler and can be applied for the development of reduced-order models for particle resuspension. The future work can include the parameterization of irregular and deforming particles, such as biological aerosols, and the development of physics-based models describing particle fate in the environment.

BIBLIOGRAPHY

1 Marshall, M. & Oxley, J. C. *Aspects of explosives detection*. (Elsevier, 2011).

2 Smedley, G. T., Phares, D. J. & Flagan, R. C. Entrainment of fine particles from surfaces by gas jets impinging at normal incidence. *Experiments in Fluids* **26**, 324-334, doi:10.1007/s003480050295 (1999).

3 Fletcher, R., Briggs, N., Ferguson, E. & Gillen, G. Measurements of Air Jet Removal Efficiencies of Spherical Particles from Cloth and Planar Surfaces. *Aerosol Science and Technology* **42**, 1052-1061, doi:10.1080/02786820802402237 (2008).

4 Verkouteren, J. R. Particle characteristics of trace high explosives: RDX and PETN. *Journal of forensic sciences* **52**, 335-340 (2007).

5 Keedy, R., Dengler, E., Ariessohn, P., Novosselov, I. & Aliseda, A. Removal Rate of Explosive Particles From a Surface by Impingement of a Gas Jet. *Aerosol Science and Technology* **46**, 148-155 (2012).

6 Kottapalli, K. & Novosselov, I. V. Experimental study of aerodynamic resuspension of RDX residue. *Aerosol Science and Technology*, 1-13, doi:10.1080/02786826.2019.1587377 (2019).

7 Fillingham, P., Murali, H. & Novosselov, I. V. Nondimensional Parameter for Characterization of Wall Shear Stress From Underexpanded Axisymmetric Impinging Jets. *Journal of Fluids Engineering* **139**, 111102 (2017).

8 Murali, H. (eds Igor V. Novosselov, James Riley, & Uri Shumlak) (ProQuest Dissertations Publishing, 2016).

9 Henderson, B. & Powell, A. Experiments Concerning Tones Produced By An Axisymmetric Choked Jet Impinging On Flat Plates. *Journal of Sound and Vibration* **168**, 307-326 (1993).

10 Krothapalli, A., Rajkuperan, E., Alvi, F. & Lourenco, L. Flow field and noise characteristics of a supersonic impinging jet. *J Fluid Mech* **392**, 155-181 (1999).

11 Tam, C. K. W. & Ahuja, K. K. Theoretical model of discrete tone generation by impinging jets. *Journal of Fluid Mechanics* **214**, 67-87 (1990).

12 Donaldson, C. d. & Snedeker, R. S. A study of free jet impingement. Part 1. Mean properties of free and impinging jets. *Journal of Fluid Mechanics* **45**, 281-319 (1971).

13 Kalghatgi, G. T. & Hunt, B. L. Occurence of Stagnation Bubbles in Supersonic Jet Impingement Flows. *Aeronautical Quarterly*, 169-185 (1976).

14 Alvi, F. S., Ladd, J. A. & Bower, W. W. Experimental and Computational Investigation of Supersonic Impinging Jets. *AIAA Journal* **40**, 599-609 (2002).

15 Chin, C. *et al.* Investigation of the Flow Structures in Supersonic Free and Impinging Jet Flows. *Journal of Fluids Engineering* **135** (2013).

16 Samareh, B., Stier, O., Lüthen, V. & Dolatabadi, A. Assesment of CFD modelling via flow visualization in cold spray process. *Journal of Thermal Spray Technology* **18**, 934-943 (2009).

17 Young, R. M., Hargather, M. J. & Settles, G. S. Shear stress and particle removal measurements of a round turbulent air jet impinging normally upon a planar wall. *J Aerosol Sci* **62**, 15-25, doi:10.1016/j.jaerosci.2013.04.002 (2013).

18 Tu, C. V. & Wood, D. H. Wall pressure and shear stress measurements beneath an impinging jet. *Experimental Thermal and Fluid Sciences* **13**, 364-373 (1996).

19 Smedley, G. T., Phares, D. J. & Flagan, R. C. Entrainment of Fine Particles from Surfaces by Gas Jets Impinging at Normal Incidence. *Experiments in Fluids* **26**, 324-334 (1999).

20 Phares, D. J., Smedley, G. T. & Flagan, R. C. The wall shear stress produced by the normal impingement of a jet on a flat surface. *Journal of Fluid Mechanics* **418**, 351-375 (2000).

21 Birch, A. D., Hughes, D. J. & Swaffield, F. Velocity Decay of Pressure Jets. *Combustion Science and Technology* **52**, 161-171 (1987).

22 Fluent, A. *14.5 Theory Guide*. (ANSYS Inc., 2012).

23 Miettinen, A. & Siikonen, T. Application of pressure-and density-based methods for different flow speeds. *International Journal for Numerical Methods in Fluids* **79**, 243-267 (**2015**).

24 Menter, F. R. Two-equation eddy viscosity turbulence models for engineering applications. *AIAA Journal* **32**, 1598-1605 (1994).

25 Catalano, P. & Marcello, A. An evaluation of RANS turbulence modelling for aerodynamic applications. *Aerospace Science and Technology* **7**, 493-509 (2003).

26 Settles, G. S. *Schlieren and Shadowgraph Techniques: Experimental Fluid Mechanics*. (Springer-Verlag, 2001).

27 Fillingham, P. & Novosselov, I. V. Wall jet similarity of impinging planar underexpanded jets. *International Journal of Heat and Fluid Flow* **81**, 108516, doi:https://doi.org/10.1016/j.ijheatfluidflow.2019.108516 (2020).

28 Martin, H. in *Advances in heat transfer* Vol. 13 1-60 (Elsevier, 1977).

29 Rahimi, M., Owen, I. & Mistry, J. Impingement heat transfer in an under-expanded axisymmetric air jet. *International journal of heat and mass transfer* **46**, 263-272 (2003).

30 Hofmann, H. M., Kind, M. & Martin, H. Measurements on steady state heat transfer and flow structure and new correlations for heat and mass transfer in submerged impinging jets. *International Journal of Heat and Mass Transfer* **50**, 3957-3965 (2007).

31 Xu, P., Qiu, S., Yu, M., Qiao, X. & Mujumdar, A. S. A study on the heat and mass transfer properties of multiple pulsating impinging jets. *International Communications in Heat and Mass Transfer* **39**, 378-382 (2012).

32 Kalghatgi, G. & Hunt, B. The occurrence of stagnation bubbles in supersonic jet impingement flows. *The Aeronautical Quarterly* **27**, 169-185 (1976).

33 Tu, C. V. & Wood, D. H. Wall pressure and shear stress measurements beneath an impinging jet. *Exp Therm Fluid Sci* **13**, 364-373, doi:10.1016/S0894-1777(96)00093-3 (1996).

34 Loureiro, J. & Freire, A. S. Wall shear stress measurements and parametric analysis of impinging wall jets. *International Journal of Heat and Mass Transfer* **55**, 6400-6409 (2012).

35 Kottapalli, K., Novosselov, I. V., Mamishev, A. V., Aliseda, A. & Mamidala, R. *Aerodynamic Removal and Characterization of Particulate Trace Residues on Model Surfaces*, University of Washington Libraries, (2017).

36 Glauert, M. The wall jet. *J Fluid Mech* **1**, 625-643 (1956).

37 George, W. K. *et al.* A similarity theory for the turbulent plane wall jet without external stream. *Journal of Fluid Mechanics* **425**, 367-411 (2000).

38 Gersten, K. The asymptotic downstream flow of plane turbulent wall jets without external stream. *J Fluid Mech* **779**, 351-370 (2015).

39 Schlichting, H. & Gersten, K. *Boundary-layer theory*. (Springer, 2016).

40 Narasimha, R., Narayan, K. Y. & Parthasarathy, S. Parametric analysis of turbulent wall jets in still air. *The Aeronautical Journal* **77**, 355-359 (1973).
41 Wygnanski, I., Katz, Y. & Horev, E. On the applicability of various scaling laws to the turbulent wall jet. *J Fluid Mech* **234**, 669-690 (1992).
42 Morkovin, M. V. Effects of compressibility on turbulent flows. *Mécanique de la Turbulence* **367**, 380 (1962).
43 Ahlman, D., Velter, G., Brethouwer, G. & Johansson, A. V. Direct numerical simulation of nonisothermal turbulent wall jets. *Physics of fluids* **21**, 035101 (2009).
44 Huang, P., Coleman, G. & Bradshaw, P. Compressible turbulent channel flows: DNS results and modelling. *J Fluid Mech* **305**, 185-218 (1995).
45 Driest, E. V. Turbulent boundary layer in compressible fluids. *Journal of the Aeronautical Sciences* **18**, 145-160 (1951).
46 Shukla, A. K. & Dewan, A. Flow and thermal characteristics of jet impingement on a flat plate for small nozzle to plate spacing using LES. *International Journal of Thermal Sciences* **145**, 106005 (2019).
47 Leonard, B. P. A stable and accurate convective modelling procedure based on quadratic upstream interpolation. *Computer methods in applied mechanics and engineering* **19**, 59-98 (1979).
48 Jaramillo, J., Trias, F., Gorobets, A., Pérez-Segarra, C. & Oliva, A. DNS and RANS modelling of a turbulent plane impinging jet. *International Journal of Heat and Mass Transfer* **55**, 789-801 (2012).
49 Alvi, F., Ladd, J. & Bower, W. Experimental and computational investigation of supersonic impinging jets. *American Institute of Aeronautics and Astronautics. AIAA Journal* **40**, 599-609, doi:10.2514/2.1709 (2002).
50 Menter, F. in *23rd fluid dynamics, plasmadynamics, and lasers conference.* 2906.
51 Shukla, A. K. & Dewan, A. Flow and thermal characteristics of jet impingement: comprehensive review. *Int. J. Heat Technol* **35**, 153-166 (2017).
52 Keedy, R., Dengler, E., Ariessohn, P., Novosselov, I. & Aliseda, A. Removal rates of explosive particles from a surface by impingement of a gas jet. *Aerosol Science and Technology* **46**, 148-155 (2012).
53 Kottapalli, K. *Aerodynamic Removal and Characterization of Particulate Trace Residues on Model Surfaces*, University of Washington Libraries, (2017).
54 Beltaos, S. Oblique impingement of plane turbulent jets. *Journal of the Hydraulics Division* **102**, 1177-1192 (1976).
55 Naqavi, I. Z., Tyacke, J. C. & Tucker, P. G. Direct numerical simulation of a wall jet: flow physics. *J Fluid Mech* **852**, 507-542 (2018).
56 Barenblatt, G., Chorin, A. & Prostokishin, V. The turbulent wall jet: A triple-layered structure and incomplete similarity. *Proceedings of the National Academy of Sciences* **102**, 8850-8853 (2005).
57 Banyassady, R. & Piomelli, U. Turbulent plane wall jets over smooth and rough surfaces. *Journal of Turbulence* **15**, 186-207 (2014).
58 Eriksson, J., Karlsson, R. & Persson, J. An experimental study of a two-dimensional plane turbulent wall jet. *Exp Fluids* **25**, 50-60 (1998).
59 Tang, Z., Rostamy, N., Bergstrom, D., Bugg, J. & Sumner, D. Incomplete similarity of a plane turbulent wall jet on smooth and transitionally rough surfaces. *Journal of Turbulence* **16**, 1076-1090 (2015).
60 Bradshaw, B. & Gee, M. Turbulent wall jets with and without an external stream. (Aeronautics Research Council, Report and Memoranda
No. 3252, 1960).
61 Fillingham, P., Zhan, X., Kottapalli, K. & Novosselov, I. V. Vol. 128 89-98 (Journal of Aerosol Science, 2019).
62 Novosselov, I. V., Ariessohn, P. C., Dengler, E. D. & Hickner, M. Particle interrogation devices and methods. USA patent 8307723 (2012).
63 Novosselov, I. V., Ariessohn, P. C., Dengler, E. D. & Hickner, M. Particle interrogation devices and methods. USA patent 8561486 (2013).
64 Novosselov, I. Pulsed jet sampling of particles and vapors from substrates. US patent 10274404 (2019).
65 Gorny, R. L. *et al*. Fungal Fragments as Indoor Air Biocontaminants. *Applied and Environmental Microbiology* **68**, 3522 (2002).
66 Hodgson, M. Field studies on the sick building syndrome. *Annals of the New York Academy of Sciences* **641**, 21-36 (1992).
67 Heim, L.-O., Blum, J., Preuss, M. & Butt, H.-J. Adhesion and Friction Forces between Spherical Micrometer- Sized Particles. *Phys. Rev. Lett.* **83**, 3328-3331, doi:10.1103/PhysRevLett.83.3328 (1999).
68 Lam, K. K. & Newton, J. M. Investigation of applied compression on the adhesion of powders to a substrate surface. *Powder Technology* **65**, 167-175, doi:10.1016/0032-5910(91)80179-M (1991).
69 Podczeck, F. & Newton, J. M. Development of an ultracentrifuge technique to determine the adhesion and friction properties between particles and surfaces. *Journal of Pharmaceutical Sciences* **84**, 1067-1071, doi:10.1002/jps.2600840907 (1995).
70 Salazar-Banda, G. R., Felicetti, M. A., Gonçalves, J. A. S., Coury, J. R. & Aguiar, M. L. Determination of the adhesion force between particles and a flat surface, using the centrifuge technique. *Powder Technology* **173**, 107-117, doi:10.1016/j.powtec.2006.12.011 (2007).
71 Krupp, H. Particle adhesion theory and experiment. *Advances in Colloid and Interface Science* **1**, 111-239, doi:10.1016/0001-8686(67)80004-6 (1967).
72 Mizes, H., Ott, M., Eklund, E. & Hays, D. Small particle adhesion: measurement and control. *Colloids and Surfaces A: Physicochemical and Engineering Aspects* **165**, 11-23, doi:10.1016/S0927-7757(99)00442-2 (2000).
73 Larsen, R. The Adhesion and Removal of Particles Attached to Air Filter Surfaces. *American Industrial Hygiene Association Journal* **19**, 265-270, doi:10.1080/00028895809343591 (1958).
74 Kordecki, M. C. & Orr, C. Adhesion of Solid Particles to Solid Surfaces. *Archives of Environmental Health: An International Journal* **1**, 1-9, doi:10.1080/00039896.1960.10662660 (1960).
75 Deryagin, B. & Zimon, A. Adhesion of particles of a powder to plane surfaces. *Kolloidnyi Zhurnal* **23**, 544-& (1961).
76 Zimon, A. D. *Adhesion of dust and powder*. (Springer Science & Business Media, 2012).
77 Visser, J. Measurement of the force of adhesion between submicron carbon- black particles and a cellulose film in aqueous solution. *Journal of Colloid And Interface Science* **34**, 26-31, doi:10.1016/0021-9797(70)90254-7 (1970).
78 Visser, J. The adhesion of colloidal polystyrene particles to cellophane as a function of pH and ionic strength. *Journal of Colloid And Interface Science* **55**, 664-677, doi:10.1016/0021-9797(76)90077-1 (1976).
79 Lucassen, J. & Van Den Tempel, M. Dynamic measurements of dilational properties of a liquid interface. *Chemical Engineering Science* **27**, 1283-1291, doi:10.1016/0009-2509(72)80104-0 (1972).

80 Hubbe, M. A. Theory of detachment of colloidal particles from flat surfaces exposed to flow. *Colloids and Surfaces* **12**, 151-178, doi:10.1016/0166-6622(84)80096-7 (1984).
81 Sharma, M. M., Chamoun, H., Sarma, D. S. H. S. R. & Schechter, R. S. Factors controlling the hydrodynamic detachment of particles from surfaces. *Journal of Colloid And Interface Science* **149**, 121-134, doi:10.1016/0021-9797(92)90398-6 (1992).
82 Waals, J. D. v. d. *Over de continuiteit van den gas- en vloeistoftoestand*. (Leyden, 1873).
83 Hamaker, H. C. The London— van der Waals attraction between spherical particles. *Physica* **4**, 1058-1072, doi:10.1016/S0031-8914(37)80203-7 (1937).
84 Derjaguin, B. V., Abrikosova, I. I. & Lifshitz, E. M. Direct measurement of molecular attraction between solids separated by a narrow gap. *Quarterly Reviews, Chemical Society* **10**, 295-329, doi:10.1039/QR9561000295 (1956).
85 Derjaguin, B. V., Muller, V. M. & Toporov, Y. P. Effect of contact deformations on the adhesion of particles. *Journal of Colloid And Interface Science* **53**, 314-326, doi:10.1016/0021-9797(75)90018-1 (1975).
86 Hertz, H. R. Über die Berührung fester elastischer Körper und über die Härte. (2006).
87 Johnson, K. L., Kendall, K. & Roberts, A. D. Surface Energy and the Contact of Elastic Solids. *Proceedings of the Royal Society of London. Series A, Mathematical and Physical Sciences (1934-1990)* **324**, 301-313, doi:10.1098/rspa.1971.0141 (1971).
88 Tabor, D. Surface forces and surface interactions. *Journal of Colloid And Interface Science* **58**, 2-13, doi:10.1016/0021-9797(77)90366-6 (1977).
89 Maugis, D. & Pollock, H. M. Surface forces, deformation and adherence at metal microcontacts. *Acta Metallurgica* **32**, 1323-1334, doi:10.1016/0001-6160(84)90078-6 (1984).
90 Saffman, P. G. The lift on a small sphere in a slow shear flow. *Journal of Fluid Mechanics* **22**, 385-400, doi:10.1017/S0022112065000824 (1965).
91 O'Neill, M. E. A sphere in contact with a plane wall in a slow linear shear flow. *Chemical Engineering Science* **23**, 1293-1298, doi:10.1016/0009-2509(68)89039-6 (1968).
92 Mollinger, A. M. & Nieuwstadt, F. T. M. Measurement of the lift force on a particle fixed to the wall in the viscous sublayer of a fully developed turbulent boundary layer. *J. Fluid. Mech.* **316**, 285-306, doi:10.1017/S0022112096000547 (1996).
93 Wang, H.-C. Effects of Inceptive Motion on Particle Detachment from Surfaces. *Aerosol Science and Technology* **13**, 386-393, doi:10.1080/02786829008959453 (1990).
94 Ziskind, G., Fichman, M. & Gutfinger, C. Adhesion moment model for estimating particle detachment from a surface. *Journal of Aerosol Science* **28**, 623-634, doi:10.1016/S0021-8502(96)00460-0 (1997).
95 Dominik, C. & Tielens, A. G. G. M. Resistance to rolling in the adhesive contact of two elastic spheres. *Philosophical Magazine A* **72**, 783-803, doi:10.1080/01418619508243800 (1995).
96 Tsai, C.-J., Pui, D. Y. H. & Liu, B. Y. H. Particle detachment from disk surfaces of computer disk drives. *Journal of Aerosol Science* **22**, 737-746, doi:10.1016/0021-8502(91)90066-Q (1991).
97 Soltani, M. & Ahmadi, G. Particle Detachment from Rough Surfaces in Turbulent Flows. *The Journal of Adhesion* **51**, 105-123, doi:10.1080/00218469508009992 (1995).
98 Bardina, J. E. (eds P. G. Huang, Thomas J. Coakley, & Center Ames Research) (Moffett Field, Calif. : National Aeronautics and Space Administration, Ames Research Center ; Springfield, Va. : National Technical Information Service, distributor, Moffett Field, Calif. : [Springfield, Va.], 1997).
99 Menter, F. R. (Sponsoring Organization: NASA Ames Research Center, 1993).
100 Zeng, L., Najjar, F., Balachandar, S. & Fischer, P. Forces on a finite-sized particle located close to a wall in a linear shear flow. *Physics of fluids* **21**, 033302 (2009).
101 Esayanur, M. S., Yeruva, S. B., Rabinovich, Y. I. & Moudgil, B. M. Interaction force measurements using atomic force microscopy for characterization and control of adhesion, dispersion and lubrication in particulate systems. *Journal of Adhesion Science and Technology* **19**, 611-626, doi:10.1163/1568561054890516 (2005).
102 Biggs, S., Cain, R. G., Dagastine, R. R. & Page, N. W. Direct measurements of the adhesion between a glass particle and a glass surface in a humid atmosphere. *Journal of Adhesion Science and Technology* **16**, 869-885, doi:10.1163/156856102760136445 (2002).
103 Maugis, D. Subcritical crack growth, surface energy, fracture toughness, stick-slip and embrittlement. *Journal of materials science* **20**, 3041-3073, doi:10.1007/BF00545170
info:doi/10.1007/BF00545170 (1985).
104 Derjaguin, B. Untersuchungen über die Reibung und Adhäsion, IV. *Kolloid-Zeitschrift* **69**, 155-164, doi:10.1007/BF01433225 (1934).
105 Masuda, H., Gotoh, K., Fukada, H. & Banba, Y. The removal of particles from flat surfaces using a high- speed air jet. *Advanced Powder Technology* **5**, 205-217, doi:10.1016/S0921-8831(08)60615-9 (1994).
106 Otani, Y., Emi, H., Morizane, T. & Mori, J. Removal of fine particles from wafer surface by pulse air jets. *Kagaku Kogaku Ronbunshu* **19**, 114-119, doi:10.1252/kakoronbunshu.19.114 (1993).
107 Otani, Y., Namiki, N. & Emi, H. Removal of Fine Particles from Smooth Flat Surfaces by Consecutive Pulse Air Jets. *Aerosol Science and Technology* **23**, 665-673, doi:10.1080/02786829508965346 (1995).
108 Ziskind, G., Yarin, L. P., Peles, S. & Gutfinger, C. Experimental Investigation of Particle Removal from Surfaces by Pulsed Air Jets. *Aerosol Science and Technology* **36**, 652-659, doi:10.1080/02786820252883883 (2002).
109 Smedley, G. T., Phares, D. J. & Flagan, R. C. Entrainment of fine particles from surfaces by impinging shock waves. *Experiments in Fluids* **26**, 116-125, doi:10.1007/s003480050270 (1999).
110 Gotoh, K., Takebe, S., Masuda, H. & Banba, Y. The Effect of Humidity on the Removal of Fine Particles on a Solid Surface using High-speed Air Jet. *KONA Powder and Particle Journal* **13**, 191-203, doi:10.14356/kona.1995024 (1995).
111 Henry, C. & Minier, J.-P. Progress in particle resuspension from rough surfaces by turbulent flows. *Progress in Energy and Combustion Science* **45**, 1-53, doi:10.1016/j.pecs.2014.06.001 (2014).
112 Lee, H. & Balachandar, S. Critical shear stress for incipient motion of a particle on a rough bed. *Journal of Geophysical Research: Earth Surface* **117** (2012).
113 Yahiaoui, S. & Feuillebois, F. Lift on a sphere moving near a wall in a parabolic flow. *Journal of fluid mechanics* **662**, 447-474 (2010).
114 Kottapalli, K. & Novosselov, I. V. Experimental study of aerodynamic resuspension of RDX residue. *Aerosol Science and Technology* **53**, 549-561 (2019).
115 Militzer, J., Kan, J., Hamdullahpur, F., Amyotte, P. & Al Taweel, A. Drag coefficient for axisymmetric flow around individual spheroidal particles. *Powder technology* **57**, 193-195 (1989).

116 Hölzer, A. & Sommerfeld, M. New simple correlation formula for the drag coefficient of non-spherical particles. *Powder Technology* **184**, 361-365 (2008).
117 Ouchene, R., Khalij, M., Tanière, A. & Arcen, B. Drag, lift and torque coefficients for ellipsoidal particles: From low to moderate particle Reynolds numbers. *Computers & Fluids* **113**, 53-64 (2015).
118 Ouchene, R., Khalij, M., Arcen, B. & Tanière, A. A new set of correlations of drag, lift and torque coefficients for non-spherical particles and large Reynolds numbers. *Powder Technology* **303**, 33-43 (2016).
119 Zastawny, M., Mallouppas, G., Zhao, F. & Van Wachem, B. Derivation of drag and lift force and torque coefficients for non-spherical particles in flows. *International Journal of Multiphase Flow* **39**, 227-239 (2012).
120 Harper, E. & Chang, I.-D. Maximum dissipation resulting from lift in a slow viscous shear flow. *Journal of Fluid Mechanics* **33**, 209-225 (1968).
121 Gavze, E. & Shapiro, M. Particles in a shear flow near a solid wall: effect of nonsphericity on forces and velocities. *International Journal of Multiphase Flow* **23**, 155-182 (1997).
122 Cui, Y., Ravnik, J., Hriberšek, M. & Steinmann, P. A novel model for the lift force acting on a prolate spheroidal particle in an arbitrary non-uniform flow. Part I. Lift force due to the streamwise flow shear. *International Journal of Multiphase Flow* **104**, 103-112 (2018).
123 Happel, J. & Brenner, H. *Low Reynolds number hydrodynamics: with special applications to particulate media*. Vol. 1 (Springer Science & Business Media, 2012).
124 Coelho, P. J. Numerical simulation of radiative heat transfer from non-gray gases in three-dimensional enclosures. *Journal of Quantitative Spectroscopy and Radiative Transfer* **74**, 307-328, doi:10.1016/S0022-4073(01)00249-7 (2002).
125 Hwang, J. C., Tsou, F. K. & Cho, W. C. K-EPSILON computations of flow and heat transfer in plane oblique impinging jets. <xocs:firstpage xmlns:xocs=""/> (1982).
126 Schauer, J. (ProQuest Dissertations Publishing, 1964).
127 Mercier-Bonin, M., Dehouche, A., Morchain, J. & Schmitz, P. Orientation and detachment dynamics of Bacillus spores from stainless steel under controlled shear flow: modelling of the adhesion force. *International journal of food microbiology* **146**, 182-191 (2011).
128 Kesavan, J. S. *et al.* Deposition method, relative humidity, and surface property effects of bacterial spore reaerosolization via pulsed air jet. *Aerosol Science and Technology* **51**, 1027-1034 (2017).
129 Fillingham, P. & Novosselov, I. Similarity of the Wall Jet Resulting from Planar Underexpanded Impinging Jets. (2018).
130 Crafton, J., Carter, C., Elliott, G. & Sullivan, J. The impingement of sonic and sub-sonic jets onto a flat plate at inclined angles. *Experimental Methods and their Applications to Fluid Flow* **41**, 699-710, doi:10.1007/s00348-006-0192-z (2006).
131 Nguyen, T. & Blake, M. Flowfield Characteristics of a Supersonic Jet Impinging on an Inclined Surface. *American Institute of Aeronautics and Astronautics. AIAA Journal* **58**, 1240-1254, doi:10.2514/1.J058897 (2020).
132 Dorrepaal, J. M. An exact solution of the Navier-Stokes equation which describes non-orthogonal stagnation-point flow in two dimensions. *J. Fluid. Mech.* **163**, 141-147, doi:10.1017/S0022112086002240 (1986).
133 Chin, D. & Agarwal, M. MASS-TRANSFER FROM AN OBLIQUE IMPINGING SLOT JET. *Journal Of The Electrochemical Society* **138**, 2643-2650, doi:10.1149/1.2086031 (1991).
134 Mazurek, K. A. & Rajaratnam, N. Erosion of sand beds by obliquely impinging plane turbulent air jets. *Journal of Hydraulic Research* **43**, 567-573, doi:10.1080/00221680509500155 (2005).
135 ANSYS FLUENT 12.0 Theory Guide - 18. Solver Theory. (2017). <http://www.afs.enea.it/project/neptunius/docs/fluent/html/th/node359.htm>.

APPENDIX A. OBLIQUELY IMPINGING UNDEREXPANDED PLANAR JETS

The wall shear stress associated with underexpanded planar jets impinging onto an inclined incidence has not been adequately investigated despite its wide practical applications. In this work, computational fluid dynamics is used to parametrically investigate the flow field of under expanded rectangular jets impinging onto a flat inclined surface. Pressure-sensitive paint is used to visualize the static pressure on the flat plate upon jet impingement and validate the results obtained from numerical simulations. The results are used to formulate an equation for predicting maximum wall shear stress on the impingement surface within a mean deviation from CFD of 3%.

I. INTRODUCTION

Impinging jets have a wide range of scientific and engineering applications and have been studied extensively. While most of these studies focus on heat and mass transfer [28,30,124-126], the focus of this work is to analyze the wall shear stress developed by the oblique impingement of underexpanded planar jets. The main applications are related to aerodynamic particle removal from the surfaces, such as in surface cleaning and non-contact surface sampling. Microparticle resuspension has been shown to have an excellent correlation to wall shear stress [6, 7]. Phares et al. [20] have suggested that resuspension of controlled particles could be used to estimate the wall shear stress developed by impinging jets. Small, deforming, or irregular shape microparticles, e.g., residues of energetic materials [52,114], microorganisms [127,128], and nanoparticles, require exposure to high velocities at the surface [111], which implies high wall shear stress. These levels shear stresses are not typical weather-induced conditions, but that can be generated by the impingement of

supersonic or high-pressure underexpanded jets. Studies of underexpanded jets have typically been confined to normally impinging axisymmetric jets as they have implications for vertical take-off and landing aircraft [9,10,32]. Recently, we have parameterized the wall flow behavior from impingiung jet designed the studies of particle resuspension using a laboratory test setup [7,27].

Obliquely impinging planar jets have advantages over normally impinging jets. They can produce larger and more uniform regions of high shear stress than round or other low aspect ratio nozzles, which is desirable for particle resuspension studies, cleaning, and heat transfer applications. Additionally, in non-contact surface sampling, the wall jet flow entrains and directs the resuspended particles for their subsequent collection and analysis in contrast to scattering the sample as with axisymmetric jets [114]. Fillingham et al. [129] presented parameterization of the normal impingement of planar underexpanded jet, but the correlations developed in that work do not expand to oblique impingement. In Crafton et al. [130] and Ngyuen et al. [131], the flowfield of axisymmetric underexpanded jets impinging on an inclined surface is studied experimentally. However, the authors did not consider planar jets and or wall shear stress correlations.

The flow field of subsonic planar jets impinging normally and obliquely has been studied previously. Dorrepaal [132] found a similarity solution which described the impingement of 2-D incompressible non-orthogonal stagnation point flows. Beltaos [54] examined the flow field extensively. They used Preston tube measurements to calculate the wall shear stress developed from the incompressible oblique impingement of planar jets. The behavior of compressible jets and characterization of wall shear stress was not considered. Chin et al. [133] studied the mass transfer of obliquely impinging planar jets but did not examine wall shear stress. Hwang et al. [125] conducted a computational study of obliquely impinging slot jets, but the turbulence model used is unreliable for wall shear stress measurement. Rajaratnam et al. [134] studied erosion, which was closely tied to

wall shear stress from obliquely planar jets. Still, their results do not directly apply to particle resuspension from a rigid surface. The lack of experimental and computational data for obliquely impinging planar jets in the compressible region suggests the need for a parametric computational study of said jets.

In this work, we present a parametric study of obliquely impinging, underexpanded planar jets. Impingement angles from 30° to 90° are examined at jet standoff height to width ratios from 15-30 and nozzle pressure ratios from 1.0-3.4. This computational matrix allows for the formulation of a correlation for the maximum wall shear stress as a function of the jet parameters.

II. PROBLEM DESCRIPTION

One can fully characterize an obliquely impinging underexpanded jet by four parameters: the standoff height, H, the jet width, W, the jet nozzle pressure ratio, NPR, and the jet impingement angle, θ. Thus, in this work, we used these variables to parameterize the wall shear stress. We also define the uphill and downhill directions, as demonstrated in Figure 1. Table 1 Summarizes the range of values for each parameter used in the computational study.

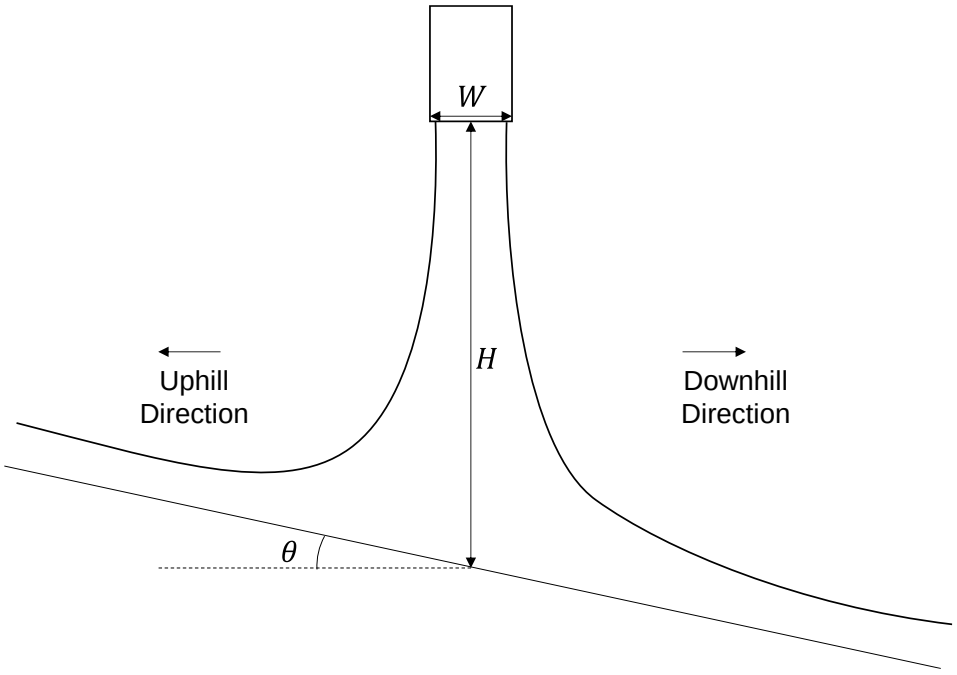

Fig. 1 Schematic of oblique jet impingement on a flat plate.

Table 1: Range of geometric conditions used for CFD to predict the shift in stagnation point.

Standoff distance, H (mm)	15.0, 17.5, 30.0, 35.0, 60.0, 100.0
Width of the nozzle, W (mm)	0.5, 1.0, 2.0
Jet Angle, θ (°)	0, 15, 20, 30, 45, 60
Nozzle exit pressure ratio, NPR	1.0, 1.2, 1.4, 1.6, 1.8, 2.0, 2.2, 2.4, 2.6, 2.8, 3.0, .3.2, 3.4

The analysis is performed using non-dimensional parameters, such as the normalized maximum wall shear stress is defined as:

$$\tau^*_{max} = \frac{\tau_{max}}{\frac{1}{2}\rho_o U_o^2},$$

where $\rho_o$and U_o are the density and velocity at the nozzle exit, respectively. The objective of this work is to develop a set of equations for the prediction of the maximum normalized wall shear stress as a function of the following non-dimensional parameters: jet height to width ration, $\frac{H}{W}$, the

nozzle pressure ratio, NPR, the jet Reynolds number, $Re = \frac{U_o W}{\nu_o}$, and the jet impingement angle θ. A naught subscript describes the properties at the nozzle exit.

III. COMPUTATIONAL METHOD

The computational analysis was performed using the commercial software code ANSYS FLUENT 17.2 and a cell-centered finite volume approach. The steady-state Reynolds and Favre averaged Navier–Stokes equations are solved to obtain the flow field. The solver uses a pressure-based scheme with pressure-velocity coupling [135]. A second-order scheme was used for the pressure. A third-order monotonic upstream-centered scheme for conservation laws was used for density, momentum, and turbulence, which was necessary to avoid the effects of numerical viscosity (associated with the low-order schemes) on the jet dissipation, as well as pressure–strain relationship. Since the flow contains not-negligible changes in temperature, the Sutherland model, which is based on the kinetic theory of ideal gases and an idealized intermolecular-force potential, is used for viscosity calculation.

The computational grids contain ~500,000 quadrilateral elements. The grid is constructed so that, along the impingement surface, the first node in the wall-normal direction is at a constant distance from the wall and is located within a y^+=1 at the maximum shear stress location for every considered case. This grid resolution ensures that the viscous sublayer is resolved for the entire domain. The maximum x-direction spacing gives an element aspect ratio no greater than 50:1. Mesh independence was confirmed by doubling the number of elements; this further mesh refinement did not affect the results.

The computational method for this work is identical to that of Fillingham et al. [27] and has been validated extensively against both direct numerical simulation (DNS) [48,55] and the experiments [33] The oblique impingement of underexpanded jets was studied experimentally using pressure-

sensitive paint. Pressure sensitive paint uses oxygen doping of luminophores that emit light at an intensity inversely proportional to the partial pressure of oxygen, allowing for the mapping of normal pressure along a surface. Figure 2 shows the normal pressure profiles from the pressure-sensitive paint experiment plotted against those from the CFD.

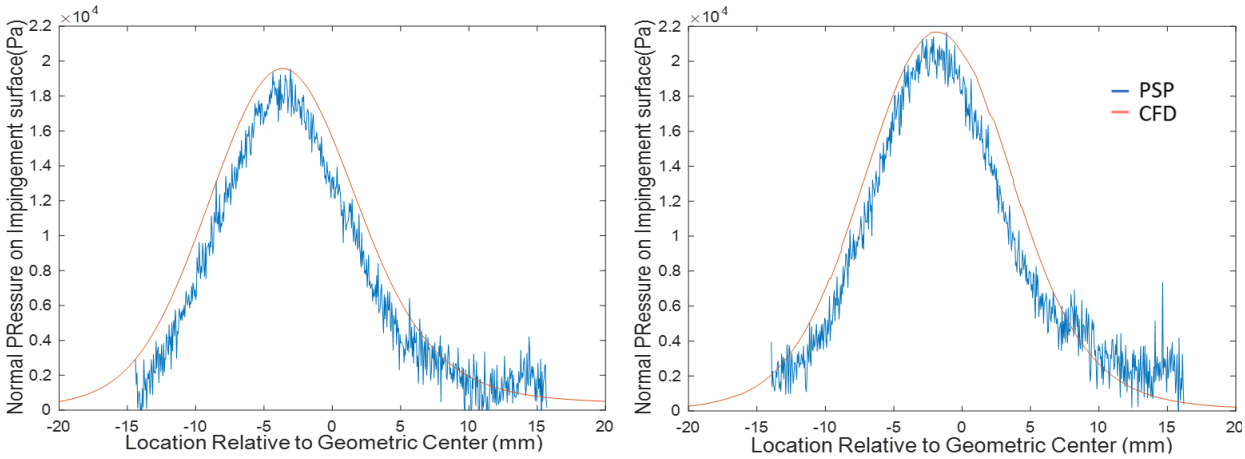

Fig. 2 Normal pressure profiles from CFD (red) and pressure sensitive paint (blue) experiments. H = 30 mm, W = 0.5 mm, NPR = 1.0 with the impingement angle of 30 degrees (left) and 15 degrees (right).

IV. RESULTS & DISCUSSION

After completing the computational study, the maximum wall shear stress was tabulated for each case and examined as a function of each jet parameter. Figure 3 plots the normalized maximum wall shear stress against the nozzle pressure ratio. When examining the dependence of maximum wall shear stress on nozzle pressure ratio alone, we found that when all other parameters are fixed, the maximum wall shear stress increases with approximately the square root of Nozzle Pressure Ratio for all cases.

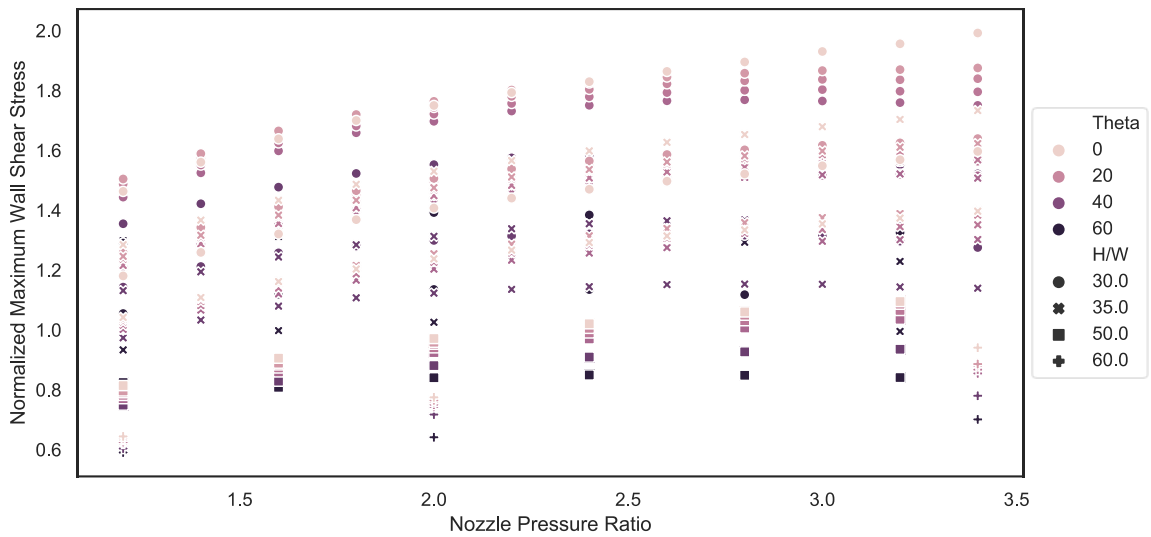

Fig. 3 Normalized maximum wall shear stress plotted against nozzle pressure ratio with impingement angle represented by shade and height to width ratio designated by the symbol.

Figure 4 plots the normalized maximum wall shear stress against the height to width ratio. As would be expected the maximum wall shear stress decreases with increasing height to width ratio. The maximum wall shear stress is proportional to the inverse of the height to width ratio when all other parameters are fixed.

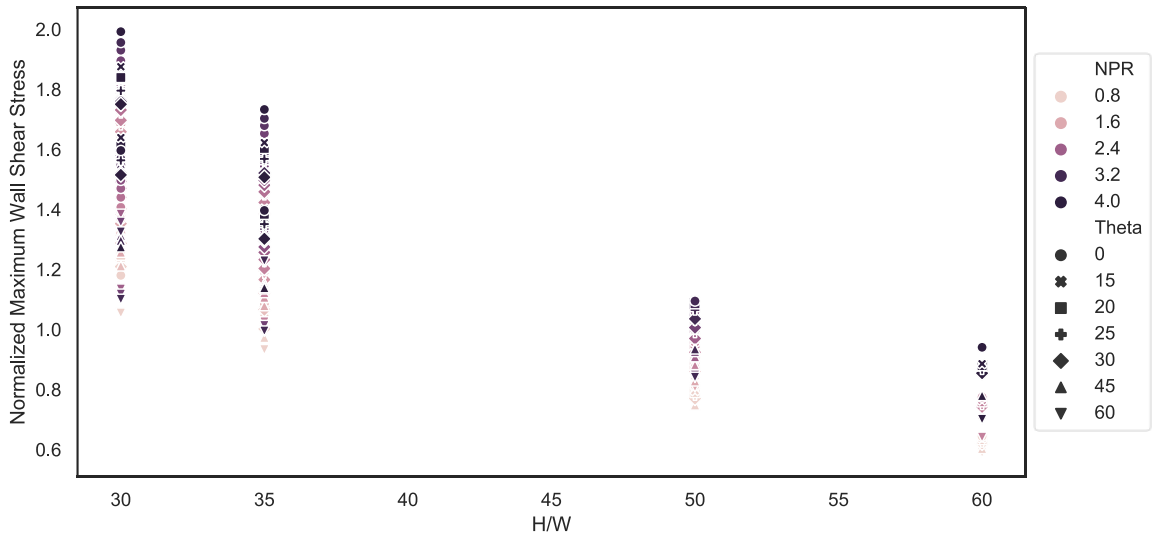

Fig. 4 Normalized maximum wall shear stress plotted against height to width ratio with nozzle pressure ratio represented by shade and impingement angle represented by the symbol.

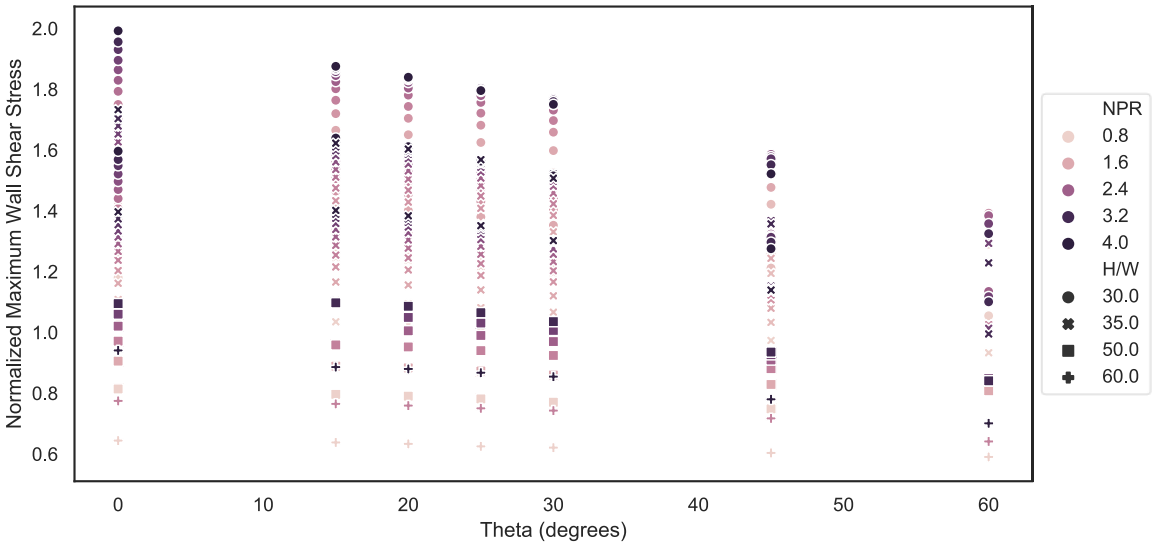

Fig. 5 Normalized maximum wall shear stress plotted impingement angle with nozzle pressure ratio represented by shade and height to width ratio represented by the symbol.

Figure 5. illustrates that maximum wall shear stress decreases with impingement angle. This relationship was found to resemble a function of the form: $1 - \sin\theta$. After analyzing the maximum wall shear stress as a function of jet parameters, we propose an equation for normalized maximum wall shear stress of the form:

$$\tau^*_{max} = \tau^*_{max,\theta=0}\left(1 - a\left(\frac{\mathrm{H}}{\mathrm{W}}\right)^{\mathrm{b}} \mathrm{NPR}^{\mathrm{c}}\sin^{d}\theta\right). \quad (1)$$

To use this equation, we must first determine the normalized maximum wall shear stress at an impingement angle of 0° as a function of height to width ratio, nozzle pressure ratio, and Reynolds number. We expect a Reynolds number term to be relevant, as the normalized maximum wall shear stress will not be Reynolds number asymptotic, as found by Fillingham et al.[7]. The size adjustment is necessary as the effective turbulent viscosity increases with Reynolds

number and thus decreases the expected maximum wall shear stress. Therefore, for the normalized maximum wall shear stress at normal impingement, we propose the following equation:

$$\tau^*_{max,\theta=0} = \alpha \left(\frac{H}{W}\right)^{\beta} NPR^{\gamma} Re^{\lambda} \tag{2}$$

Least-squares fitting gives the following values for the coefficient and exponents:

$$\alpha = 9338.08$$

$$\beta = -1.146$$

$$\gamma = 0.589$$

$$\lambda = -0.301$$

The resulting Equation 2 allows for the prediction of the maximum wall shear stress from the normal impingement of underexpanded planar jets. The equation calculates the maximum shear stress with a maximum deviation from CFD of 5.7% and a mean deviation of 2.1%. Figure 6 plots the predicted maximum wall shear stress against the calculated value from CFD.

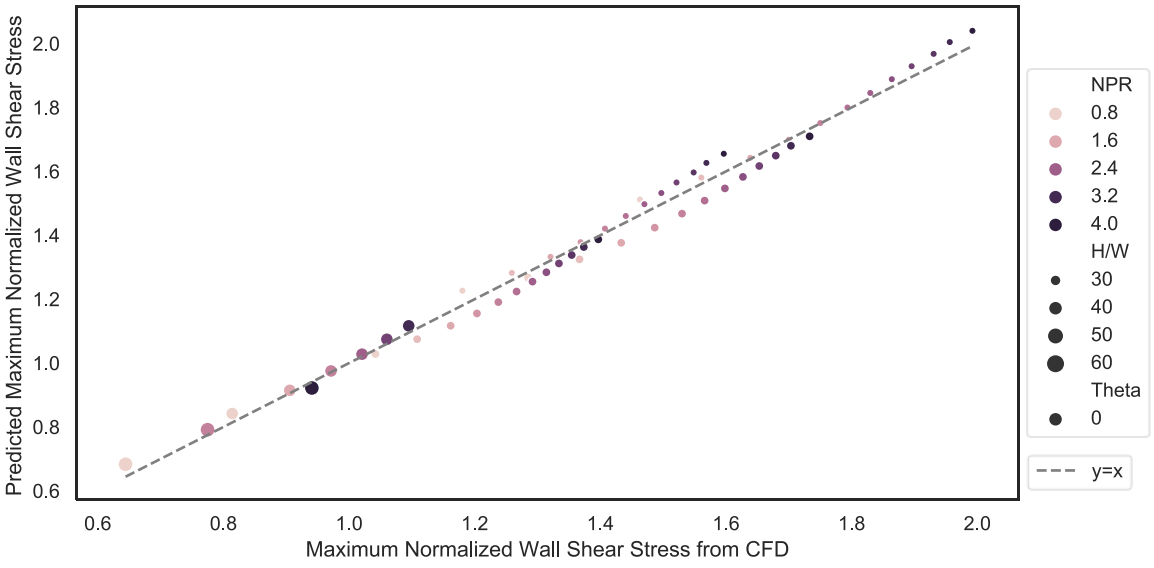

Fig. 6 Predicted maximum normalized wall shear stress plotted against maximum normalized wall shear stress from CFD for normal impingement. Shade represents the nozzle pressure ratio, while the symbol represents the height to width ratio.

After finding the normal impingement correlations, we calculated the coefficient and exponents for equation 1. Least-squares fitting yields the following coefficients:

$$a = 0.208$$

$$b = -0.276$$

$$c = 1.213$$

$$d = 1.512$$

Using equation 1, we can predict the maximum wall shear stress with a maximum deviation from CFD of 10.3% and an average deviation of 3.3%. Figure 7 plots the predicted normalized maximum wall shear stress values against the values calculated via CFD.

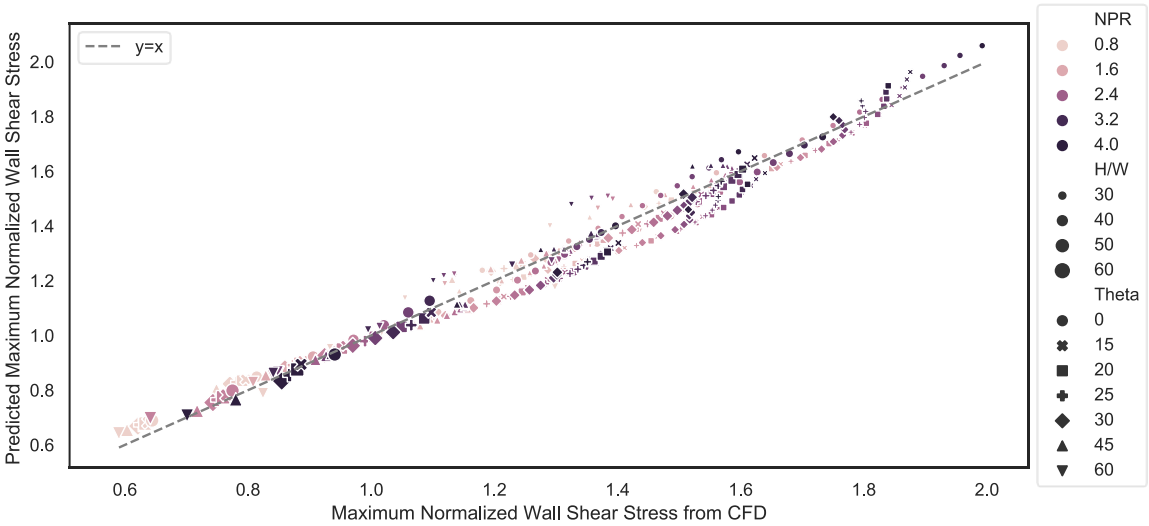

Fig. 7 Predicted maximum normalized wall shear stress plotted against maximum normalized wall shear stress from CFD for all impingement angles. Shade represents nozzle pressure ratio, while symbol represents impingement angle, and marker size represents height to width ratio.

V. Conclusions

This paper investigates the impingement of under expanded oblique flat jets to find the maximum wall shear stress associated with the wall-bounded flow. Obliquely impinging jets find application in many fields, this study focuses on their use in studies of aerodynamic particle resuspension where the knowledge of shear stress is important, as particle resuspension thresholds and removal rates can be directly correlated with wall shear stresses [61]. When addressing removal "sticky" particles such as residues of energetic material or biological particles, high wall shear stresses are required [6]. Obliquely impinging jets provide a larger area of high wall shear stress as well as a mechanism for transporting the resuspended particles. This work provides a set of equations for the prediction of the maximum wall shear stress resulting from obliquely impinging underexpanded planar jets as a function of jet parameters. The maximum wall shear stress can be predicted within a mean error of 3.3%.